2016

Interactions Between Local Magnetic Moments and Itinerant Charge Carriers in Fe-based systems

Yan Wu
Louisiana State University and Agricultural and Mechanical College

INTERACTIONS BETWEEN LOCAL MAGNETIC MOMENTS AND ITINERANT CHARGE CARRIERS IN FE-BASED SYSTEMS

A Dissertation

Submitted to the Graduate Faculty of the
Louisiana State University and
Agricultural and Mechanical College
in partial fulfillment of the
requirements for the degree of
Doctor of Philosophy

in

The Department of Physics and Astronomy

by
Yan Wu
B.S., Northwest University, 2006
M.S., Graduate School of Chinese Academy of Science, 2010
May 2016

Acknowledgments

I would like to express my sincere gratitude to my supervisor, Dr. John DiTusa. His expertise, motivation and patience had been essential in leading my entire Ph. D. study and research. His enthusiasm for research has always encouraged me. This work would not be possible without his continuous support in funding and his guidance with vast knowledge and skills. I also would like to thank other members of my committee, Dr. David Young, Dr. Rongying Jin, Dr. Ilya Vekhter, Dr. A. Ravi P. Rau and Dr. Louay Mohammad for the all the useful suggestions and assistance they provided at all levels of the research project.

My sincere thanks also goes to Dr. David Young, Dr. Rongying Jin, Dr. Philip Adams from LSU and Dr. Julia Chan from UT-Dallas, for providing the instruments and guidances in material synthesis, characteristics and measurements.

I would also like to thank instrument scientists at the Oak Ridge national Lab, particularly Huibo Cao, for the assistance in neutron scattering experiments and analysis process, which has contributed to a important part of my Ph. D research.

I want to express my gratitude to Dr. W. Adam Phelan who had spared time to help me as proofreader of this work. I would also like to thank all friends from our group and other groups at LSU for the stimulating discussions we had in meetings and in labs, for the busy days of crystals growth, for all the help at work and off work, and for all the fun we had together that enlightened my life at LSU.

This dissertation is dedicated to my family: my parents who gave my life and always support me whenever I need them and my brother and sisters who shared lots of happy or sorrow moments of my life.

Table of Contents

List of Tables

List of Figures

Abstract

The interactions between magnetic moments and electrons are essential in creating many of the unique properties of magnetic systems. In this thesis, I focused on two Fe-based systems employing multiple experimental techniques to investigate the coupling between localized magnetic moments and conducting charge carriers in two systems with tendencies to order into itinerant magnetic phases.

With systematic investigations of $Fe_{1-y}Co_ySi$, we discovered a field depended non-Fermi-Liquid (non-FL) behavior near its insulator-metal-transition (IMT) that appears to share the same mechanism as previously discovered in Mn doped FeSi - the underscreened Kondo effect.

A similar interaction of the charge carrier moments screening $S = 1$ impurity moments are found in the $y \approx 0.01$ range of Co doped FeSi as in $Fe_{1-x}Mn_xSi$. The conductivity results indicate a field dependent non-FL behavior at IMT of $Fe_{1-y}Co_ySi$ that transitions to a disordered FL dependence with the application of magnetic field or by increasing the density of Co substitutions. However, Co-substitution between $0.01 < x \leq 0.03$ displays unique behavior which is enhanced by the application of magnetic field. We are presently exploring the consequences of this discovery. A relatively large density of unscreened magnetic moments at low temperature was confirmed through specific heat measurements at several magnetic fields over a wide range of temperatures. These findings indicate that the non-FL of Mn and Co doped FeSi is related to the underscreened Kondo mechanism and depends only on the local interaction rather than the charge carrier type.

A second Fe-based magnetic system Fe_3Ga_4 was investigated via neutron scattering technique. In the neutron scattering investigations of on the Fe_3Ga_4 system, ferromagnetic (FM) ordered states are confirmed below 68 K and between 360 - 420 K. The antiferromagnetic state which exists at intermediate temperatures between two ferromagnetically ordered regimes consists of an incommensurate spin density wave (SDW) order likely caused by RKKY interactions. The effect of magnetic fields and pressure on the magnetic states of this complex material were explored.

Chapter 1
Introduction

The couplings of charge carries and local moments can have different forms and strengths. They could act as the Kondo effect[18] that charge carrier moments screen the local moments or as in Ruderman-Kittel-Kasuya-Yosida (RKKY) interaction[16;32;40], where local moments indirectly coupled via the conduction electrons. These interactions generally play important roles in determining low temperature material physical properties. In the work reported on here, we focus on two cases involving such interactions to investigate the mechanisms behind material properties. The first is a carrier-doped strongly correlated Kondo insulator that displays a field dependent non-Fermi-Liquid (non-FL) behavior. The next is an itinerant antiferromagnet (IAFM) where charge carriers and local moments coupling acts to create a long range modulation resulting in a spin-density-wave (SDW) magnetically ordered state.

1.1 Fermi-Liquid Theory and Non-Fermi-liquid Behavior

The theories of Drude and Sommerfield[3] employs the free electron gas as an approximation for electrons in metals. It is successful in explaining properties such as Ohm's law in the resistivity of metals and the linear temperature term in low temperature specific heat of alkali metals. However, limited by the non-interacting-free-electron approximation, it fails in many ways especially in transition metal system and rare earth materials where correlated electron effects are crucial in determining material properties.

In 1957, L. D. Landau[21] proposed the Fermi-Liquid (FL) theory to describe the low temperature properties of metals which includes many of the effects of the interaction betweens electrons. The central assumption of this theory is that charge carriers can be described as weakly interacting *quasiparticles* which are electrons "dressed" in interaction clouds resulting in fermionic particles of effective mass m^*. These quasiparticles fill up energy levels up to the Fermi surface at $T = 0$ and form the Fermi sea in the ground state. The quasiparticles at the Fermi level have a long lifetime and dominate most of the electronic material properties[13].

1.1.1 Fermi-Liquid Theory

The energy of a quasiparticle is given by the free particle expression

$$\epsilon(p) = \frac{|\vec{p}|^2}{2m^*}, \tag{1.1}$$

where m^* is the effective mass. At zero temperature, all non-interacting quasiparticles states $|\vec{p}\sigma\rangle$ have $|\vec{p}| < p_F$ and $\sigma = \pm\frac{1}{2}$ are occupied with a distribution function $n(\vec{p}, \sigma) = 1$ and all $|\vec{p}| > p_F$ states are empty with $n(\vec{p}, \sigma) = 0$. When there is a small change of distribution function δn, with the fermionic feature of the quasiparticles being included, the change in energy is

$$\delta E = S_{\sigma'} \int f(\vec{p}, \sigma; \vec{p}^{\,'}, \sigma^{'}) \delta n d\tau_p, \tag{1.2}$$

where $d\tau_p = dp_x dp_y dp_z/(2\pi\hbar)^3$ and S_α represent the the spin states parameter. $f(\vec{p}, \sigma; \vec{p}^{\,'}, \sigma^{'})$ corresponds to the scattering amplitude the two quasiparticles ($|\vec{p}\sigma\rangle$ and $|\vec{p}^{\,'}\sigma^{'}\rangle$) and obeys the time reversal symmetry.

The entropy of the liquid from quantum statistics is:

$$S = -S_{\sigma'} \int n_{\vec{p}} ln(n_{\vec{p}}) + (1 - n_{\vec{p}}) ln(1 - n_{\vec{p}}) d\tau_p. \tag{1.3}$$

Here n follows the Fermi-Dirac distribution,

$$n_{\vec{p}} = \frac{1}{\exp((\epsilon_{\vec{p}} - \mu_F)/k_B T) + 1}. \tag{1.4}$$

With the change of the density states, one would have

$$\delta S = \frac{1}{T}\int (\epsilon_{\vec{p}} - \mu_F)\delta n_{\vec{p}} d\tau_p \backsimeq {k_B}^2 N_F(0)\frac{\pi^2}{3}\delta T + O(T^2), \tag{1.5}$$

$N_F(0)$ is the density of state at Fermi-level at zero temperature

$$N_F(0) = \frac{V_F}{2\pi^2}\sqrt{\epsilon_{\vec{p}}\left(\frac{2m^*}{\hbar^2}\right)^3}. \tag{1.6}$$

V_F is the volume of the Fermi surface sphere. Hence, one can have

$$\delta S = \frac{m^* k_F}{3\hbar^2}{k_B}^2 \delta T, \tag{1.7}$$

and

$$C_V = T\left(\frac{\partial S}{\partial T}\right)_V = \frac{m^* k_F}{3\hbar^2}{k_B}^2 T. \tag{1.8}$$

The resistivity in the quasiparticle theory can have a form similar to the Drude model with lifetime τ and m^*:

$$\rho = \frac{m^*}{ne^2\tau}. \tag{1.9}$$

In a system with stronger electron-electron ($e-e$) correlations, $e-e$ interaction need to be considered in determining τ. With the $e-e$ inelastic scatterings considered, the scattering length $\ell = {\tau_{ee}}^{-1}$ of 3D system has the form of $\ell \sim T^2$. As a result, at low temperatures the resistivity takes on the form

$$\rho = \rho_0 + mT^2, \tag{1.10}$$

where ρ_0 is the residual resistivity due to impurity scattering.

The FL explanation describes most common metals very well and also describes the properties of ^{3}He. ^{3}He is the decay product of tritium and is a fermion with

$S = \frac{1}{2}$. At low temperature where ^{3}He is a normal (nonsuperfluid) liquid, there is a linear specific heat in temperature[39]. Even heavy fermion metals such as UPt_3[36] and $CeAl_3$[1] act as FL except that they have a rather large m^* due to the vastly renormalized (by up to 3 orders of magnitude by the interaction) effective mass (m^*). Fig. 1.1 shows an example of $U_{1-x}Y_xPt_3$. Despite the T_c decreasing with doping concentration increasing, the resistivity of $U_{1-x}Y_xPt_3$ clearly follows the FL rule of $\rho \sim T^2$ in the normal state.

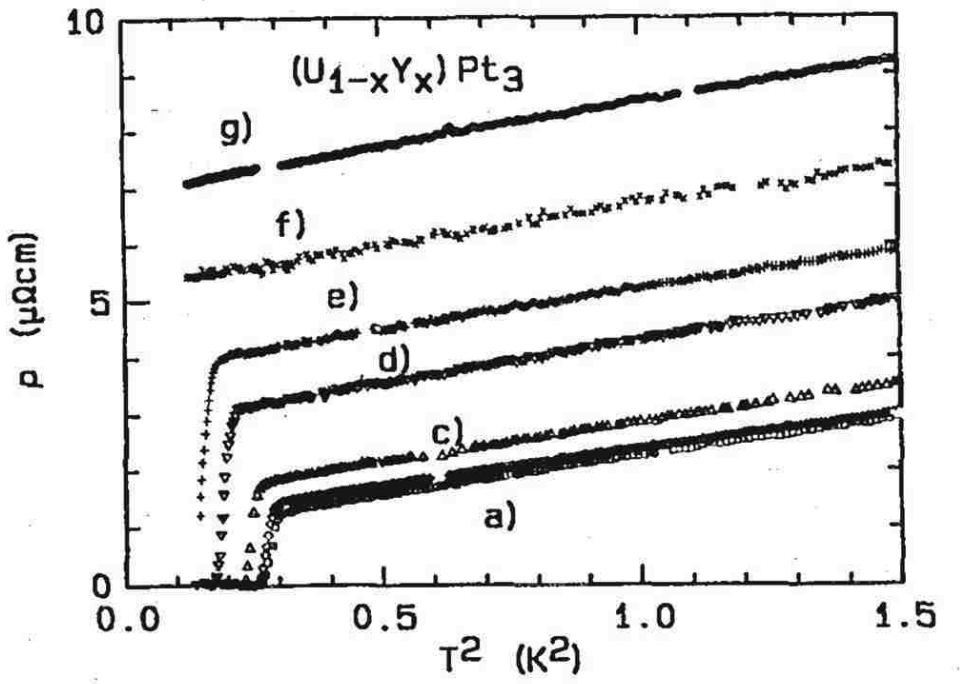

FIGURE 1.1: Resistivity of $U_{1-x}Y_xPt_3$,with x from 0 to 0.5% (from a to g) exhibits a quadratic temperature dependence[36] at normal state.

1.1.2 Disordered Fermi-Liquid

The framework of FL theory is not limited to the clean metal systems[26], but can be modified to describe finite size systems and disordered systems. Systematic studies of interaction and disorder correlations started in the last century[23] and obtained great success. The greatest advances were made in the regime of weak disorder,

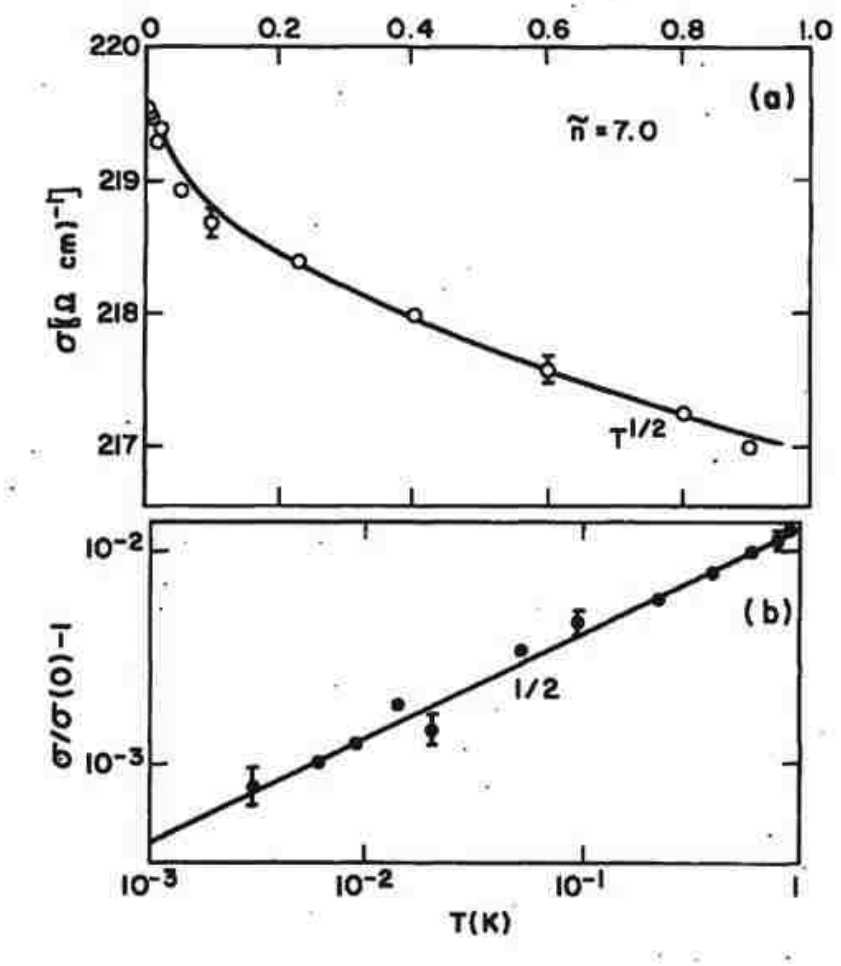

FIGURE 1.2: Resistivity of Si:P exhibits a $\rho \sim T^{\frac{1}{2}}$ dependence as expected for a disordered Fermi-liquid[30].

where controlled many-body calculations are possible using the disorder strength as a parameter[23].

Treatments of disordered systems began with the 'scaling description of the Anderson localization problem' and the diffusive electrons in the presence of a random potential[23]. With the random phase renormalization and scaling theory, significant modifications were made to the traditional FL theory of metals leading to disordered FL theory. This theory is applied mostly in the heavily doped semiconductors

systems[23;26;30] while other metallic systems with weak disorder, i.e. the epitaxial graphene[22], also can be described in the framework .

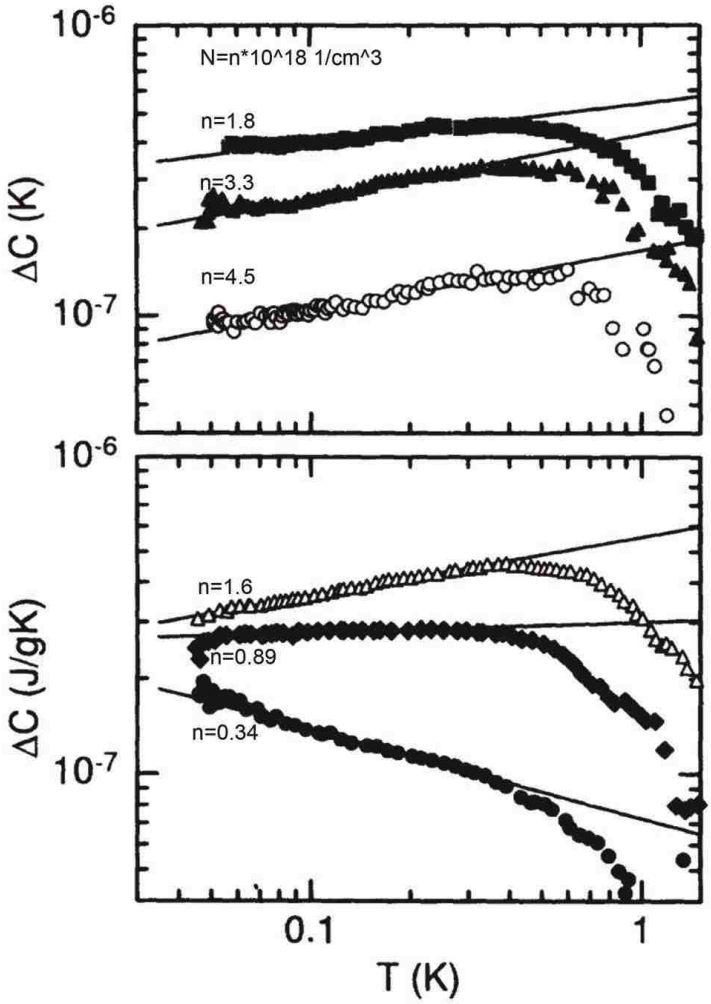

FIGURE 1.3: Specific heat of Si:P exhibits a power law $C_v = \gamma T + \beta T^3 + mT^\alpha$ dependence with $\alpha = 0.2$ in the metallic region[20].

In disordered systems where the scaling rule is valid[26], the conductivity of the metallic phase at low temperature yields the form:

$$\sigma(T) \sim t^\mu \phi_\sigma\Big(\frac{T}{t^{\mu z}}\Big) \tag{1.11}$$

where $t = (n - n_c)/n_c$ is the dimensionless distance from the transition, $\phi_\sigma(x)$ is the scaling function and $\mu = (d-2)\nu$. Other parameters are the dimensions of the

system d, the correlation length exponent ν and the dynamical exponent z. At finite temperature, $\phi_\sigma(x)$ can be expanded in the metallic phase:

$$\phi_\sigma(x) \approx 1 + ax^\alpha \tag{1.12}$$

which leads the low T conductivity

$$\sigma(t,T) \approx \sigma_0(t) + m_\sigma(t)T^\alpha \tag{1.13}$$

where $\sigma_0(t) \sim t^\mu$ and $m_\sigma(t)$ is also a function of t ($m \sim t^{\mu-\alpha\nu z}$).

The exponent α is a universal value in the metallic phase under the scaling treatment. Under the condition of weak disorder, it is found to be $\alpha = 1/2$. It was clearly demonstrated by Rosenbaum *et al* that in the heavily doped semiconductor Si:P near an insulator to metal transition (IMT) the conductivity at $T < 1$ K is well defined with a square root dependence of temperature[30] as shown in Fig. 1.2.

An analogy can be used in the treatment of the specific heat which leads to a power law form of the low temperature specific heat.

$$C_v \approx \gamma_0(t)T + m_\gamma(t)T^{\alpha+1} \tag{1.14}$$

The specific heat of the Si:P can be fit to a power law dependence of T (Fig. 1.3), with a constant α derived from data in the metallic phase.

DiTusa *et al* have investigated Al doped FeSi to compare with the case of Si:P[7;8]. They found that FeSi is similar to silicon after renormalization of the carrier mass, in analogy to the heavy fermion metals that behave as a FL with large effective mass. In this context, the behavior of doped FeSi after IMT should follow the rule of disordered FL theory, which has $T^{1/2}$ dependence of conductivity (Fig. 1.4).

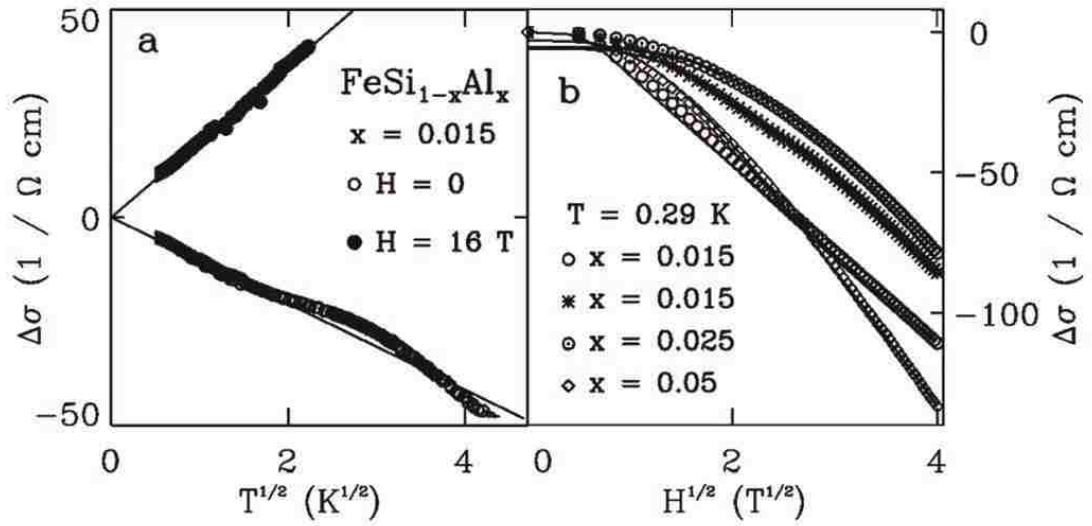

FIGURE 1.4: Conductivity of $Fe_{1-x}Al_xSi$ has a $\rho \sim T^{\frac{1}{2}}$ dependence as a disordered Fermi-liquid[7].

The effective mass is large, in the case of $Fe_{1-x}Al_xSi$, a m^*/m_e ratio of 14 ± 2 is derived from the free electron theory. This study showed that though the higher temperature properties can be largely affected by strong correlation effects, the intrinsic properties of ground state of the heavy fermion metals and doped strongly correlated insulators can still be described in the framework of the FL theory.

1.1.3 Non-Fermi-Liquid Behavior

Materials with anomalous temperature dependences in low-temperature properties are considered as non-FL. Such materials include high T_c cuprate superconductors[12] and some heavy-fermion systems on the verge of magnetic ordering[37;41]. The emergence of non-FL behavior indicates singular Fermi surface or Fermi surface reconstruction or even the critical condition that the entire Fermi surface disappears as in cuprate superconductors[5;6;34]. As a result, the necessary environment for Laudau's quasiparticles is destroyed and the system can no longer be explained with FL theory. Due to the complexity of the problem, it has proven to

be difficult to build a theory for such systems though non-FL behavior has been observed in a large category of materials experimentally.

Non-Fermi-Liquid Heavy Fermion Systems

Non-FL behaviors are frequently found in the Ce-, Yb-, and U-based heavy-

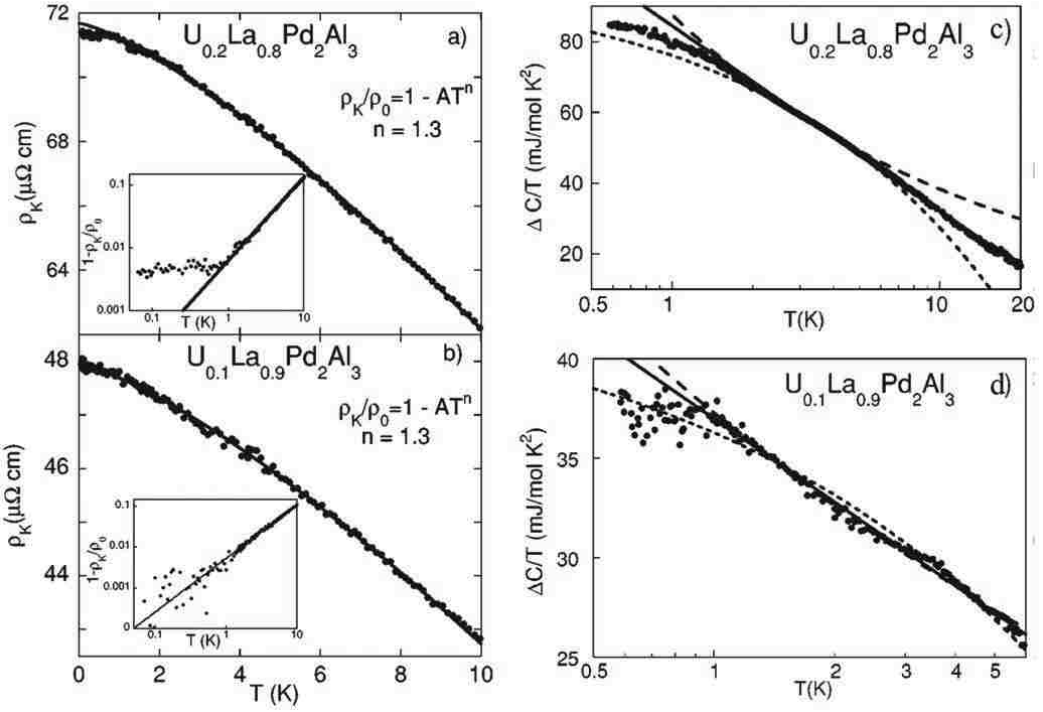

FIGURE 1.5: The Uranium-based heavy-Fermion system, $U_xLa_{1-x}Pd_2Al_3$, displays anomalous T dependence on resistivity ρ and $logT$ dependence of specific heat $\Delta C/T$ (Solid line fitting)[41].

fermion intermetallic compounds. These systems have strong correlations because of the interacting f electrons. These materials are often close to a quantum critical point that can be tuned with doping or external parameters such as pressure or magnetic field[37]. Studies of the non-FL behavior of these systems have extended for a few decades[26;37]. There has been a considerable amount of experimental data to motivate a phenomenological description of the behavior quantum critical systems such as the temperature dependences of the electronic resistivity $\rho(T)$, the specific

heat $C(T)$ and the magnetic susceptibility $\chi(T)$[41]. For the temperature dependence of the electrical resistivity $\rho(T)$, there is

$$\rho(T) \sim 1 - m(T/T_0)^n, \tag{1.15}$$

where m can be positive or negative with $|m| \sim 1$ and $n \sim 1 - 1.5$. While the specific heat and susceptibility can have more than one temperature dependent form,

$$C(T)/T \sim \left(-\frac{1}{T_0}\right) ln\left(\frac{T}{T_0}\right) \quad or \quad \sim T^{-1+\lambda} \tag{1.16}$$

and

$$\chi(T) \sim 1 - \left(\frac{T}{T_0}\right)^{1/2}, \quad \left(-\frac{1}{T_0}\right) ln\left(\frac{T}{T_0}\right) \quad or \quad \sim T^{\lambda}. \tag{1.17}$$

Here λ is typically between 0.7 and 0.8 and the characteristic temperature T_0 is identified with Kondo temperature.

An example is shown here to demonstrate the resistivity and specific heat of $U_xLa_{1-x}Pd_2Al_3$ at low temperature (Fig. 1.5). From Fig. 1.5. a) and b), the power law coefficient $n = 1.3$ as $\rho \sim -T^n$ implies that the system is a non-FL over the measured temperature. Fig. 1.5. c) and d) displays the specific heat where a log T dependence is apparent.

Pressure Driven Non-Fermi-Liquid MnSi

MnSi has a cubic B20 structure which lacks of center-inversion symmetry (space group $P2_13$). Below T_c=29.5 K, the magnetic moments of MnSi tend to form a long-wavelength helix under the influence of the chiral spin-orbital interaction. As a materials with a rather simple structure where the Dzyaloshinsky - Moriya (DM) interaction interaction is active, MnSi is one of the most extensively studied materials driven by both theoretical and experimental interest. Non-FL behavior of

MnSi under 14.6 kbar pressure was reported by Pfleiderer *et al* in 2001[27] (Fig. 1.6). It was discovered that below the critical pressure, the resistivity followed a $T^{3/2}$ dependence of a non-FL rather than the T^2 dependence of a FL. Neutron scattering studies found that the helimagnetic spiral is unlocked so that it is only partially long range ordered within the non-FL state. This suggests an unusual microscopic origin of the non-FL phase in this system[28].

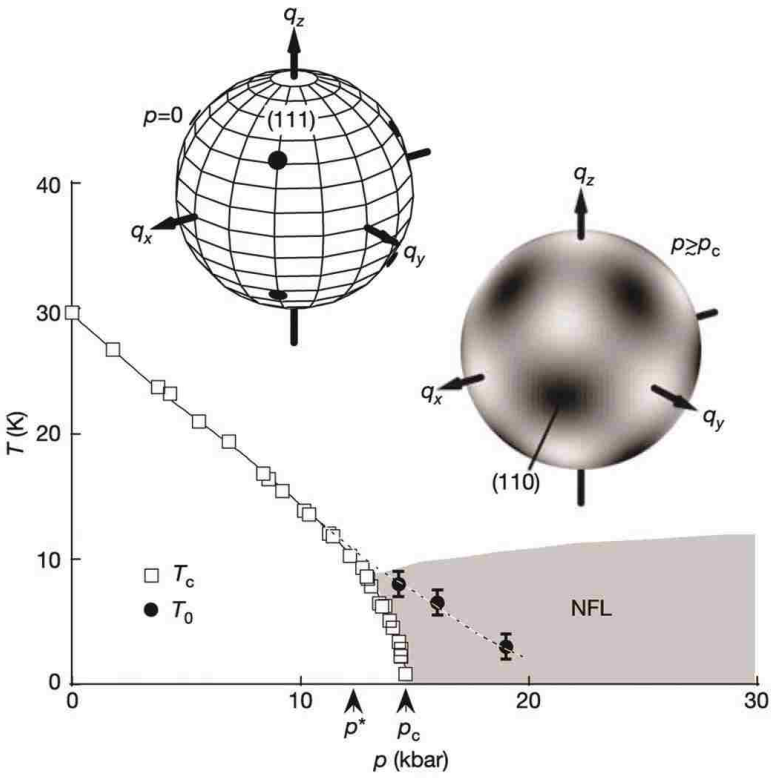

FIGURE 1.6: Schematic temperature versus pressure phase diagram of MnSi[28].

Investigations on MnSi also identified an **A**-phase in the conical magnetically ordered region of the phase diagram where a topological lattice structure, called a skyrmion lattice, was first observed in magnetic materials[31]. Theoretical studies reported that partial order is often related with the topological spin textures. These findings raised interest in investigating the connection of non-FL resistivity

behavior with the topological spin properties. A more recent study was dedicated to this topic and revealed its nature under pressures and fields as a topological non-FL[29] (Fig. 1.7). They discovered that the topological Hall signal is associated with the non-FL behavior of MnSi. The topological Hall effect is a Hall effect contribution that doesn't depends on either the magnetic field or the magnetization. It is a signature of the skyrmion state or the A-phase in this system. The intrinsic mechanism of the $T^{3/2}$ non-FL behavior was illustrated as the topological winding of skyrmions. This non-trivial spin structure induced topological non-FL may be generated from the chirality of the DM spin-orbital coupling.

1.2 Neutron Scattering Investigation of Itinerant Antiferromagnetism

The theoretical perspective of itinerant magnetism starts from Stoner's model. Here the local imbalance of up- and down-spins of conduction electrons are considered with the temperature dependence of the Fermi-Dirac distribution[17]. Stoner's model successfully predicts a magnetic ground state but often gives very large T_c in comparison to experimental results. Recent progress on Stoner's model with Heisenberg Hamiltonian has improved it so that it can give a reasonable T_c for $3d$ electron magnets[33].

Neutron scattering is a commonly used experimental technique and a powerful tool for studying magnetism. Neutrons are particles with mass m=1.675$\times 10^{-27}$ kg, spin $1/2\hbar$ and no charge. Neutrons penetrate deep into the materials instead of probing just a small region near the surface. Thermal neutrons have a de Broglie wavelength comparable to typical inter-atomic distances. Thus, neutron scattering is a probe for determining magnetic and nuclear structures as well as for studying nuclear and magnetic thermal excitations with energy of 0.1 - 100 meV. In ad-

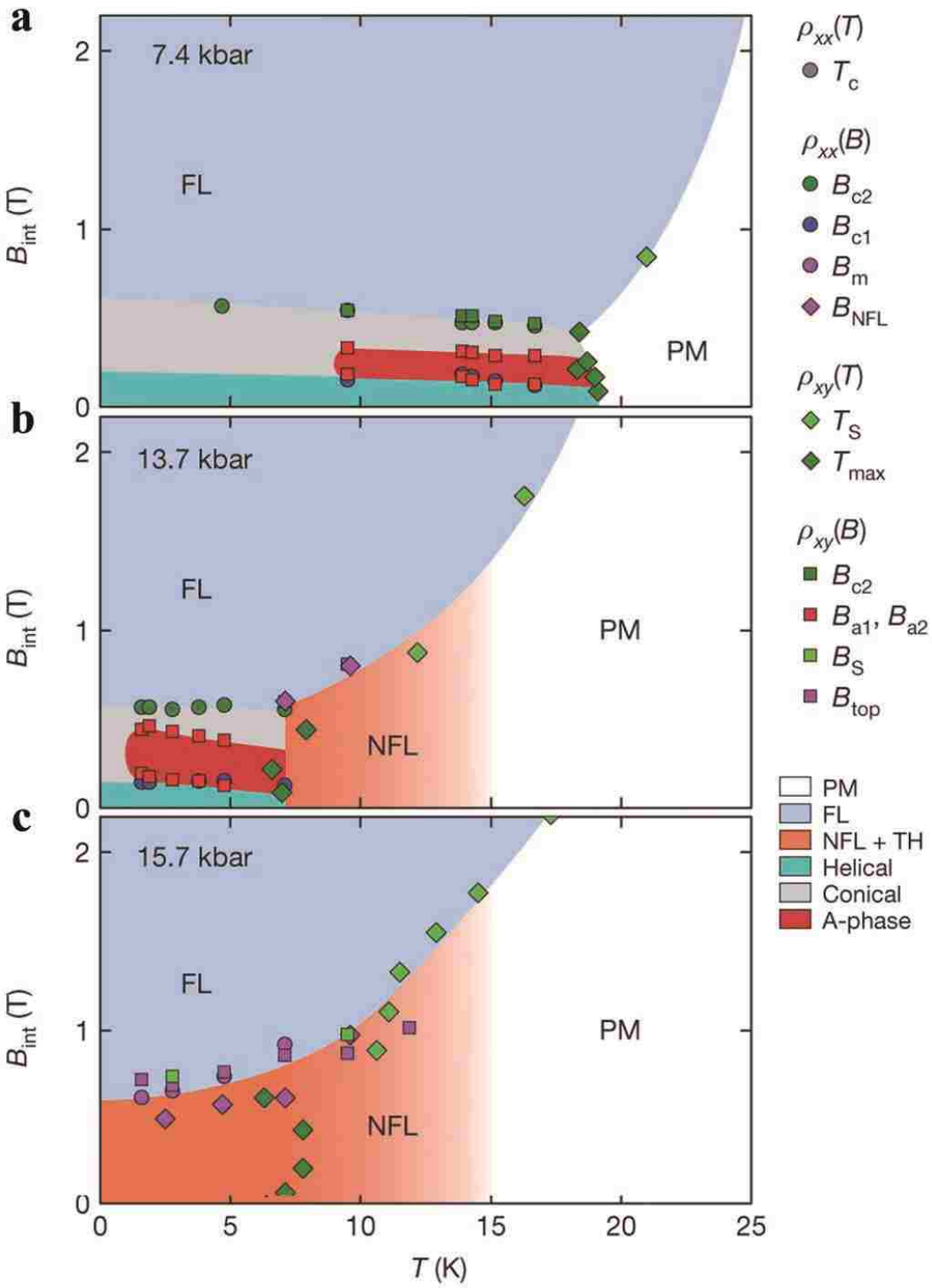

FIGURE 1.7: Magnetic phase diagrams of MnSi at 7.4 kbar, 13.7 kbar and 15.7 kbar displaying the topological Hall effect and non-Fermi-Liquid resistivity .

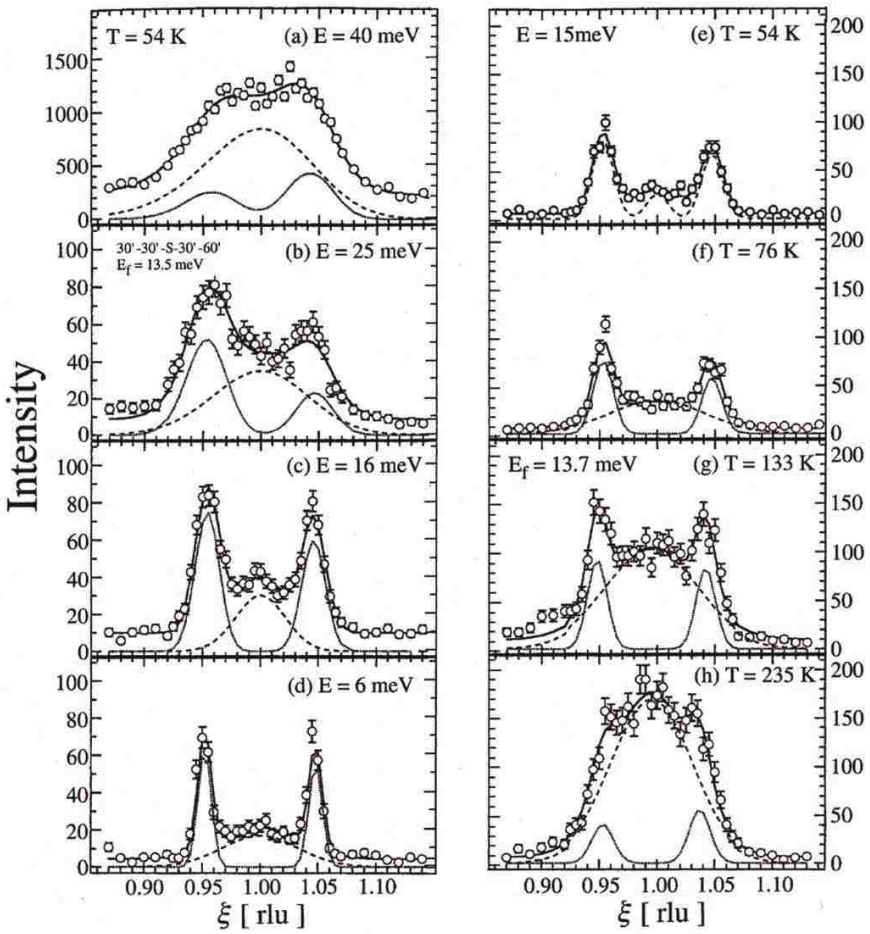

FIGURE 1.8: Neutron magnetic scattering intensity of Cr near (1, 0, 0) plane[19]. The various energies scans are at $T = 54$ K (a, b, c and d) and the $E = 15$ meV scans are at different temperatures (e, f, g and h). The dashed and light lines fit to conmmensurate charge-density-wave and incommensurate spin-density-wave components.

dition, neutron spins interact with electron spins through a strong dipole-dipole interaction allowing the scattering to reflect the local magnetic environment in materials.

Experimentally discovered itinerant ferromagnetic (FM) or antiferromagnetic (AFM) materials are mostly transition metal or Rare Earth metal containing compounds. The most extensively studied IAFM system is chromium, which displays a incommensurate SDW ordered ground state[9;19](Fig. 1.8). Fig. 1.9 displays a SDW structure scheme picture of Cr identified with neutron scattering. The wavevector

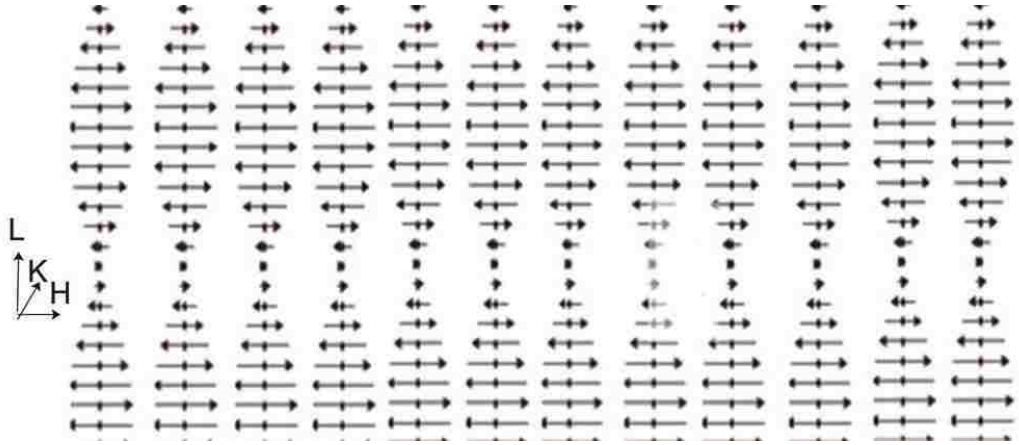

FIGURE 1.9: Scheme image of the spin-density-wave of Cr propagates along H direction[35].

of the SDW is $k = (2\pi/a)(1-\delta, 0, 0)$ with a being the lattice constant and δ is temperature dependent. At the *Néel temperature*, $T_N = 312$ K, $\delta = 0.037$. The nearest neighbors interact antiferromagnetically in the SDW state. When $T = T_N$, the temperature dependent resistivity displays a cusp[2]. The sudden resistivity increase indicates the loss of charge carrier density as a gap opens at the Fermi surface. This feature is associated with the SDW ordering in Cr and is a common feature of *band antiferromagnets*[4]. MnSi is another heavily investigated system as weak itinerant ferromagnet[14].

Besides $3d$ transition metal compounds, there are also f electron metal compounds belonging to the catagory of IAFM, for example, $UPtGa_5$ and $UNiGa_5$[15]. Neutron scattering results revealed that large spin-orbit coupling induced substantial magnetostriction around T_N along the easy-axis direction in these itinerant systems (Fig. 1.10). Similar to UGa_3, the orbital magnetic moment is strongly suppressed due to the hybridization of Uranium $5f$ and Ga-$4p$ electron states. Rare earth materials like GdSi also exhibits properties of an IAFM[10;11].

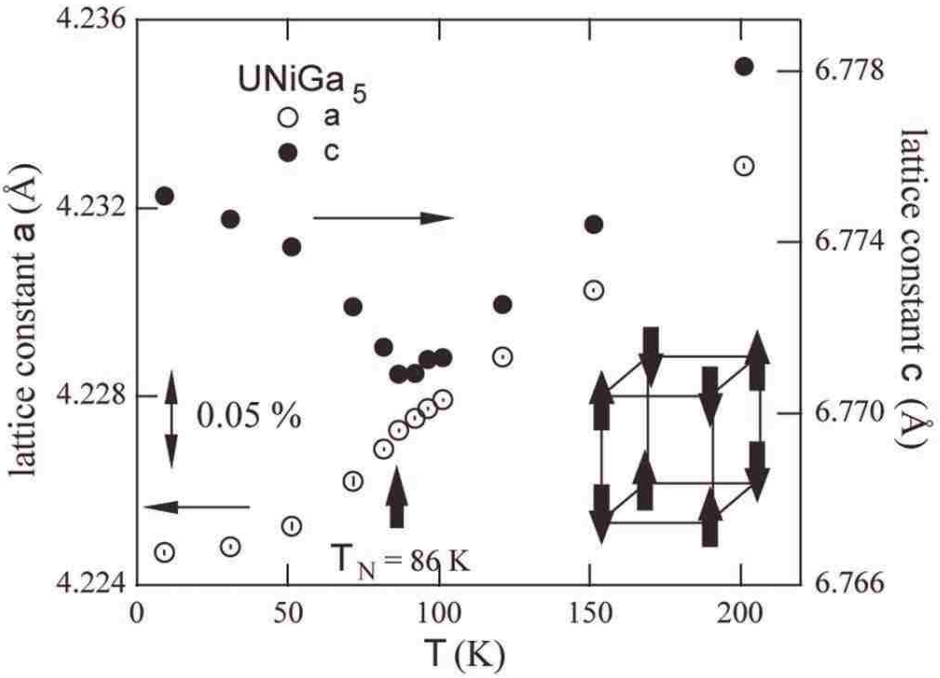

FIGURE 1.10: Lattice constant vs. temperature plot of $UNiGa_5$ [15].

Though the majority of the itinerant magnets contain elements that contribute a definite magnetic moment, a few materials with no magnet constituents are also found to behave like an itinerant manget [24;25;38]. TiAu is a recently reported IAFM that contains no obvious magnetic constituents. It is first identified in a band structure calculation survey (using a full-potential DFT with taking spin-orbit coupling) [38]. Several experiments including magnetic, transport, specific heat and neutron scattering experiments confirmed that a long range AFM order exists in the full volume of this itinerant system. This finding enriches our knowledge of the weak IAFM and provides insights in understanding the microscopic interaction pictures of the localized and itinerant moment systems.

1.3 Outline of Our Work

In this work, I focus on the non-FL behavior investigation in the $Fe_{1-y}Co_ySi$ system and neutron scattering studies of the IAFM Fe_3Ga_4. I began chapter 1 with a short introduction on FL, disordered FL and non-FL behaviors as well as itinerant

magnets. Chapter 2 concerns the experimental techniques and common models of magnetic, transport and thermodynamic properties related to our studies of $Fe_{1-y}Co_ySi$ and Fe_3Ga_4.

The following two chapters discussed the experimental studies of the $Fe_{1-y}Co_ySi$ system where we discovered a field depended non-FL behavior that shares the same mechanism as previously discovered in Mn doped FeSi.

. Chapter 3 includes a review of the previous studies of Co and Mn doped FeSi. This followed by a summary on the sample preparation processes and the discussion of our experimental results on the magnetic properties of $Fe_{1-y}Co_ySi$, $0 \leq y < 0.1$. We observed a systematic increase of the Weiss temperature from Mn through to Co doping. The Θ_w remains negative for small y of $Fe_{1-y}Co_ySi$. We have found that the impurity moment in the low doping range of the $Fe_{1-y}Co_ySi$ is $S = 1$, similar to what was found in Mn substituted FeSi. This suggests that there may be a similar interaction of the magnetic moments with conducting charge carriers in the very low doping region of Co and Mn doped FeSi.

Chapter 4 continues the investigation of Co doped FeSi concentrating on our transport and specific heat results. The conductivity of $Fe_{1-y}Co_ySi$ $0 \leq y < 0.03$ clearly indicates a field depended non-FL behavior near IMT as previously discovered in $Fe_{1-x}Mn_xSi$. The magnetoresistance studies are also similar to that seen in $Fe_{1-x}Mn_xSi$ while largely different from a heavily doped semiconductor (disordered FL) near IMT. Specific heat measurements indicated that a large amount of entropy is released from the system at very low temperatures - i.e. below our lowest temperature measured (0.3 K). This phenomenon confirmed the existence of the underscreen magnetic moments at very low temperature. These findings

support the idea that the same mechanism for non-FL is at play in FeCoSi as was previously proposed for Mn doped FeSi, the underscreened Kondo model.

In Chapter 5, I discuss the investigation of the magnetic structure of Fe_3Ga_4 with neutron scattering techniques. Following an introduction, I summarized the sample preparation and experimental detail. Then I presented the refinement and magnetic structure rendering process before focusing on the results and discussion of the neutron scattering investigation on Fe_3Ga_4. A FM ordered state is confirmed below 68 K and between 360 - 420 K. The intermediate temperature magnetic structure of Fe_3Ga_4 was determined to be an incommensurate SDW. The SDW state is propagating along the c-axis with the magnetic moments lying mostly in the a-axis direction. Considerable non-coplanar moments were found in the b-axis direction which is consistent with our previous Hall effect measurements. Neutron scattering in field of $H = 0.5$ T revealed that the SDW coexists with the high temperature FM state.

1.4 Bibliography

[1] K. Andres, J. E. Graebner, and H. R. Ott. $4f$-virtual-bound-state formation in $CeAl_3$ at low temperatures. *Phys. Rev. Lett.*, 35:1779–1782.

[2] Sigurds Arajs, R. Aidun, and C. A. Moyer. Antiferromagnetism and electrical resistivity of dilute chromium-germanium alloys. *Phys. Rev. B*, 22:5366–5368, 1980.

[3] N.W. Ashcroft and N.D. Mermin. *Solid State Physics*. Saunders College, Philadelphia, 1976.

[4] Jr. Charles P. Poole. *Encyclopedic Dictionary of Condensed Matter Physics*. Academic Press, Science, 2004.

[5] P Coleman, C Ppin, Qimiao Si, and R Ramazashvili. How do Fermi liquids get heavy and die? *Journal of Physics: Condensed Matter*, 13(35):R723, 2001.

[6] Tanmoy Das, R. S. Markiewicz, and A. Bansil. Emergence of non-Fermi-liquid behavior due to Fermi surface reconstruction in the underdoped cuprate

superconductors. *Phys. Rev. B*, 81:184515, 2010.

[7] J. F. DiTusa, K. Friemelt, E. Bucher, G. Aeppli, and A. P. Ramirez. Metal-insulator transitions in the kondo insulator FeSi and classic semiconductors are similar. *Physical Review Letters*, 78(14):2831–2834, 1997.

[8] J. F. DiTusa, K. Friemelt, E. Bucher, G. Aeppli, and A. P. Ramirez. Heavy fermion metalkondo insulator transition in $FeSi_{1-x}Al_x$. *Physical Review B*, 58 (16):10288–10301, 1998.

[9] Eric Fawcett. Spin-density-wave antiferromagnetism in chromium. *Reviews of Modern Physics*, 60(1):209–283, 1988.

[10] Yejun Feng, Jiyang Wang, D. M. Silevitch, B. Mihaila, J. W. Kim, J.-Q. Yan, R. K. Schulze, Nayoon Woo, A. Palmer, Y. Ren, Jasper van Wezel, P. B. Littlewood, and T. F. Rosenbaum. Incommensurate antiferromagnetism in a pure spin system via cooperative organization of local and itinerant moments. *Proceedings of the National Academy of Sciences*, 110(9):3287–3292, 2013.

[11] Yejun Feng, Jiyang Wang, A. Palmer, J. A. Aguiar, B. Mihaila, J. Q. Yan, P. B. Littlewood, and T. F. Rosenbaum. Hidden one-dimensional spin modulation in a three-dimensional metal. *Nat Commun*, 5, 2014.

[12] M. Gurvitch and A. T. Fiory. Resistivity of $La_{1.825}Sr_{0.175}CuO_4$ and $YBa_2Cu_3O_7$ to 1100 K: Absence of saturation and its implications. *Physical Review Letters*, 59(12):1337–1340, 1987.

[13] Thomas Ihn. *Electronic Quantum Transport in Mesoscopic Semiconductor Structures*, chapter Electron-electron interactions within the Fermi-liquid concept, pages 29–34. Springer New York, New York, NY, 2004.

[14] Y. Ishikawa. Neutron scattering studies of itinerant electron magnetism. *Journal of Applied Physics*, 49(3):2125–2130, 1978.

[15] Koji Kaneko, Naoto Metoki, Gerard H. Lander, Nicholas Bernhoeft, Yoshihumi Tokiwa, Yoshinori Haga, Yoshichika nuki, and Yoshinobu Ishii. Neutron diffraction study of $5f$ itinerant antiferromagnet $UPtGa_5$ and $UNiGa_5$. *Physica B: Condensed Matter*, 329333, Part 2:510 – 511, 2003.

[16] T. Kasuya. A theory of metallic ferro- and antiferromagnetism on zener's model. *Prog. Theor. Phys.*, 16:45–57, 1956.

[17] Jürgen Kübler. *Theory of Itinerant Electron Magnetism*. Oxford Science Publication, Clarendon, Oxford, 2000.

[18] Leo Kouwenhoven and Leonid Glazman. Revival of the kondo effect. *Physics World*, 14(1):33, 2001.

[19] N. I. Kulikov and V. V. Tugushev. Spin-density waves and itinerant antiferromagnetism in metals. *Soviet Physics Uspekhi*, 27(12):954, 1984.

[20] M. Lakner, H. v. L öhneysen, A. Langenfeld, and P. Wölfle. Localized magnetic moments in Si : P near the metal-insulator transition. *Phys. Rev. B*, 50:17064–17073, 1994.

[21] L. D. Landau. The theory of a Fermi liquid. *Soviet Physics JETP*, 3(6):920, 1957.

[22] Samuel Lara-Avila, Alexander Tzalenchuk, Sergey Kubatkin, Rositza Yakimova, T. J. B. M. Janssen, Karin Cedergren, Tobias Bergsten, and Vladimir Fal'ko. Disordered Fermi liquid in epitaxial graphene from quantum transport measurements. *Phys. Rev. Lett.*, 107:166602, 2011.

[23] Patrick A. Lee and T. V. Ramakrishnan. Disordered electronic systems. *Rev. Mod. Phys.*, 57:287–337, 1985.

[24] B. T. Matthias and R. M. Bozorth. Ferromagnetism of a zirconium-zinc compound. *Phys. Rev.*, 109:604–605, 1958.

[25] B. T. Matthias, A. M. Clogston, H. J. Williams, E. Corenzwit, and R. C. Sherwood. Ferromagnetism in solid solutions of scandium and indium. *Phys. Rev. Lett.*, 7:7–9, 1961.

[26] E. Miranda and V. Dobrosavljevic. Disorder-driven non-Fermi liquid behavior of correlated electrons. *Reports on Progress in Physics*, 68(10):2337, 2005.

[27] C. Pfleiderer, S. R. Julian, and G. G. Lonzarich. Non-Fermi-liquid nature of the normal state of itinerant-electron ferromagnets. *Nature*, 414(6862): 427–430, 2001.

[28] C. Pfleiderer, D. Reznik, L. Pintschovius, H. v Lohneysen, M. Garst, and A. Rosch. Partial order in the non-Fermi-liquid phase of MnSi. *Nature*, 427 (6971):227–231, 2004.

[29] R. Ritz, M. Halder, M. Wagner, C. Franz, A. Bauer, and C. Pfleiderer. Formation of a topological non-Fermi liquid in MnSi. *Nature*, 497(7448):231–234, 2013.

[30] T. F. Rosenbaum, R. F. Milligan, M. A. Paalanen, G. A. Thomas, R. N. Bhatt, and W. Lin. Metal-insulator transition in a doped semiconductor. *Physical Review B*, 27(12):7509–7523, 1983.

[31] U. K. Roszler, A. N. Bogdanov, and C. Pfleiderer. Spontaneous skyrmion ground states in magnetic metals. *Nature*, 442(17):797, 2006.

[32] M. A. Ruderman and C. Kittel. Indirect exchange coupling of nuclear magnetic moments by conduction electrons. *Phys. Rev.*, 96:99–102, 1954.

[33] L. M. Sandratskii, R. Singer, and E. Şaşıoğlu. Heisenberg hamiltonian description of multiple-sublattice itinerant-electron systems: General considerations and applications to NiMnSb and MnAs. *Phys. Rev. B*, 76:184406, 2007.

[34] T. Senthil. Critical Fermi surfaces and non-Fermi liquid metals. *Phys. Rev. B*, 78:035103, 2008.

[35] O. G. Shpyrko, E. D. Isaacs, J. M. Logan, Yejun Feng, G. Aeppli, R. Jaramillo, H. C. Kim, T. F. Rosenbaum, P. Zschack, M. Sprung, S. Narayanan, and A. R. Sandy. Direct measurement of antiferromagnetic domain fluctuations. *Nature*, 447(7140):68–71, 2007.

[36] J. L. Smith, M. C. Aronson, S. E. Brown, and A. L. Giorgi. Impurity effects in UPt_3. *Physica B: Condensed Matter*, 163(1):129–130, 1990.

[37] G. R. Stewart. Non-Fermi-liquid behavior in d- and f-electron metals. *Reviews of Modern Physics*, 73(4):797–855, 2001.

[38] E. Svanidze, Jiakui K. Wang, T. Besara, L. Liu, Q. Huang, T. Siegrist, B. Frandsen, J. W. Lynn, Andriy H. Nevidomskyy, Monika B. Gamza, M. C. Aronson, Y. J. Uemura, and E. Morosan. An itinerant antiferromagnetic metal without magnetic constituents. *Nat Commun*, 6, 2015.

[39] Dieter Vollhardt. Normal ^{3}He an almost localized Fermi liquid. *Reviews of Modern Physics*, 56(1):99–120, 1984.

[40] K. Yosida. Magnetic properties of $Cu - Mn$ alloys. *Phys. Rev.*, 106:893–898, 1957.

[41] V. S. Zapf, R. P. Dickey, E. J. Freeman, C. Sirvent, and M. B. Maple. Magnetic and non-Fermi-liquid properties of $U_{1-x}La_xPd_2Al_3$. *Physical Review B*, 65(2): 024437, 2001.

Chapter 2

Magnetic, Transport and Thermodynamic Properties: Models and Experimental Detail

2.1 Magnetic Property

2.1.1 Susceptibility and Magnetization Models

In the local moment picture of magnetism, exchange interactions between local moments on individual atoms contribute to the long-ranged magnetic order. The magnetization of paramagnetic materials derived from Boltzmann statistics is in the form[2]:

$$M(H,T) = N_A g J \mu_B B_J(x). \tag{2.1}$$

N_A is the electron density and J is the size of the magnetic moment. B_J is the Brillouin function:

$$B_J(x) = \frac{2J+1}{2J} coth[\left(\frac{2J+1}{2J}\right)x] - \frac{1}{2J} coth[\frac{x}{2J}], \tag{2.2}$$

with

$$x = \frac{\mu B}{k_B T} = \frac{g J \mu_B H}{k_B T}. \tag{2.3}$$

At the high temperature limit, $\lim_{x\to 0} B_J(x) = [(J+1)/3J]x$. This leads to $M(H,T) = NgJ(J+1)\mu_B H/3k_B T$. As a result, the susceptibility χ yields the Curie's law

$$\chi = \frac{M}{H} = \frac{C}{T}. \tag{2.4}$$

C is the Curie constant:

$$C = \frac{N_A}{3}\frac{(g\mu_B)^2}{k_B} J(J+1). \tag{2.5}$$

While at the high field limit, $\lim_{x\to\infty} B_J(x) = 1$, which gives the saturate magnetization $M(H,T) = N_A g \mu_B J$.

In the ferromagnetic materials, a Weiss molecular field correction is added in the moments coupling energy. This leads to a Curie-Weiss form of the susceptibility above T_c:

$$\chi_{impurity} = \frac{C}{T - \Theta_w}. \tag{2.6}$$

The Weiss temperature Θ_W is a renormalization constant of the temperature indicating the type and size of the interaction of moments. The Weiss temperature is expressed as

$$\Theta_w = 2N_A S(S+1) z J_{eff}/3k_B, \tag{2.7}$$

Where z is the number of cations in the first coordination sphere (z=12 for the graphite structure). J_{eff} represents the magnetic interchange interaction in the system. For example, the negative value of Θ_w in FeSi indicates dominated screening interactions[1].

In the vicinity of the phase transition temperature T_c materials physical properties exhibit singular behavior that varies as a power law form of the temperature:

$$M(T) \propto M_0 \left(1 - \frac{T}{T_c}\right)^{\alpha}, \tag{2.8}$$

where M_0 is the saturation magnetization. The mean field approach gives $\alpha = \frac{1}{2}$.

In narrow band gap paramagnets which has magnetic impurities, i.e. $Fe_{1-y}Co_ySi$, the total susceptibility includes three terms:

$$\chi = \chi_{Pauli} + \chi_{impurity} + \chi_{activated}. \tag{2.9}$$

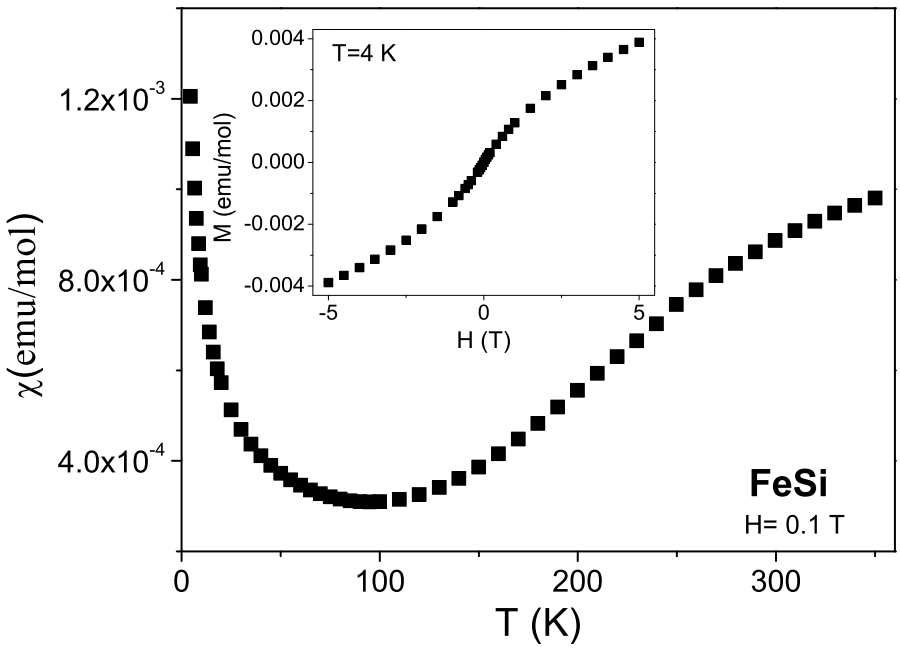

FIGURE 2.1: Susceptibility at $H = 0.01$ T and $T = 4$ K magnetization of a FeSi sample.

The first term is the Pauli paramagnetic susceptibility. This term is independent of temperature and represents the contribution of free carriers (the uncoupling moment of conduction electrons)[2]

$$\chi_{Pauli} = (\mu_B)^2 g(\varepsilon_F). \tag{2.10}$$

Here μ_B is the Bohr magneton, $g(\varepsilon_F)$ represents the density of states at the Fermi surface and ε_F is the Fermi energy. This term is observed in all kinds of materials. It could be quite large in materials with small gap and large number of the density of states at the Fermi level. When χ_{Pauli} is large enough to exceed a certain threshold, it is possible for the band to split spontaneously and form an itinerant ferromagnet. The second term is the contribution of the magnetic moments stemming from the impurity species which is modeled in a Curie Weiss form.

The third term is due to the activated moments at moderately high temperature under the narrow band gap feature, called the activated term:

$$\chi_{activated} = \exp \frac{-k_B T}{\Delta_g}. \tag{2.11}$$

Here the Δ_g corresponds to the band gap energy. This term arise when the activation of carriers above the band gap creating magnetic moments from the singlet states at low temperature.

Due to the combined effects of the contributions to the magnetization the susceptibility of FeSi has a unique shape (Fig. 2.1). Different contributions can be extracted from the different temperature ranges where the susceptibility was measured since each dominates in a different temperature regime. The Curie constant and the Weiss temperature can be obtained from the low temperature upturn, the intermediate temperature minimum represents the size of the Pauli-susceptibility, and the high temperature increase as a result of the activated carriers moments indicating the size of the energy gap or the vestige of the narrow energy gap.

2.1.2 Experimental Detail

The magnetic susceptibility and magnetization of all our samples were measured with a Quantum Design Magnetic Property Measurement System (MPMS) that is equipped with a 5 or 7 T superconducting magnet and that could access temperatures ranging from 1.8 to 400 K. In at least one case we were able to make use of an MPMS with a furnace extending the temperature range to 800 K. All measured samples have well determined phase purity and stoichiometry determined through X-ray diffraction (XRD) and wave-length disperse spectroscopy (WDS) characterization processes. Samples were prepared for magnetic measurements by

mounting at the center of a narrow quartz tube. The quartz tube was attached to the sample probe in a standard sample loading process in MPMS. The RSO mode of MPMS that was employed as it offers the best signal to noise performance in the range of magnetizations from 10^{-6} to 10^{-1} emu. Sample sizes were adjusted to have the signal sizes fit within the limit.

2.2 Transport Property: Models and Measurement

2.2.1 Resistivity Models

There are three models for the conductivity of materials that we consider in this work. These include a simple power law for describing Fermi liquid (FL) and non-FL metallic transport, variable range hopping transport for disordered insulators, and an activated form for the intrinsic conduction of insulating materials.

Power Law Model of Conductivity

The power law form for the conductivity,

$$\sigma = \sigma_0 + mT^{\alpha}, \tag{2.12}$$

is a simple way to describe both a FL and non-FL temperature dependence for conductors. FL theory predicts an $\alpha = 2$ for low disorder metallic transport. Disordered FL like the heavily doped semiconductors (Si:P) are best described by this form with $\alpha = 1/2$ which comes from the scaling theory described in chapter 1. Non-FL displays an anomalous temperature dependence of the conductivity typically displaying a power-law temperature dependence with α less than 2. In general, this model describes the temperature dependence of conductivity in metallic systems.

Variable Range Hopping Model of Conductivity

The variable range hopping model,

$$\sigma = \sigma_0 + \exp(T_\alpha/T)^\alpha \tag{2.13}$$

describes temperature dependence of conductivity in disordered insulators. The original work of Mott regarding the thermal activation of carriers so that they hop between localized states near the chemical potential predicts an $\alpha = 1/4$. Shklovskii and Efros contributed to this model by adding the Coulomb interaction[4;9], which yields an $\alpha = 1/2$. The model with the Coulomb interaction between localized moments is called the soft band gap variable range hopping model. The variable hopping models describe the temperature dependent transport behavior of the insulators or dilutely-doped semiconductors that they are still insulating (conductivity at zero temperature is zero).

Activated Form of the Conductivity of Insulators

Similar to the activated form of the magnetic susceptibility introduced earlier, the activated form describes the conductivity of carriers that are thermally excited across an energy gap. Here the conductivity is described as

$$\sigma \propto \exp(-\Delta_g/k_B T), \tag{2.14}$$

where Δ_g is the energy gap. This form describes the contribution in conductivity induced by the thermally activated charge carriers.

2.2.2 Hall Effect

In 1879, Edwin Hall observed an effect later named after him: a field depended voltage in current-carrying conductor that is perpendicular to the charge carrier

velocity and magnetic field[5]. During further studies of ferromagnetic metals[12], he discovered that there are two terms in the Hall effect (HE): a linearly field depended term called the "ordinary HE" and a second term know as the anomalous HE that is normally proportional to the magnetization.

The empirical relation of Hall resistivity in Gaussian units is represented as[12]:

$$\rho_{xy} = \rho^{OH} + \rho^{AH} = R_0 H + R_s 4\pi M, \tag{2.15}$$

where R_0 is the ordinary Hall coefficient dependent on the density and sign of the charge carriers. The anomalous Hall coefficient $R_s(T)$ is a scaling factor that relates the anomalous Hall resistivity to the magnetization. The ordinary HE is clarified as the consequence of charge carriers accumulating on the edge of the material due to the Lorentz force. This term is well described by the Drude model and often employed as an experimental tool in determining charge carrier density[2].

The mechanism of the anomalous HE is more complicated. After years of debate a coherent picture is emerging on the contributions and mechanisms of the anomalous Hall effect. It is generally agreed that two aspects contribute to the origin of the anomalous HE. The first one is the extrinsic scattering in collaboration of the spin-orbit coupling (SOC), including the skew-scattering scheme ($\sim \rho_{xx}$ term) and side-jump effect ($\sim \rho_{xx}^2$ term):

$$\rho_{xy}^{AH} = a\rho_{xx} + b\rho_{xx}^2. \tag{2.16}$$

The second aspect is the intrinsic contribution that arises from the SOC induced band structure modification. This contribution is independent of the carrier scattering rate - with the Hall resistivity related to the Hall conductivity by the form $\sigma_{xy} = \rho_{xy}/{\rho_{xx}}^2$ is independent of the impurity scatterings in materials[6].

2.2.3 Experimental Detail

The samples for transport measurements were prepared first as thin rectangular bars with low-power spark erosion cutting. The sample surfaces were polished with 0.3 μm emery paper to improve electrical contact at the surface. The sample for HE measurements were polished down to $\sim$0.1 mm. Pure platinum wire (.001 Platinum Pure TC Grade) and Epotek silver epoxy were used to make contacts for the four probe resistivity measurement. The transport measurements (including resistivity, magnetoresistance and Hall Effect measurements) were carried out over a 2 - 400 K temperature range employing standard low frequency lock-in techniques. The HE results were derived by symmetrizing the data in both positive and negative fields to correct the misalignment of the Hall leads. The transport measurements performed in the temperature range between 50 mK and 2 K employing transformer coupling lock-in amplifier techniques in an Oxford 200 dilution refrigerator with an Oxford 16 T superconducting magnet and a GPIB based data acquiring program written in Labview.

2.3 Thermodynamic Properties

2.3.1 Specific Heat Models

The specific heat C_v contains rich information of the intrinsic characteristics on the thermodynamic response of materials[7]. It quantifies the temperature response of a material in exchanging energy, which illustrates features of the excited states in the temperature range studied. The specific heat can assist in identifying the dominant excitations in solid systems as mechanisms can be identified via their temperature or field response. Lattice vibrations (phonon) in insulators at low temperature can be explained by the low temperature limit of the Debye model, which says that the specific heat of materials follows a T^3 rule under a temperature below θ_D, Debye

temperature. Debye model has the form of

$$C_{ph} = 1944\left[\frac{T}{\theta D}\right]^3 = \beta T^3. \tag{2.17}$$

This model works in a wide range in identifying phonon contributions in specific heat.

In metals, there is another major contribution to the specific heat due to the conducting charge carriers. With electron movements taken into consideration, the specific heat of metals at low temperature follows a $T-$linear dependence. The simple relation (equation) followed by

$$C = \gamma T + \beta T^3, \tag{2.18}$$

where γ is the Sommerfeld constant. The low temperatures means that the temperature is small comparing with Debye temperature in phonon modes or with Fermi temperature in considering electrons. This form is limited to temperatures being low compared to the Debye temperature which is below 20 K for most materials.

When investigating a magnetic metallic material, a third contribution to the specific heat due to magnetic excitations needs to be taken into account. The magnetic moments yields a $T^{-2}\exp -T_s/T$ contribution from the nuclear Schottky upturn. Thus, for a metal with magnetic contributions, the specific heat at low temperature (The region with thermal energy small comparing with internal field of the magnet) should be:

$$C = \gamma T + \delta T^{-2}\exp -T_s/T + \beta T^3. \tag{2.19}$$

At $T < 1K$ where the phonon movements are negligible, only the first two terms are important in explaining the specific heat properties of magnetic materials.

2.3.2 Thermo Relaxation Method and Experimental Detail

Despite of the various theoretical models used to understand the specific heat, experimentally obtaining specific heat data is usually difficult at the low temperatures. Large heat exchange rate and small noise to signal ratio problem becomes more and more substantial as the temperature decreases in low temperature experiments[11]. Moreover, specific heat measurement requires an adiabatic condition or at least a quasi-adiabatic condition being met for ease of analysis. As a result, reducing the heat transfer rate between measurement system and the environment is the key to design a successful calorimeter.

In the early days, the specific heat was measured according to the classic definition[10]:

$$C_p = \lim_{\mathrm{d}T \to 0} (\mathrm{d}Q/\mathrm{d}T)_p. \tag{2.20}$$

This method is called the adiabatic method, which requires a thermally isolated sample that is large enough to minimize the stray heat leaks affections. Because of the strict limitations of the method, i.e. large size, it is difficult to apply in material studies, especially in studying small samples at low temperatures.

In 1968, Sullivan and Seidel[11] proposed an *ac* method measuring the specific heat of small samples employing the commercial lock-in amplifiers. By generating an *ac* heat pulse of frequency $1/2\omega$, the ac temperature of the sample at frequency of ω is:

$$T_{ac} = \frac{\dot{Q}}{2\omega C}\left(1 + \frac{1}{\omega^2 {\tau_1}^2} + \omega^2 {\tau_2}^2 + const\right)^{1/2}. \tag{2.21}$$

Here τ_1 is the sample-bath relaxation time, and τ_2 is a combined exchange time of sample to heater (τ_h), sample to thermometer (τ_θ) and sample internal ($\tau_{internal}$)

time constants: ${\tau_2}^2 = {\tau_h}^2 + {\tau_\theta}^2 + {\tau_{internal}}^2$. It is obvious that to maintain a quasi-adiabatic condition, $\tau_1 \gg \tau_2$ is a necessary requirement. However, at very low temperature, due to the rapid increase of the thermal contact resistance, τ_2 could be considerably larger than the other thermal time constants. As a result, the frequency needs to be very low to meet a reasonable experimental condition, which makes an ac method undesirable.

Bachmann *et al* proposed another method for low temperature specific heat measurement of small samples[3], called the thermal relaxation method. It involves a 1-D heat-flow equation that describes the sample temperature as it is allowed to rise above the thermal bath with a constant heat pulse and then to decay to the bath temperature exponentially[8]. The sample temperature varies during the decay process in the form:

$$T_s(t) = T_0 + \Delta T \exp\left(-\frac{t}{\tau_1}\right). \tag{2.22}$$

Here T_s represents the sample temperature and T_0 refers to the bath temperature. ΔT is the initial temperature difference between bath and sample. τ_1 is the time constant of sample to bath heat exchange, also called the sample-bath relaxation time:

$$\tau_1 = C_p/K_b, \tag{2.23}$$

where C_p is the heat capacity of the sample and the K_b is the thermal conductivity of the thermal link from sample to the bath. With these relationships the heat capacity could be derived with measured τ_1 and K_b.

The specific heat measurements in our investigation were done employing the Quantum Design PPMS with ^{3}He dilution refrigerator inset in temperature range

of 300 mK - 20 K at 0 - 5 T magnetic field. We also developed a home-made specific heat data acquiring system with Labview programming on the Oxford He^3-He^4 dilution refrigerator to allow temperature reaching 50 mK. Both systems employed the thermal-relaxation method.

The experimental realization of the thermal-relaxation method relies on a weak permanent thermal link with a constant low temperature bath where the heater, thermometer and sample are combined as a core connecting to the bath with weak thermal links. The intermediate thermal resistance between the heater, the thermometer and the sample must be reduced to be as low as is possible in order to allow a fast heat exchange within the core. A slow exchange between the core and the bath is ensured with the weak thermal link that is in the form of thin, high resistance, conducting wires. Therefore, a quasi-adiabatic condition in the core is fulfilled for a possible calorimetric method, where the fast heat exchange within the core refers to a small time constant τ_2 and the slow thermal relaxation process governed by the weak link leads to a large time constant τ_1 ($\tau_1 \gg \tau_2$). Since τ_θ and τ_h could be reduced to minimum with a reasonable experimental design, one can achieve the best condition that all the τ_2 contributions are from $\tau_{internal}$.

The home-made specific heat measurement device was built following the quasi-adiabatic environment $\tau_1 \gg \tau_2$ requirement. The core of the system is an addenda being installed to the sample holder with only four high thermal resistance wire contact with the sample holder. The addenda is constructed by an evenly divided 1 kΩ RuO_2 resistor. This is created by carefully cutting the resistor so that there are two parallel 3.3 kΩ RuO_2 resistor on one sapphire base. One resistor serves as the heater connecting to the pulse generator circuit and the other is a resistance

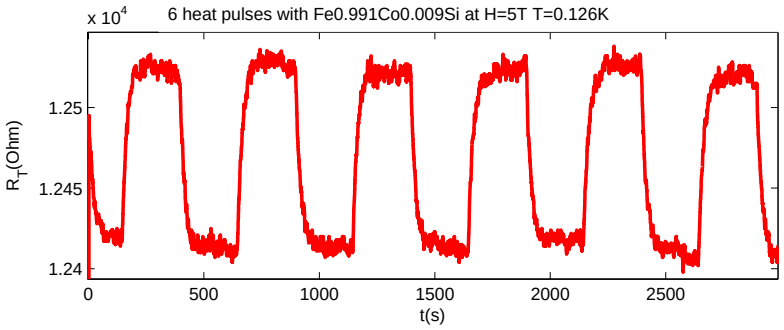

FIGURE 2.2: An example of heat pulses specific heat measurement.

thermometer which is measured via a small current and lock-in techniques. The thin resistive wires connected between the heater or the thermometer to the sample probe pillars serves as a current or voltage probe as well as a heat link to the bath. The sample holder and the entire dilution refrigerator environment act as the heat sink. Large τ_1 is achieved under this design. Small internal time constant τ_2 is guaranteed naturally since both the heater and thermometer are directly sitting on one piece of the sapphire base with good thermal conductivity. Thus, the $\tau_1 \gg \tau_2$ requirement is fulfilled.

The measurement procedure for the homemade specific heat measurement system is as following:

Computer sends command to a SRS DS345 synthesized function generator asking for an adequately long period square wave heat pulse of $\gtrsim 250s$ corresponding to the large τ_1; the heat pulse (V_p) reaches the heater after passing through a voltage divider consisting of a large resistance (11.8 MΩ); the voltage on the heater is recorded indirectly with a voltmeter (V_m); the entire addenda including the thermometer is heated and cooled according to the heat pulse cycle; the lock-in amplifier records the thermometer resistance (R_θ) during the entire heating - cooling cycle and the data is recorded via a computer. The heat pulse voltage is adjusted

according so that a heating level of 5% is maintained over the temperature range of 0.05 to 2 K. The current excitation for the thermometer is maintained to levels less than 5 nA. The heat pulse period was set properly to allow the addenda time to reach adequate thermal equilibrium. Therefore, at the two step edge of each square wave heating pulse, we can detect distinct heating and cooling processes as reported by the thermometer resistor through lock-in amplifier. An example of the resistance change on the thermometer in six heat pulses is shown in Fig. 2.2. The heating (or cooling) cycle of the thermometer resistance follows an exponential form:

$$R_\theta(t) = R_{\theta 0} - \Delta R \exp\left(-\frac{t}{\tau_1}\right). \tag{2.24}$$

By fitting the heating (or cooling) curve, we can directly get the time constant

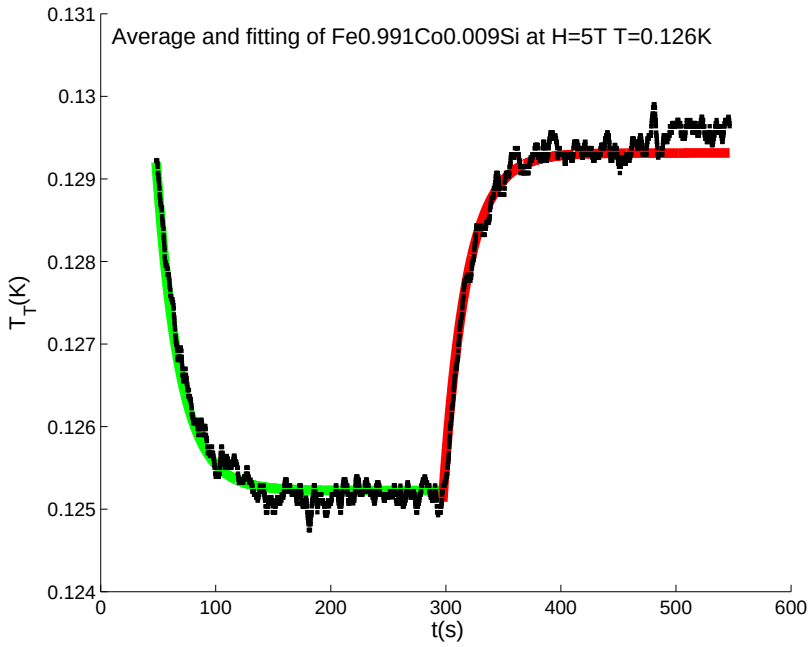

FIGURE 2.3: Averaged results of six pulses and the fits of the heating (cooling) process.

($\tau_1 \lesssim 30$ s), current temperature resistance $R_{\theta 0}$ and resistance change ΔR which

indicates the temperature change of the resistor with the amount of heat absorbed (or dissipated). The relation of the thermometer resistance to temperature is obtained with no current to the heater through careful measurement over the entire temperature range of the measurement and characterized via a fit of the data by a variable range hopping form:

$$R_\theta(T) = m_1 \exp\left[\left(\frac{m_2}{T}\right)^{\frac{1}{4}}\right]. \tag{2.25}$$

The two parameters m_1 and m_2 are carefully found from the best fit of the model to the data.

Fig. 2.3 displays the result of averaged six pulses and the fits with Eq. 2.24. The temperature difference between the heating and cooling cycles was extracted with the aid of equations 2.24 and 2.25. The heat transfer rate $\dot{Q}$ can be derived from the total input heat power based on the circuit resistor relationships. Thus, one finally have the specific heat:

$$C_p = \tau_1 \frac{\dot{Q}}{\Delta T}. \tag{2.26}$$

After calibration of the addenda specific heat, this home-made device can be used for measuring specific heat of small samples. The quality of the data was determined by the small background to signal ratio and a good thermal contact between sample and addenda fulfilling the $\tau_1 \gg \tau_2$ requirement. The base of the addenda was polished with sand paper so that the thickness of the sapphire was less than 0.2 mm (1.4 mg in mass) in order to reduce the addenda specific heat. Samples were attached to the addenda surface with very thin layers of Ge varnish that has a high thermal conductivity (5×10^{-3} W/cm at $T = 1$ K)[7] to minimize $\tau_{internal}$ and τ_2. The sample surface was polished with emery paper to increase the contact area and decrease the thermal resistance between sample and thermome-

ter. The experiment measured addenda specific heat was $\sim 10^{-8}$ J/K. Increase the size of the samples benefit the signal to noise ratio since the specific heat of the addenda being fixed. While the smallest sample around 2 mg have the background to signal ratio less than 20%, which is adequate for determining the specific heat of our samples.

2.4 Bibliography

[1] E. Arushanov, M. Respaud, J. M. Broto, J. Leotin, S. Askenazy, Ch. Kloc, E. Bucher, and K. Lisunov. Band parameters of FeSi single crystals determined by magnetic measurements. *Phys. Rev. B*, 55:8056–8059, 1997.

[2] N.W. Ashcroft and N.D. Mermin. *Solid State Physics*. Saunders College, Philadelphia, 1976.

[3] R. Bachmann, F. J. DiSalvo, T. H. Geballe, R. L. Greene, R. E. Howard, C. N. King, H. C. Kirsch, K. N. Lee, R. E. Schwall, H.U. Thomas, and R. B. Zubeck. Heat capacity measurements on small samples at low temperatures. *Review of Scientific Instruments*, 43(2):205–214, 1972.

[4] A L Efros and B I Shklovskii. Coulomb gap and low temperature conductivity of disordered systems. *Journal of Physics C: Solid State Physics*, 8(4):L49, 1975.

[5] E. H. Hall. On a new action of the magnet on electric currents. *American Journal of Mathematics*, 2(3):287–292, 1879.

[6] Naoto Nagaosa, Jairo Sinova, Shigeki Onoda, A. H. MacDonald, and N. P. Ong. Anomalous hall effect. *Reviews of Modern Physics*, 82(2):1539, 2010.

[7] Frank Pobell. *Matter and Methods at Low Temperatures*. Springer Berlin Heidelberg, Dresden, Germany, 2007.

[8] R. J. Schutz. Thermal relaxation calorimetry below 1 K. *Review of Scientific Instruments*, 45(4):548–551, 1974.

[9] Boris I. Shklovskii and Alex L. Efros. *Electronic Properties of Doped Semiconductors*. Springer Berlin Heidelberg, 1984.

[10] G. R. Stewart. Measurement of low temperature specific heat. *Review of Scientific Instruments*, 54(1):1–11, 1983.

[11] Sullivan, Paul F., and G. Seidel. Steady-state, ac-temperature calorimetry. *Physical Review*, 173(3):679–685, 1968.

[12] Changgan Zeng, Yugui Yao, Qian Niu, and Hanno H. Weitering. Linear magnetization dependence of the intrinsic anomalous hall effect. *Physical Review Letters*, 96(3):037204, 2006.

Chapter 3
Single Crystalline $Fe_{1-y}Co_ySi$ Magnetic Properties

As we have stated in chapter 1, Landau's Fermi-Liquid (FL) theory has been a very successful tool in understanding how the interactions between electrons affect the metallic state. Under the assumption of almost independent fermion quasiparticles, FL theory predicts material behaviors such as the T-linear dependence of specific heat and the T^2 dependence of conductivity at low temperature. The FL hypothesis is a satisfying description for most common metals, heavy fermion metal such as UPt_3[8]. It can be modified to describe heavily doped semiconductors as disordered FL[9]. Experimental research has found unusual temperature dependences in the low-temperature properties of many exceptional materials, such as high T_c cuprate superconductors and heavy-fermion systems on the verge of magnetic ordering[18]. In this chapter and the following chapter, we will concentrate on the Co doped small band gap insulator FeSi to compare with Mn doped FeSi, in which a field depended non-FL behavior is discovered near an insulator-metal-transition (IMT). A comprehensive study of the magnetic, transport and thermodynamic properties has been performed and the results will be discussed in the following two chapters.

3.1 Introduction

FeSi, a binary compound with a noncenterosymmetric B20 structure ($P2_13$) (Fig. 3.1), displays interesting anomalous magnetic and electrical properties. It is composed of half iron, however, contains no net magnetic moments. Activated magnetic moments appear quickly with the temperature rising. Because many of its properties are similar to a set of insulating cerium compounds[3,5], FeSi has been

described as a Kondo insulator[7]. CoSi and MnSi are isostructural with FeSi[10;15]. CoSi is diamagnetic(DM) semimetal, while MnSi is a well-known weak itinerant ferromagnet[13;16]. Doping FeSi with Mn or Co introduces magnetic moments with charge carriers as holes or electrons while the system maintains the B20 structure. The effect of the addition of charge carrier is significant that the system quickly go through an IMT with a few percentage of chemical substitution (Fig. 3.2). When doped with a small percentage of Mn, the system appears to be paramagnetic (PM) and insulating first, and stays PM and metallic at rather high doping concentrations. With Co doping, the system goes through a magnetic transition from PM to helimagnetic (HM) with chemical substitutions just beyond the IMT. $Fe_{1-y}Co_ySi$ stays HM until $y \approx 0.8$ where it transitions to a diamagnet.

Within this simple structural system, there are complicated interactions of spin-

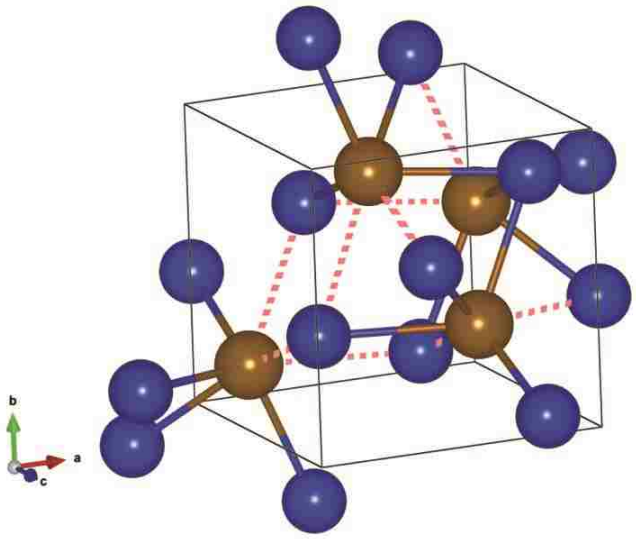

FIGURE 3.1: FeSi crystal structure in a unit cell. Brown balls represent Fe atoms and the blue ones are Si.

orbital coupling with the hole or electron types of disorder. One can tune the dopant level to manipulate the interactions and investigate across the magnetic transitions

and IMT. In addition, as silicon based semiconductors, they are also potential spintronic materials[10;12]. With both fundamental research significance and application potentials, pure and doped FeSi system has continuously attracted considerable research interest over the last few decades[10;15].

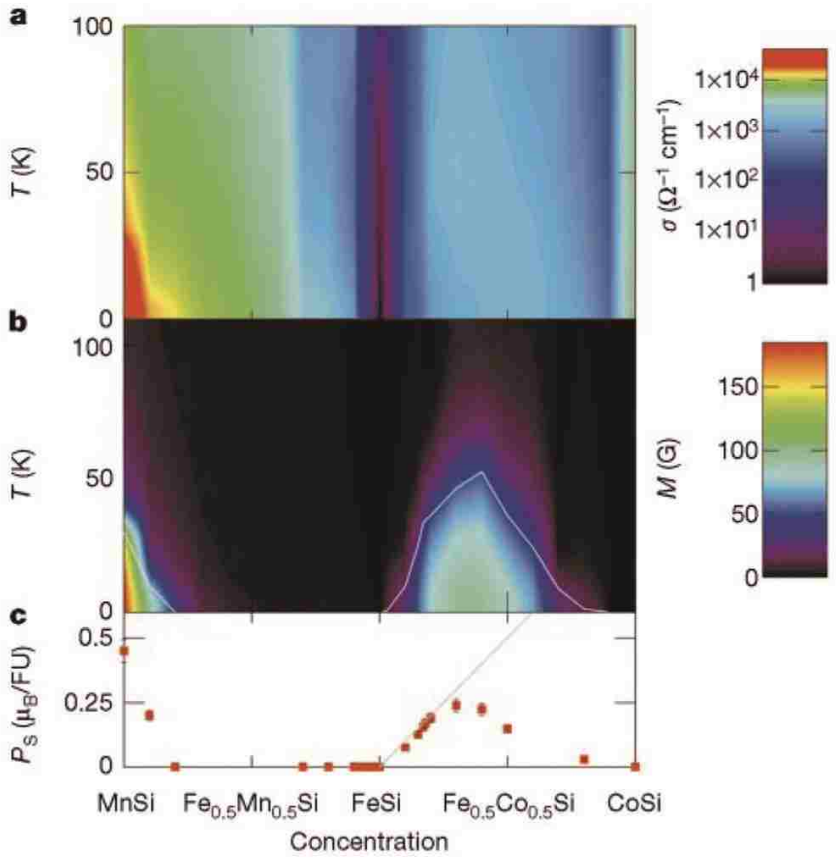

FIGURE 3.2: $Fe_{1-x,y}Mn_xCo_ySi$ magnetic and transport phase diagram[10]. **a**, Conductivity σ vs. temperature and concentration. **b**, Magnetization M at 1 T vs. temperature and concentration. **c**, Spontaneous magnetization (P_s) as determined from the saturated value of the magnetization at high magnetic field vs. concentration. Gray line represents behavior of Co per 1 μ_B moments.

Manyala *et al*[11] reported a field depended non-FL behavior in Mn doped FeSi near its IMT. Instead of the T^2 dependent conductivity in FL or $T^{1/2}$ dependence in disordered FL[9;17], at low temperature, $Fe_{1-x}Mn_xSi$ displays an anomalous tem-

perature dependence on conductivity ($\sigma \sim T^{\alpha}$, $0 \leq \alpha \leq 1$). Fig. 3.3 taken from ref.[11] depicts the color contour plot of conductivity dependence on the temperature and Mn substitution x (magnetic field H). The dark area with $x \approx 0.02$ corresponds to the very small α region, indicating where the system does not have a temperature and field dependence expected for a disordered Fermi liquid (Fig. 3.3). The field sensitive nature of the non-FL state is clearly shown in Fig. 3.3 **d**, as it takes less than a 1T field to return the temperature and field dependencies back to what is expected for a disordered Fermi liquid. Magnetotransport and magnetic data support that the non-FL behavior is related with uncoupled spins remaining at low temperature near the IMT. It was observed that the in-field entropy is larger than zero-field case indicated by data taken above 50 mK due to the entropy associated with relatively non-interacting magnetic moments existing below the lowest temperature in specific heat measurements. The extra entropy apparent upon applying a magnetic field verifies the existence of the under-screened spins. As a result, the non-FL behavior in $Fe_{1-x}Mn_xSi$ could be interpreted as being due to the under-screened or under-compensated Kondo effect[4;11] .

Co doping brings in electron type of charge carriers with the $S = 1/2$ moments. When comparing with the Mn doping, it brings in the question of whether or not Co doped FeSi yields a similar non-FL behavior as in $Fe_{1-x}Mn_xSi$. Co doping in FeSi induces electrons instead of holes in Mn doping case. There are different magnetic behaviors in different doping cases: electron doping beyond the IMT results in helimagnetic ordering while the hole doping produces a PM metal[12]. These differences may be reflected in the behavior close to the IMT. And detailed studies of the Co doping FeSi are required to explore the effects of the carrier type and the role of the interactions of the carriers with the local magnetic moments

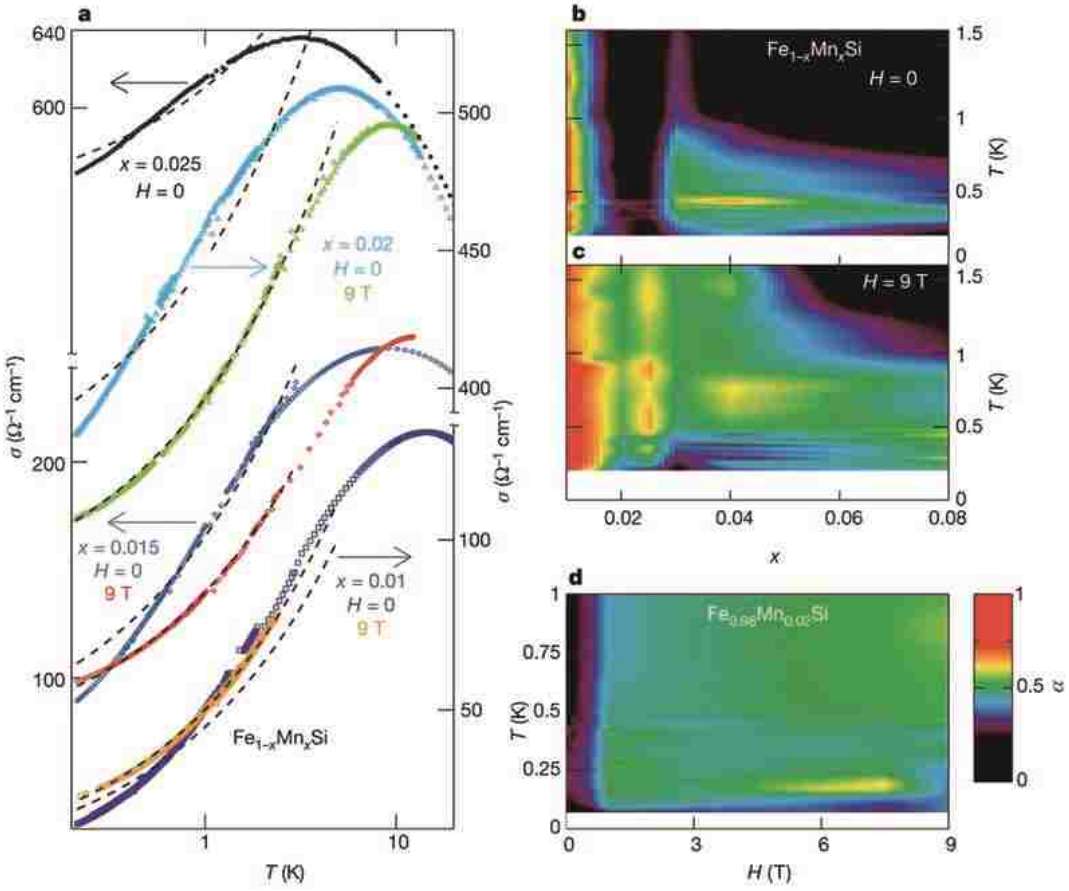

FIGURE 3.3: Conductivity (σ) vs. temperature (T) of $Fe_{1-x}Mn_xSi$ at magnetic fields (H) identified in the figure depicting Fermi-liquid to non-Fermi-liquid transition [11].
(a) Low temperature conductivity of zero field and $H = 9$ T data fitting with disordered FL behavior $T^{1/2}$. Lines represents fits of the behavior expected for a disordered Fermi liquid. (b) (c) Color contour plots of conductivity (σ) vs. temperature (T) and Mn concentration x parameterized by the logarithmic derivative of σ with respect to T: $\alpha = d\ln(\sigma - \sigma_0)/d\ln(T)$ at $H = 0$ T and $H = 9$ T. The parameter σ_0 is chosen by fitting the data below 0.7 K to a power law form $\sigma = \sigma_0 + m_\sigma T^\alpha$. (c) Color contour plots of conductivity (σ) vs. field (H) and T parameterized by α. The dark areas correspond to the very small α region, indicating where the system displays behavior distinct from that of a disordered Fermi liquid.

associated with the Co-dopants. DiTusa *et al*[6] discussed the IMT of Al doped FeSi, which is similar to the classic IMT in the semiconductor Si:P, a disordered FL albeit with a somewhat enhanced carrier mass. A comparison between those two cases of Fe_{1-y} Co_ySi and Si:P would also be meaningful in defining whether or not Co doping is a non-FL or just the conventional disordered FL. The contents that will be covered in this chapter are as following. First, I discussed the synthesis methodology in producing the single crystalline Fe_{1-y} Co_ySi, $0 \leq y \leq 0.1$. Then, the magnetic properties studied in temperature range 2 - 400 K and fields between 0 and 5T are discussed and compared with Mn doped FeSi.

3.2 Sample Synthesis and Preparation

When chemically substituting Co for Fe in FeSi, the system goes through IMT at a Co concentration of 0.01. Therefore, the investigation of dilute Co doped FeSi near its IMT requires high quality crystals whose stoichiometry are precisely determined. To achieve this goal, I first synthesized polycrystalline samples with the doping levels and growth process meticulously controlled. After verifying the crystal structure with X-ray diffraction (XRD), polycrystalline samples were either served as a starting charge for single crystals growth or as a check group on the systematic study of the doping induced properties in Co doped FeSi. The stoichiometry was checked with the Wavelength dispersive X-ray spectroscopy (WDS).

3.2.1 Polycrystalline Sample Synthesis

All polycrystalline samples were grown from high purity (99.999%) Fe (Co) powders and (99.999%) silicon pieces via the Arc melting method in a water-cooled Cu-crucible in an argon atmosphere. The high current electric arc is produced between a sharp tip anode and a large volume oxygen free copper crucible that serves as the negative electrode.(Fig 3.4). Power is supplied using a Miller Gold Star 400SS Direct Current Arc Welder Power Source.

FIGURE 3.4: Synthesis of polycrystalline $Fe_{1-x}Co_xSi$ samples in an arc furnace.

The arc melted Co doped FeSi samples are ellipsoidal pellets of mass between 1 and 3 grams. After arc melting, the pellets were sealed in quartz tubes in vacuum and annealed at a temperature of 1200°C (1000°C) for 1(4) days. Mass losses (mainly due to silicon vaporization) during melting and annealing process were carefully monitored to ensure the sample quality.

3.2.2 Single Crystalline Sample Synthesis

Single crystals of $Fe_{1-y}Co_ySi$ were prepared via the flux growth method and the vapor transport method. The choice of flux was antimony, which has a distinctly different atomic radius and a lower melting point than Co, Fe and Si. Pre-synthesized polycrystalline sample powders were mixed with antinomy chips at a desired ratio (1:5) in an alumina crucible. The crucible is covered with quartz wool on top and fitted into an evacuated quartz ampule. The whole assembly is placed upright into a box furnace and allowed to react at 1000°C for 4 days. It is cooled to 670 °C and spined in a centrifuge immediately after taken out of the furnace. Most of the antinomy liquid is filtered through the quartz wool, leaving single crystals of

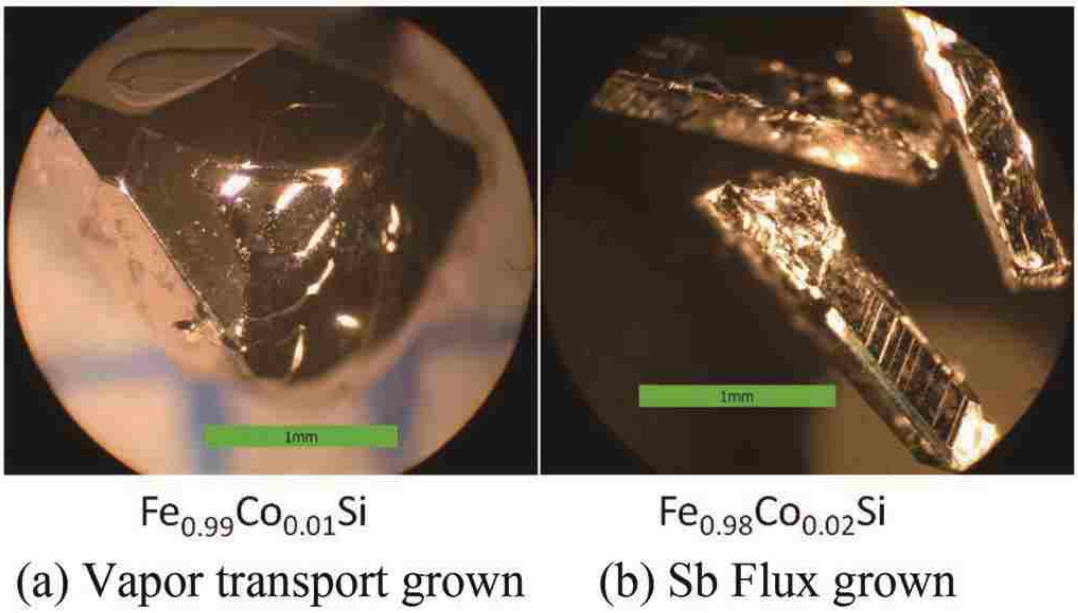

FIGURE 3.5: Pictures of single crystalline Co doped FeSi samples.

$Fe_{1-y}Co_ySi$ in the crucible. The Flux growth technique has been successful for all $Fe_{1-y}Co_ySi$ $0 \leq y \leq 0.1$. The chemical substitution levels in crystals are close to the nominal doping levels as verified with WDS (Table. 3.1). Single crystals obtained in this method are usually shiny small bars or needles with dimensions of several millimeters long and less than 1 mm thick (Fig 3.5. (b)). The flux growth technique has the advantage of high homogeneity and low impurity, but there is a possibility of the inclusion of flux elements, especially in very low doping level (less than 1%) samples. And our flux grown $y \sim 0.01$ samples display an abnormal R *vs* T behavior with a surprisingly large magnetoresistance.

In order to exclude the possibility of flux inclusions, we employed a standard Iodine vapor transport method (VTM) for growing the pure and very low doping samples. Low concentrations of Iodine and starting charge mixtures were placed in one end of an evacuated quartz ampule and a temperature gradient of 100 °C

TABLE 3.1: Stoichiometry analysis result with WDS of selected vapor transport grown $Fe_{1-y}Co_ySi$ samples (VTM) and flux grown samples (flux).

Synthesis Method	Nominal Co %	WDS Co %
	1.0	0.89(0.03)
	2.0	0.52(0.43)
	5.0	0.07(0.10)
VTM	6.0	0.34(0.23)
	1.0	1.03(0.03)
	2.0	1.74(0.12)
	2.5	2.35(0.06)
flux	3.0	2.81(0.08)
	5.0	4.46(0.06)
	8.0	8.50(0.17)
	10.0	9.09(0.16)

was applied via a tube furnace. The mixtures were allowed to react at 1000 °C for 10 - 14 days. Crystals obtained through this method are small lumps that could reach 10 mg and roughly 2 mm×4 mm in size, see Fig 3.5.

The VTM synthesized crystals usually have doping concentrations that are much lower comparing with the nominal Co levels. As a result, synthesizing high level doping samples with VTM becomes troublesome. This method served as a supplement for the flux growth method to obtain pure and the very low doping concentration (up to 1.2%) single crystals (Table. 3.1).

3.2.3 Characterization

To ensure the quality of the crystals, all the samples were examined with X-ray diffraction on a Nonius Kappa CCD diffractometer (Mo $K_\alpha, \lambda = 0.71073\mathring{A}$). No indications of secondary phases were found in the single crystalline samples. The single crystal XRD refinement result confirmed that the $Fe_{1-y}Co_ySi$ crystals are in a B20 structure which lacks a center of inversion symmetry (space group $P2_13$).

Lattice constants of the $Fe_{1-y}Co_ySi$ follow an increasing trend with increasing y in agreement with Vegards law and previous work[12].

Due to the requirements for high precision in crystal stoichiometry for our FeCoSi samples, the WDS technique was employed to quantitatively identify the ratio of Fe, Co and Si within our samples. The results of the WDS investigations are presented in Table. 3.1. The WDS technique uses the characteristic X-rays generated from a sample to identify the elemental constituents[14]. Different from the more commonly applied Electron dispersive X-ray spectroscopy (EDS), it acquires one wavelength at a time and collects the spectrum profile of the full wavelength range, which is more time consuming but gives an apparently improvement resolution compared to EDS.

In order to separate the spectrum by wavelength, the characteristic X-rays are diffracted with a analyzing crystal of specific lattice space. The diffraction angle follows the Bragg's law: $n\lambda = 2dsin\theta$. Here λ is the wavelength of the characteristic X-ray, d is the lattice spacing of the analyzing crystal; and θ is the angle between the X-ray and the crystal diffraction surface. The interference between other elements in WDS are greatly reduced after diffraction. As a result, it is effective quantifying the level of trace elements in a sample. As in the analysis of $Fe_{1-y}Co_ySi$, one can have resolution of 10^{-3} in atomic ratio as shown in table. 3.1.

3.3 Susceptibility and Magnetization of $Fe_{1-y}Co_ySi$

The susceptibility χ versus temperature T plots of the single crystalline $Fe_{1-y}Co_ySi$, $0 \leq y \leq 0.1$ taken at 1000 Oe field are shown in Fig. 3.6. The most obvious feature of the plot is the systematic increase of susceptibility at low temperature

with y. The $y = 0.045$ and the $y = 0.091$ samples show signs of ordering above 1.8 K. For $y < 0.03$ Co doping, no peak associated with magnetic ordering was observed in the $T > 1.8$ K region. This is supported with an Arrot-plot analysis[1] and the details of the ordering temperature consistent with the Arrott-plot will be presented later in this chapter.

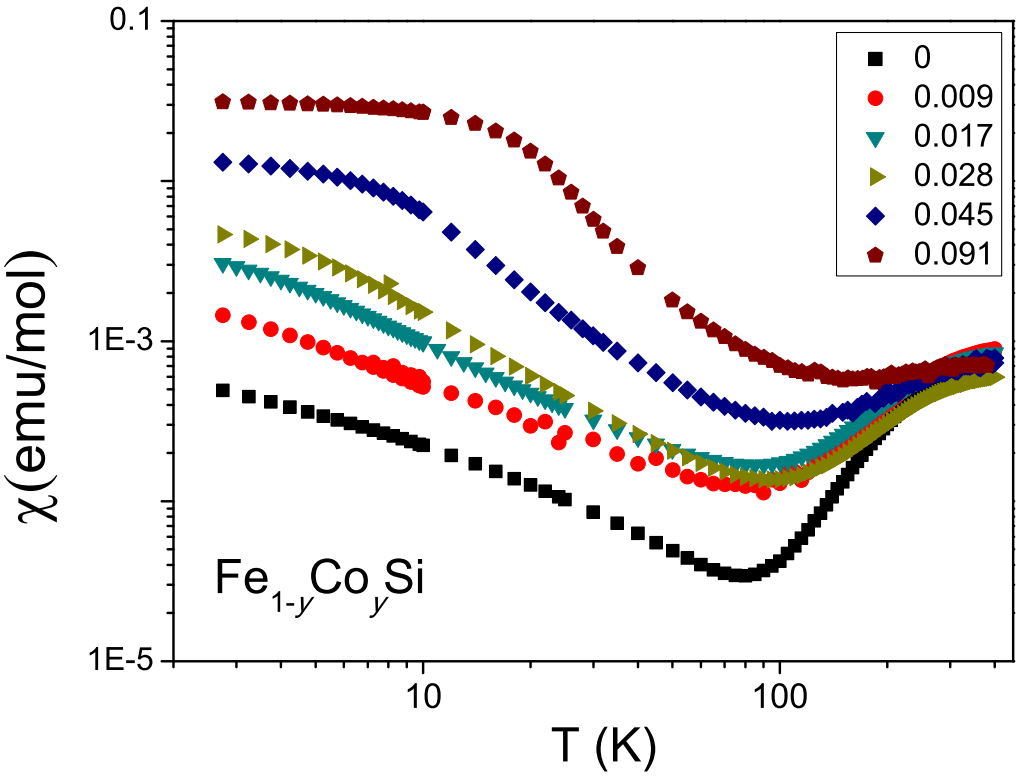

FIGURE 3.6: Susceptibility of $Fe_{1-y}Co_ySi$ single crystalline samples $0 \leq y \leq 0.1$ at $H = 1000$ Oe magnetic field.

The susceptibility curves were fit with Eq. 2.9, where the Curie-Weiss term corresponds to the low temperature upturn of susceptibility above ordering temperature (T_c). The impurity moment contribution can be extracted from the parameters determined from the best fit to the data with Eq. 2.6. The Curie constants and Weiss temperatures derived from the fits are presented in Fig. 3.7. The Weiss temper-

atures and Curie constants from a previous study of Mn-doped FeSi[11] are also included for comparison(Fig. 3.7 red bullets).

As shown in Fig. 3.7 (a), the Weiss temperature Θ_w of $Fe_{1-x,y}$ Mn_x Co_ySi is systematically increases with both x and y. Mn doping yields a negative Θ_w indicating a tendency for singlet formation as a result of dominated screening effect. While for Co doping, Θ_w are positive except in the very low doping regime $y > 0.01$, indicating an ordering effect dominated interaction. In the Curie constant plot (Fig. 3.7 (b)), low Mn doping induces $S = 1$ impurity moments. With larger x the magnetic moments tend to decrease, which reduced into $S = 1/2$ at the doping level $y \approx 0.08$. For Co doping, an $S = 1$ impurity moment similar to what was observed for Mn doping. However, at larger y the magnetic moment gradually grows to $S = 3/2$ at $y \approx 0.05$ where the system tends to order magnetically at low temperature.

With the evolution of the magnetic moments induced with chemical substitution characterized above, one can compare the impurity concentration to the Curie Constant. The result is plotted in Fig. 3.8. density of magnetic moments determined from the Curie-Weiss fits to the magnetic susceptibility agrees well with the density of Co atoms determined from our WDS data. In addition, we have characterized our nominally pure FeSi sample in the same way leading to the conclusion that this sample contains as much as 0.5% of $S = 1$ impurities perhaps as a result of defects or Si deficiencies in this sample. This level of impurity is consistent in crystals grown in either VTM or flux method.

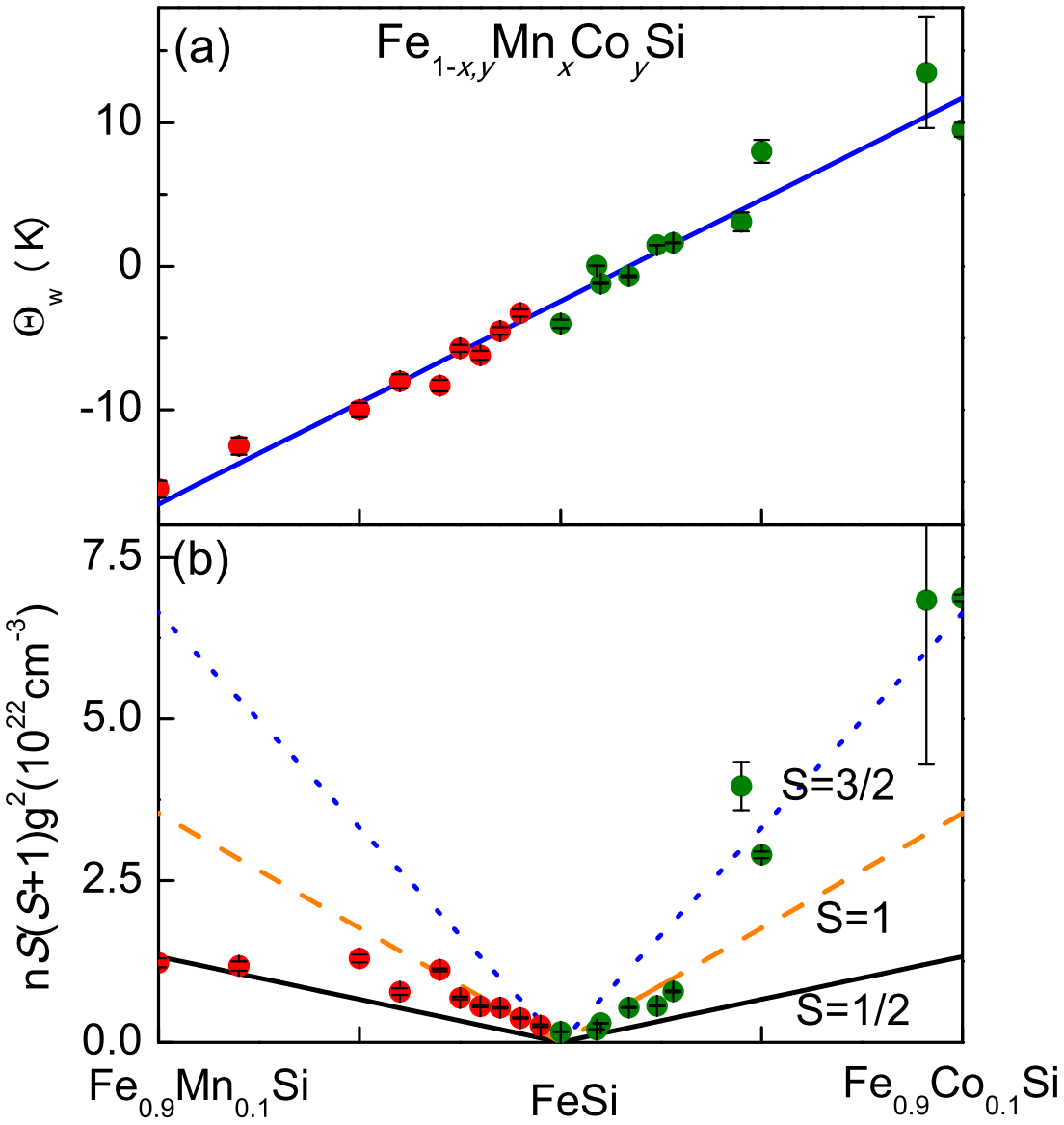

FIGURE 3.7: Curie-Weiss parameters of $Fe_{1-x,y}Mn_xCo_ySi$ from fits of the Curie-Weiss form to the susceptibility data.
(a) Weiss temperature of $Fe_{1-x,y}Mn_xCo_ySi$ displaying a systematic increase with x and y. Solid line is a linear fit to the data. (b) Cuire constant of $Fe_{1-x,y}Mn_xCo_ySi$ changing as a function of x and y. The three lines are $nS(S+1)g^2$ with $S = 1/2$, $S = 1$ and $S = 3/2$ using the dopant densities of Mn(Co).

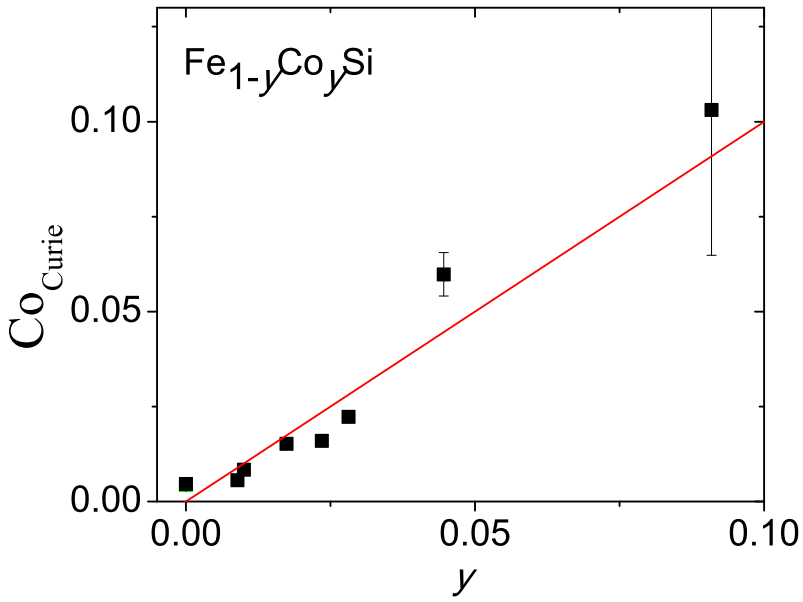

FIGURE 3.8: The concentration of magnetic moments of Fe_{1-y} $Co_y Si$, $0 \leq y \leq 0.1$ obtained from Curie constant with $J = 1$ at $y \leq 0.03$ and $J = 3/2$ at $y > 0.04$.

The magnetization ($M(H)$) plots of the $Fe_{0.991}Co_{0.009}Si$, $Fe_{0.972}Co_{0.028}$ and $Fe_{0.909}Co_{0.091}$ samples are shown at Fig. 3.9, 3.10 and 3.11. The almost linear behavior in magnetization of $Fe_{0.991}Co_{0.009}Si$ in the entire temperature range explored indicates that there is no ordered moments contributions. This is consistent with our determination of a negative Θ_w for this sample. By $y = 0.028$ the magnetization curves appear to be close to a magnetic ordering. $Fe_{0.909}Co_{0.091}Si$ is likely to be helimagnetic as we find that it orders at $T \approx 20$ K. For all samples, a PM $M(H)$ curve is apparent at $T > 20$ K.

Magnetizations at $T = 4$ K of selected $Fe_{1-y}Co_y Si$, $0 \leq y \leq 0.1$ sample are plotted in Fig. 3.12. In general, the magnetization increases consistent with value of y and the Curie constant determined from the temperature dependence of the magnetic susceptibility. Evidence of ordering is observed in the magnetization with $y \approx 0.03$.

The value of the high field magnetization appears to scale well with y, particularly for the magnetic ordered samples. The saturated moment or the ordered moment in the $y \geq 0.45$ samples are in a small size of $0.5 \sim 0.6\ \mu_B$ at $T = 4$ K. Comparing with the Curie-Weiss moment in a magnitude of $\frac{3}{2}\ \mu_B$, the saturate moment size is apparently smaller. The strong Curie Weiss dependence and small weak ordered moments indicate a weak magnetism[2] system.

In order to determine precisely the thermodynamic Curie temperature, the Arrott analysis[1;19] is employed following Eq. 6.16 in the discussion of Appendix A. The Arrott plots H/M vs. M^2 of three ordered or near-ordered samples are shown in Fig. 3.13, 3.14 and 3.15. The $y = 0.091$ sample is fully ordered which has almost linear H/M vs. M^2 behavior in large field range. $Fe_{0.955}Co_{0.045}Si$ displays a ferromagnetic feature above $\sim$1 T field. The $y = 0.028$ sample can barely fit to a linear fit above $H \approx 2$ T suggesting a paramagnet. We derived the intercept M_s from a linear fit of the ferromagnetically ordered part of the H/M vs. M^2 curve (Fig. 3.16). The Curie temperatures are where the intercepts become zero. The T_c of the $Fe_{0.909}Co_{0.091}Si$ is $T = 21.98$ K and $Fe_{0.955}Co_{0.045}Si$ orders in over 1 T field at $T = 8.15$ K.

3.4 Conclusion

We have investigated the magnetic properties of single crystalline $Fe_{1-y}Co_ySi$, $0 \leq y \leq 0.1$. Surprisingly, an $S = 1$ impurity moment in $Fe_{1-y}Co_ySi$ with small y is similar to what was observed for Mn substitutions. For higher Co substitutions, we observed an $S = \frac{3}{2}$ moment differing from the $S = \frac{1}{2}$ state found for Mn doped samples with $x > 0.05$. A systematic dependence of the Weiss temperature through the entire range of x and y is observed. From Mn to Co side of the $Fe_{1-x,y}Mn_xCo_ySi$, the Weiss temperature is increased from negative to positive

value. The very low doping ones with $y \sim 0.01$ still has a negative Θ_w, indicating a similar screening effect dominated environment on the $S = 1$ local moments as in the low doping concentration $Fe_{1-x}Mn_xSi$. In the narrow region of $y < 0.03$, our crystal show no indication of magnetic ordering, likely a fruitful place to search for NFL behavior.

3.5 Bibliography

[1] Anthony Arrott and John E. Noakes. Approximate equation of state for nickel near its critical temperature. *Physical Review Letters*, 19(14):786–789, 1967.

[2] A. Bauer, A. Neubauer, C. Franz, uuml, W. nzer, M. Garst, and C. Pfleiderer. Quantum phase transitions in single-crystal $Mn_{1-x}Fe_xSi$ and $Mn_{1-x}Co_xSi$: Crystal growth, magnetization, ac susceptibility, and specific heat. *Physical Review B*, 82(6):064404, 2010.

[3] B. Bucher, Z. Schlesinger, D. Mandrus, Z. Fisk, J. Sarrao, J. F. DiTusa, C. Oglesby, G. Aeppli, and E. Bucher. Charge dynamics of Ce-based compounds: Connection between the mixed valent and Kondo-insulator states. *Physical Review B*, 53(6):R2948–R2951, 1996.

[4] P. Coleman and C. Pépin. Singular Fermi - liquid behavior in the underscreened Kondo model. *Phys. Rev. B*, 68:220405, 2003.

[5] J. C. Cooley, M. C. Aronson, and P. C. Canfield. High pressures and the Kondo gap in $Ce_3Bi_4Pt_3$. *Physical Review B*, 55(12):7533–7538, 1997.

[6] J. F. DiTusa, K. Friemelt, E. Bucher, G. Aeppli, and A. P. Ramirez. Metal-insulator transitions in the Kondo insulator FeSi and classic semiconductors are similar. *Physical Review Letters*, 78(14):2831–2834, 1997.

[7] Z. Fisk, J. L. Sarrao, J. D. Thompson, D. Mandrus, M. F. Hundley, A. Miglori, B. Bucher, Z. Schlesinger, G. Aeppli, E. Bucher, J. F. DiTusa, C. S. Oglesby, H. R. Ott, P. C. Canfield, and S. E. Brown. Kondo insulators. *Physica B: Condensed Matter*, 206207:798–803, 1995.

[8] P. H. Frings, J. J. M. Franse, F. R. de Boer, and A. Menovsky. Magnetic properties of U_xPt_y compounds. *Journal of Magnetism and Magnetic Materials*, 3134, Part 1(0):240–242, 1983.

[9] Patrick A. Lee and T. V. Ramakrishnan. Disordered electronic systems. *Reviews of Modern Physics*, 57(2):287–337, 1985.

[10] N. Manyala, Y. Sidis, J. F. DiTusa, G. Aeppli, D. P. Young, and Z. Fisk. Magnetoresistance from quantum interference effects in ferromagnets. *Nature*, 404(6778):581–584, 2000.

[11] N. Manyala, J. F. DiTusa, G. Aeppli, and A. P. Ramirez. Doping a semiconductor to create an unconventional metal. *Nature*, 454(7207):976–980, 2008.

[12] Ncholu Manyala, Yvan Sidis, John F. DiTusa, Gabriel Aeppli, David P. Young, and Zachary Fisk. Large anomalous Hall effect in a silicon-based magnetic semiconductor. *Nat Mater*, 3(4):255–262, 2004.

[13] T. Moriya. *Spin fluctuations in itinerant electron magnetism*. Springer, 1983.

[14] Oxford Instruments NanoAnalysis. An introduction to energy-dispersive and wavelength-dispersive X-ray microanalysis, June 2013.

[15] Alla E. Petrova, Vladimir N. Krasnorussky, Anatoly A. Shikov, William M. Yuhasz, Thomas A. Lograsso, Jason C. Lashley, and Sergei M. Stishov. Elastic, thermodynamic, and electronic properties of MnSi, FeSi, and CoSi. *Physical Review B*, 82(15):155124, 2010.

[16] C. Pfleiderer, D. Reznik, L. Pintschovius, H. v Lohneysen, M. Garst, and A. Rosch. Partial order in the non-Fermi-liquid phase of MnSi. *Nature*, 427 (6971):227–231, 2004.

[17] T. F. Rosenbaum, R. F. Milligan, M. A. Paalanen, G. A. Thomas, R. N. Bhatt, and W. Lin. Metal-insulator transition in a doped semiconductor. *Physical Review B*, 27(12):7509–7523, 1983.

[18] G. R. Stewart. Non-Fermi-liquid behavior in d- and f-electron metals. *Reviews of Modern Physics*, 73(4):797–855, 2001.

[19] I. Yeung, R. M. Roshko, and G. Williams. Arrott-plot criterion for ferromagnetism in disordered systems. *Phys. Rev. B*, 34:3456–3457, 1986.

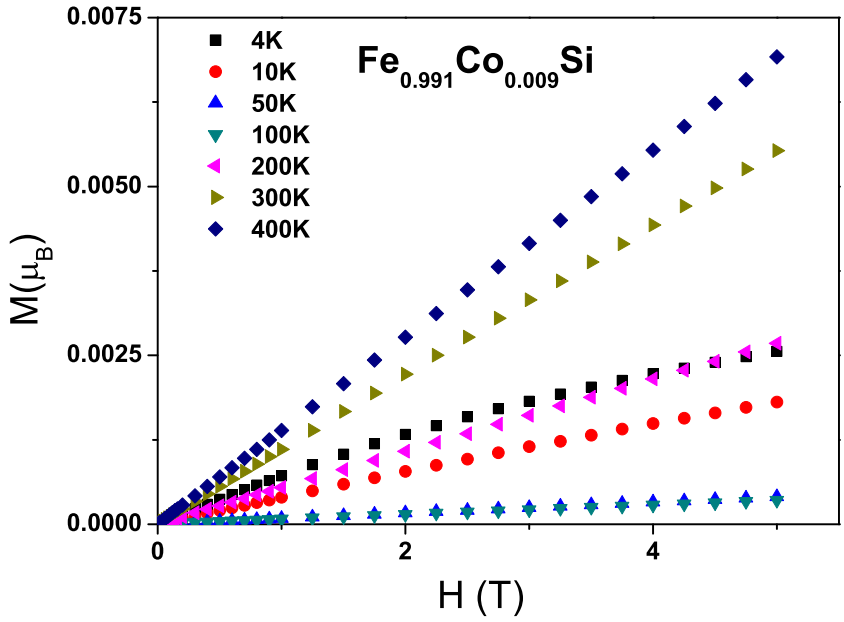

FIGURE 3.9: Magnetization of $Fe_{0.991}Co_{0.009}Si$ in the unit of Bohr magneton (μ_B) from 0 to 5 T magnetic field at 4 - 400 K temperatures.

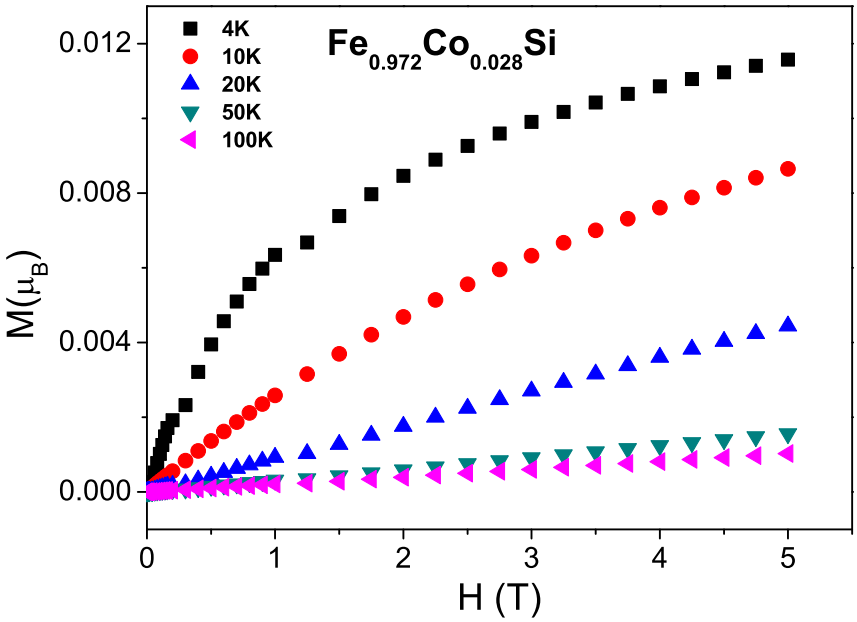

FIGURE 3.10: Magnetization of $Fe_{0.971}Co_{0.029}Si$ in 0 - 5 T magnetic field at 4 -100 K temperatures.

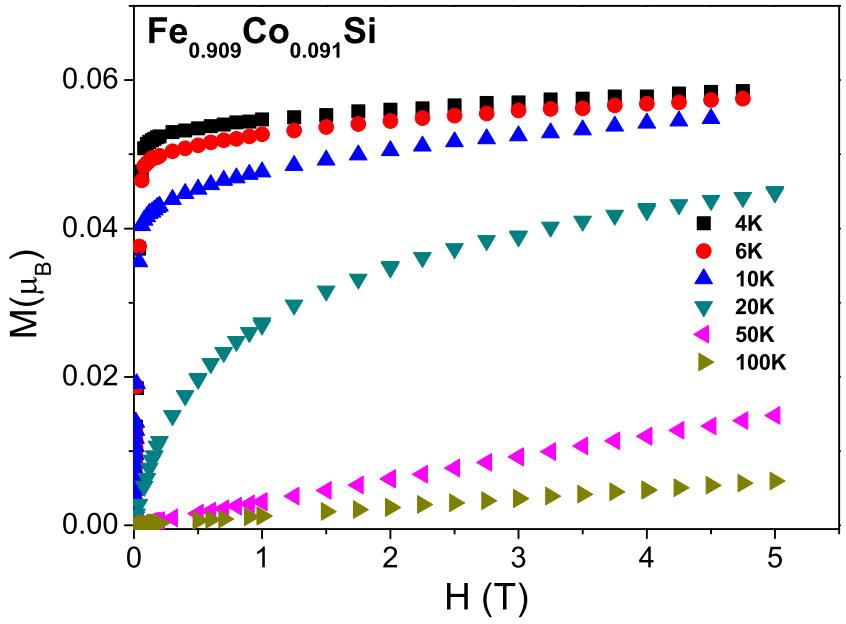

FIGURE 3.11: Magnetizations of $Fe_{0.909}Co_{0.091}Si$ in 0 - 5 T magnetic field at 4 -100 K temperatures.

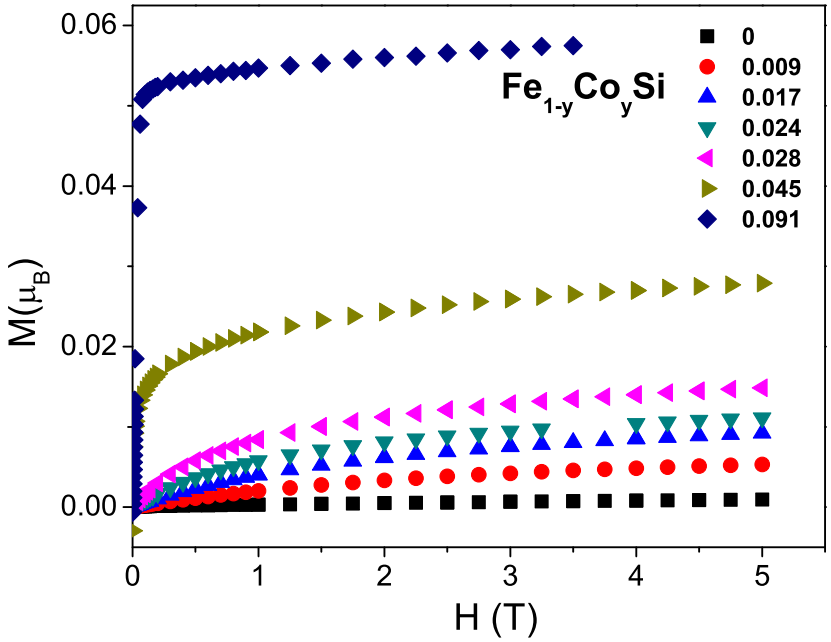

FIGURE 3.12: Magnetization of $Fe_{1-y}Co_ySi$, $0 \leq y \leq 0.1$ in 0 - 5 T at $T = 4$ K.

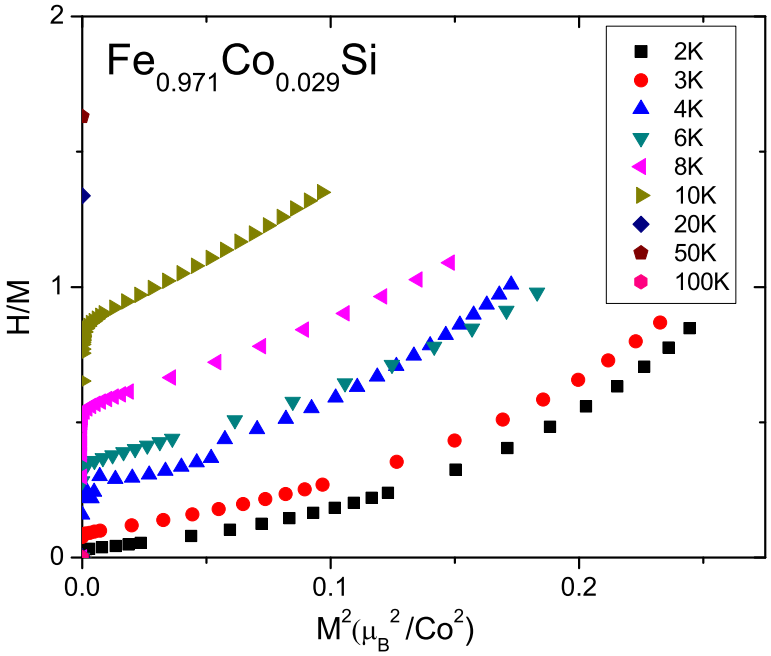

FIGURE 3.13: Arrott plot of $Fe_{0.971}Co_{0.029}Si$.

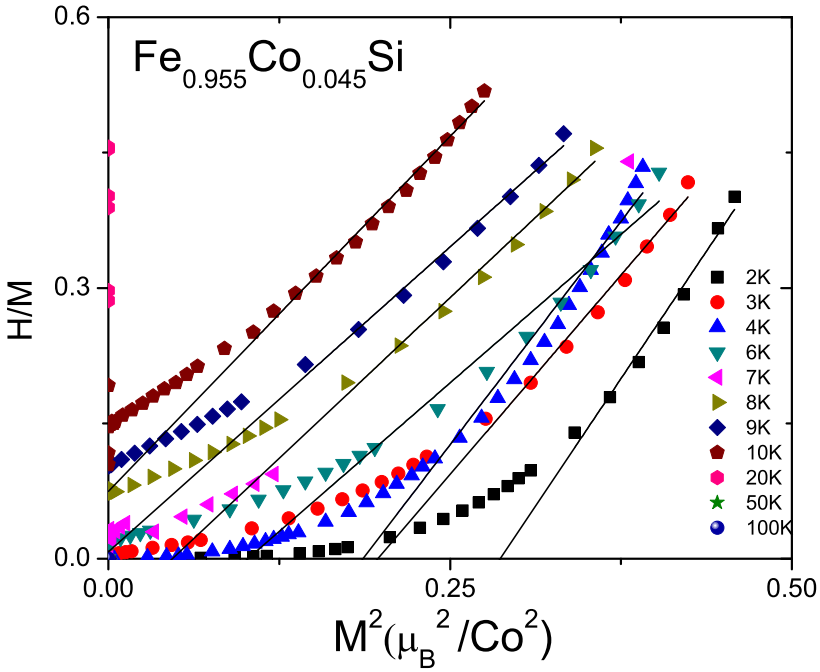

FIGURE 3.14: Arrott plot of $Fe_{0.955}Co_{0.045}Si$.

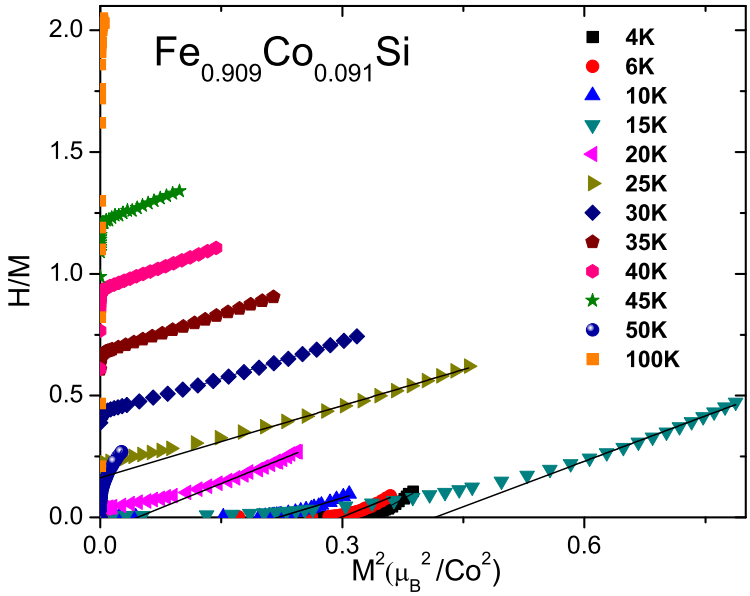

FIGURE 3.15: Arrott plot of $Fe_{0.909}Co_{0.091}Si$.

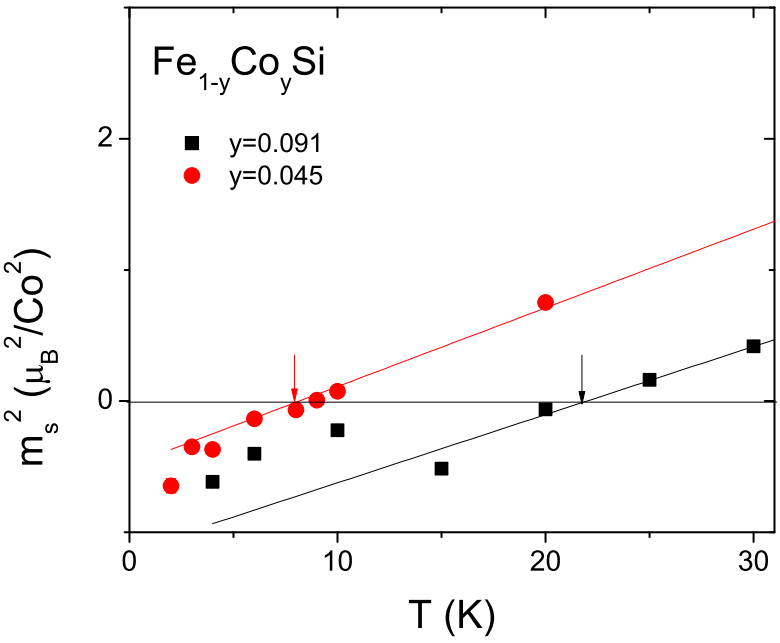

FIGURE 3.16: M_s derived from the Arrott plot intercept of $Fe_{0.909}Co_{0.091}Si$ and $Fe_{0.955}Co_{0.045}Si$ determining Curie temperature.

Chapter 4

Single Crystalline $Fe_{1-y}Co_ySi$ Transport and Thermodynamic Properties

In this chapter, we continue with the discussion of the investigation of single crystalline $Fe_{1-y}Co_ySi$ transport and thermodynamic properties. These measurements will directly demonstrate the non Fermi-Liquid (FL) behavior near the insulator-metal-transition (IMT). We have investigated the transport and thermodynamic properties of $Fe_{1-y}Co_ySi$, $0 \leq y \leq 0.1$ paying particularly attention to the region of dilute doping ($0 \leq y \leq 0.03$).

4.1 $Fe_{1-y}Co_ySi$ Transport Properties

4.1.1 Resistivity and Magnetoresistivity of $Fe_{1-y}Co_ySi$

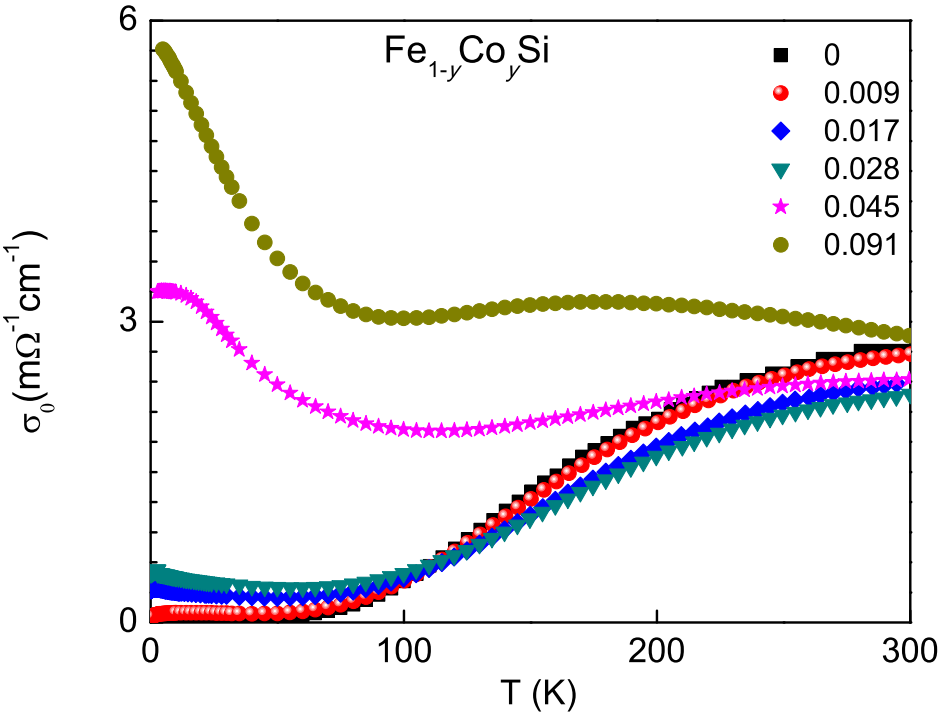

FIGURE 4.1: Conductivity of $Fe_{1-y}Co_ySi$, $0 \leq y \leq 0.1$.

The temperature dependence of zero field conductivity of $Fe_{1-y}Co_ySi$ for $0 \leq y \leq 0.1$ is shown in Fig. 4.1. The low temperature conductivity increases systematically with y. While pure FeSi is an insulator, the doped samples are more metallic as the analytic continuation of their measured conductivities to zero temperature is non-zero. The higher doping level samples, $y = 0.091$ and $y = 0.045$, display increasing conductivity with decreasing temperature, which is a clear metallic behavior. The product of the Fermi wave vector, k_f, and the mean free path, l, is often used as an benchmark for metallic behavior ($k_f l > 1$). The $k_f l$ can be obtained from carrier density and resistivity with free electron models[6]. We plotted the $k_f l$ of the Fe_{1-y} Co_ySi, $0 \leq y \leq 0.1$ crystals in Fig. 4.2 to demonstrate the crossover from insulating to metallic behavior. While the two higher doped samples are clearly on the metallic side, the samples with $0.01 \leq y \leq 0.03$ have $k_f l$ around $\frac{1}{2}$, indicating that the carriers are likely to be weakly localized at $T = 4$ K. The $k_f l$ of the nominally pure FeSi sample is near zero with no intentional dopants.

Energy gap at high temperature can be obtained for low doping samples from activated behaviors. We have extrapolated the energy gap in the 100 - 300 K region by fitting the activated form $\sigma \propto \exp -\Delta_g/2T$ to our data of $y \leq 0.03$ samples. Those data are compared with activation gap energy Δ_g obtained from fitting the susceptibility data in Fig. 3.6. The two sets of data ($0 \leq y \leq 0.03$) agree well with each other (Fig. 4.3) with a trend of gap decreasing with y indicating that the high temperature activated magnetic moments and charge carriers are well correlated.

The temperature dependent conductivities of the $y = 0.009$, 0.017 and 0.028 samples below 10 K in $H = 0$ or 9 T (8 T) magnetic fields are plotted in Fig. 4.4. The solid lines are fits of the disordered FL behavior $\sigma \propto T^{1/2}$ to the data. From

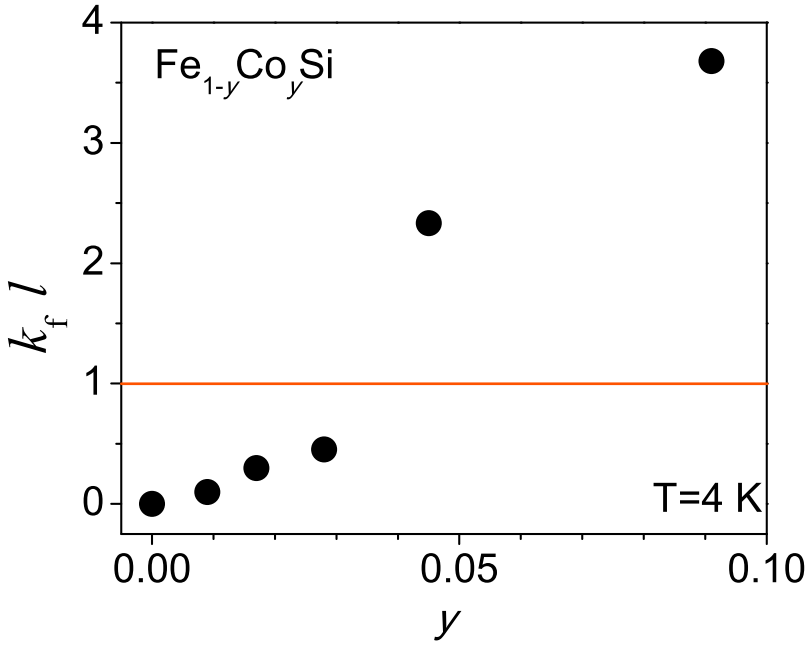

FIGURE 4.2: $k_f l$ of $Fe_{1-y}Co_ySi$, $0 \leq y \leq 0.1$.

the zero field data, it is clear the disordered FL theory doesn't describe the y=0.009 sample conductivity well. This sample appears to be very close to the IMT as the extrapolated conductivity is zero for all reasonable forms of the temperature dependence. We also fit the Variable Range Hopping model and the soft gap Variable Range Hopping model to the zero field conductivity of the $y = 0.009$ sample. Neither of them return reasonable fits indicating that the $y = 0.009$ sample cannot be described by the standard insulating models of the temperature dependent conductivity as well. With the application of a magnetic field of $H = 8$ T the conductivity of the y=0.009 sample increases and the temperature dependence resembles that of a disordered FL (α =0.5) much more closely. We have fit a power-law form for the temperature dependent conductivity to the zero field data allowing the power-law, α, to float. The best fit value was found to be close to 0.79. Thus, we can conclude that a field dependent non-FL behavior was found in the low doping level of $Fe_{1-y}Co_ySi$ with σ displaying an anomalous $T-$dependence. The zero field

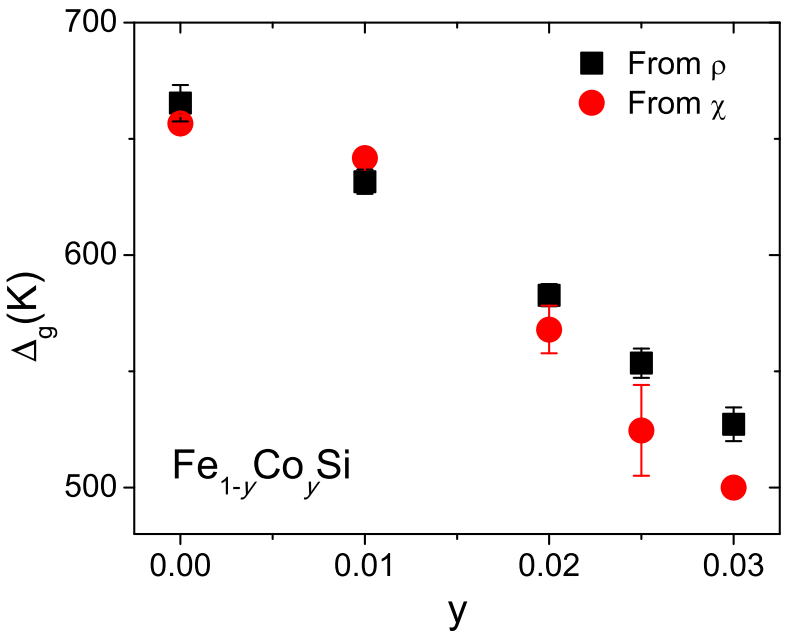

FIGURE 4.3: Energy gap of $Fe_{1-y}Co_ySi$, $0 \leq y \leq 0.03$ derived from activated function of susceptibility and conductivity.

conductivity of slightly larger y samples agree somewhat better with a $T^{1/2}$ dependence. Similar to Mn substituted FeSi, the non-FL behavior in $Fe_{1-y}Co_ySi$, where y is close to the critical region of IMT, can be tuned away with a large density of substitutions. The conductivity $Fe_{0.983}Co_{0.017}Si$ and $Fe_{0.972}Co_{0.028}Si$ in field do not appear to be described well by disordered FL theory as power-law fits to the data indicate α close to 1.

The temperature dependence of conductivity in magnetic fields can be viewed in fig. 4.5. The zero field conductivity, σ_0, also can be obtained from the fit. In zero field σ_0 is nearly zero while adding field increase conductivity with $\sigma_0 \approx 22$ $(\Omega cm)^{-1}$ at $H = 8$ T. This indicates an field induced IMT - similar to what was found in Mn doped FeSi. Meanwhile, the agreement of $T^{1/2}$ law to the in high field data indicates that the system is pushed toward a disordered FL with application

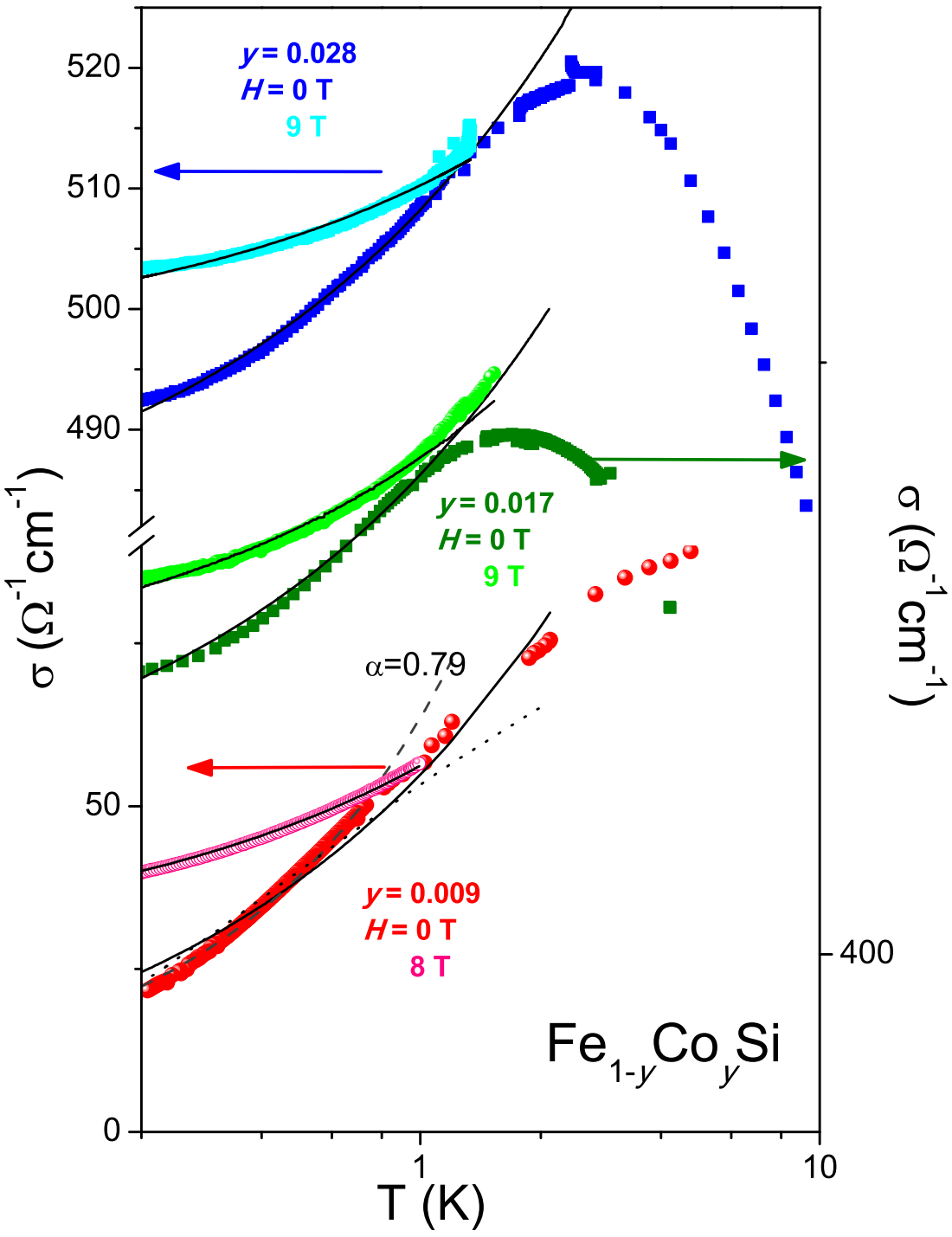

FIGURE 4.4: Conductivity (σ) vs. temperature (T) of $Fe_{1-y}Co_ySi$, $0.01 \leq y \leq 0.03$ at magnetic fields (H) identified in the figure.
Solid lines are fits to the disordered Fermi-Liquid behavior $\sigma = \sigma_0 + mT^{1/2}$.
Dashed lines are fits to $\sigma = \sigma_0 + mT^{\alpha}$ with α as marked in the figure. Dot line is the soft gap variable range hopping model fit.

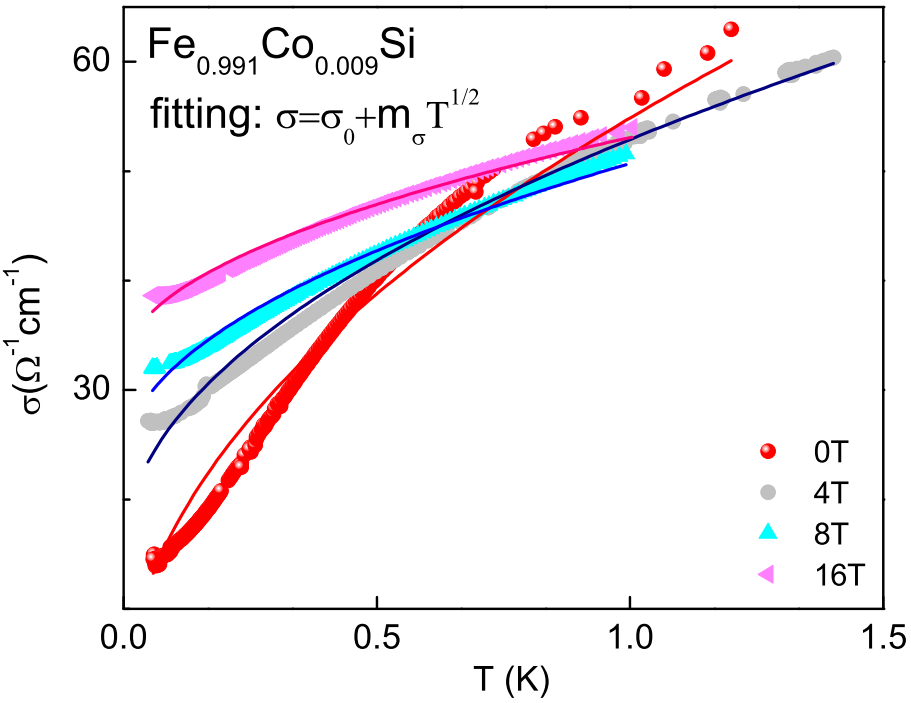

FIGURE 4.5: Conductivity vs. T for $Fe_{0.991}Co_{0.009}Si$ at various fields identified in the figure. Lines represent the best fit of disordered Fermi liquid behavior to the data.

of magnetic field similar to what we observe upon increasing y.

The field dependence of the non-FL to FL transition suggests that the non-FL behavior is associated with magnetic interactions. To evaluated the strength of the orbital contributions of the charge carriers in the system, we have performed both the transverse and longitudinal MR measurements. Orbital effects only contribute to the MR in transverse but not in the longitudinal geometry. The results of MR with the both directions at low temperatures are shown in Fig. 4.6 for $Fe_{0.991}Co_{0.009}Si$. One can see that there are negligible differences between the transverse and longitudinal MR in temperatures higher than 0.4 K where the temperature differences between two set ups are within 1 mK. The lowest temper-

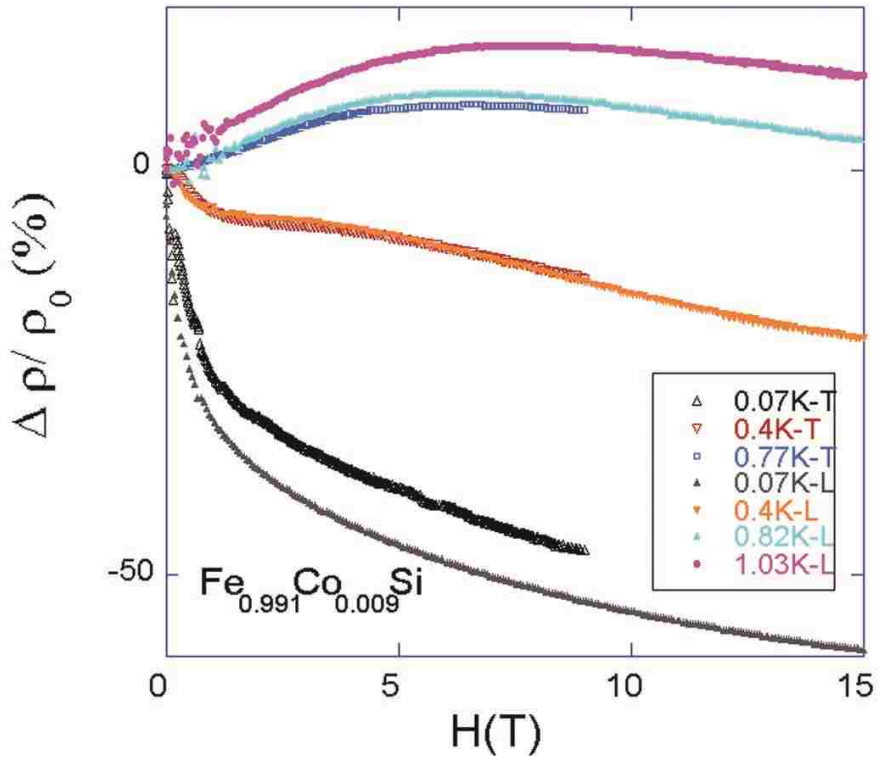

FIGURE 4.6: Transverse and longitudinal magnetoresistance for $Fe_{0.991}Co_{0.009}Si$.

ature case is sightly different due to a temperature deference of 3 mK between two geometries. Similar transverse and longitudinal MR rule out the contamination of the orbital components in charge carrier in the field dependent transport behaviors of $Fe_{1-y}Co_ySi$. The independence of MR on the angle between current and field suggest that the non-FL behavior is associated with the spin degrees of freedom of the carriers.

In doped semiconductors like Si:P, the transport properties can be described with either the Coulomb interaction model or the localization model based on the level of donor concentrations[5;14]. At dopant concentrations in proximity to the IMT the Coulomb interaction dominates and the field. The field depended resistivity at

low temperature with dominate Coulomb interaction has a form of

$$\rho(H,T) = \rho(0,0) - \alpha(\frac{4}{3} - F)\sqrt{T} + 0.77\alpha\rho^2(0,0)F(g\mu_B/k)^{1/2}\sqrt{H}. \quad (4.1)$$

Here F is a dimensionless term with $0 \leq F \leq 1$. The constant α is defined as:

$$\alpha = \frac{1}{\sqrt{T_F \frac{mD_c}{\hbar}}}, \quad (4.2)$$

with D_c diffusion constant and T_F the Fermi temperature determined by donor concentration. A positive magnetoresistance (MR) with $\sqrt{H}$ dependence can be derived from Eq. 4.1. This dependence has been observed in heavily doped semiconductors, i. e. Si:P with carrier densities approaching and larger than the critical concentration for the IMT[14].

In the model of weak localization Kawabata[5] derived a field dependent MR contribution for heavily doped semiconductors in the high field limit. This form yields a negative MR contribution as

$$\frac{\rho(H,T) - \rho(0,T)}{\rho(0,0)} \equiv \frac{\Delta\rho}{\rho(0,0)} = -0.918\rho(0,0)F(g\mu_B/k)^{1/2}\sqrt{H}. \quad (4.3)$$

Fig. 4.7 (a) shows the MR of $Fe_{0.991}Co_{0.009}Si$ at temperatures from 0.07 to 10 K. At $T = 0.07$ K, a large negative MR is observed. A few percent negative MR is also found in the prototypical semiconductor materials as Si:P on the insulating side of the IMT[14] which was attributed to weak localization contributions. However, the 60% negative MR in $Fe_{0.991}Co_{0.009}Si$ is an order of magnitude larger. This cannot be explained within the model of weak localization, not only due to the large magnitude but also because of its independence on the direction of the magnetic field with respect to the current. With increasing temperature a positive contribution to the MR most likely due to $e-e$ interactions is apparent in the low field region.

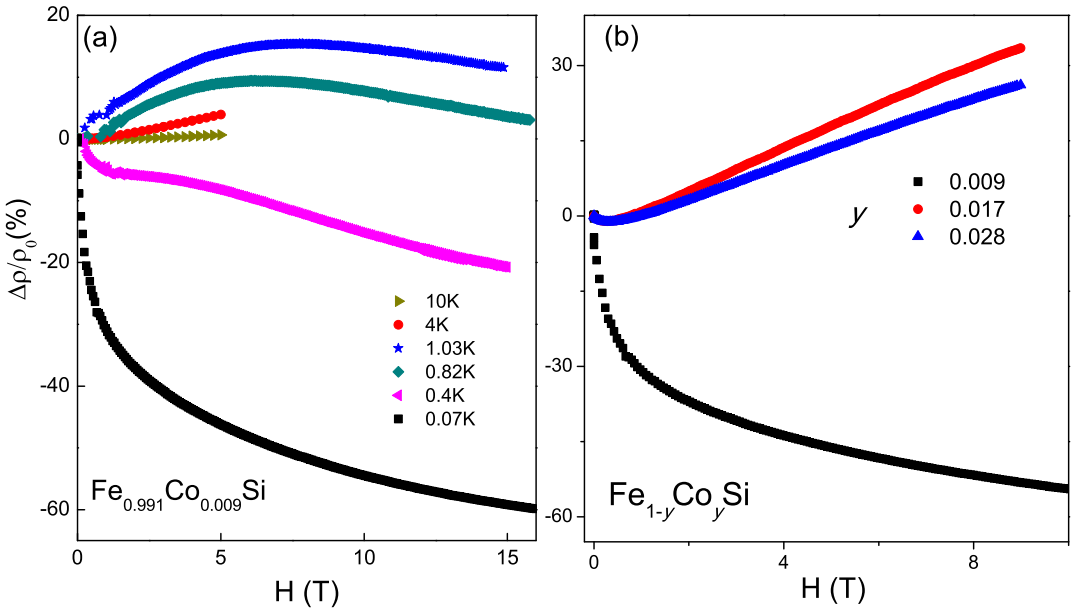

FIGURE 4.7: Magnetoresistance of $Fe_{0.991}Co_{0.009}Si$ at selected temperatures (a) and magnetoresistance of $Fe_{1-y}Co_ySi$ at $T \approx 0.07$ K (b).

Fig. 4.7 (b) displays the MR of the $Fe_{1-y}Co_ySi$ $0 < y < 0.03$ samples at $T \approx 0.07$ K. There is a significant difference in the high field MR as only the $y = 0.009$ sample displays a large negative MR. At larger y the MR is negative at small fields ($H < 1$ T) and positive at higher fields. The positive MR is expected in the $e - e$ interaction model which is thought to dominate the response of semiconductors in proximity to the IMT.

The negative low field behavior is similar to what was observed in $Fe_{1-x}Mn_xSi$ where it was shown to be associated with the non-FL behavior. Seen Fig. 4.9 where both $Fe_{1-x}Mn_xSi$ samples display a low field positive magnetoconductivity (MC) (negative MR) which is not consistent with the usual models of doped semiconductors. $Fe_{1-x}Mn_xSi$ $x \approx 0.02$ at lowest temperature distinctly deviates from an $e - e$ interaction behavior. The MC of $Fe_{0.991}Co_{0.009}Si$ and $Fe_{0.983}Co_{0.017}Si$ are also plotted in the $H^{1/2}$ scale for a direct comparison (Fig. 4.8). Consistently in

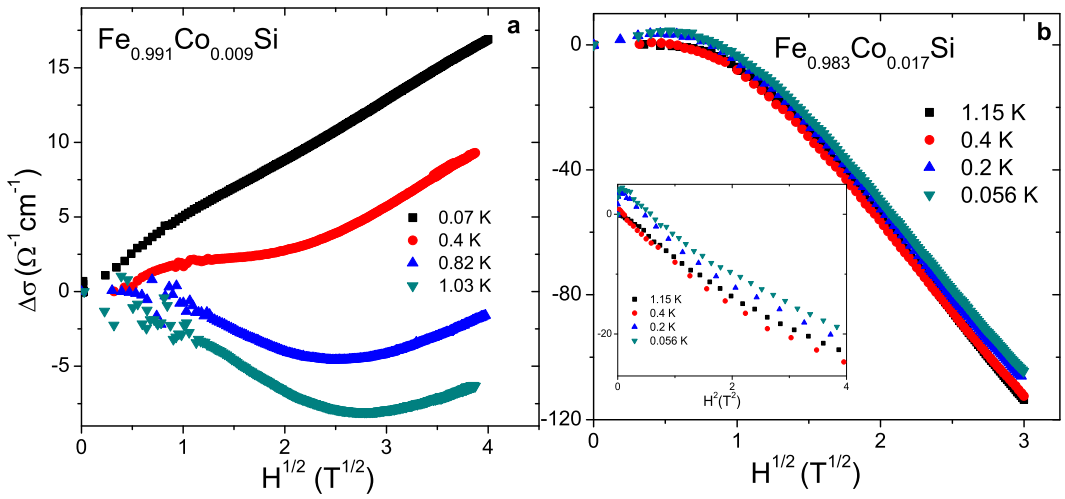

FIGURE 4.8: Magnetoconductivity of $Fe_{0.991}Co_{0.009}Si$ (a) and $Fe_{0.983}Co_{0.017}Si$ (b) plotted in $H^{1/2}$ scale. Inset: Magnetoconductivity of $Fe_{0.983}Co_{0.017}Si$ vs. H^2 plot.

$Fe_{0.991}Co_{0.009}Si$, the approximately $H^{1/2}$ dependence but opposite sign MC at high fields clearly violates the rule of Si:P. In Fig. 4.8 b, it is obvious that the MC follows the $H^{1/2}$ dependence at high fields similar to $FeAl_zSi_{1-z}$. While $Fe_{0.983}Co_{0.017}Si$ also displays a positive MC at low field as observed in the $Fe_{1-x}Mn_xSi$ $x = 0.02$ and $x = 0.04$ samples. The cross-over field of positive to negative MC decreases with increased y or increased temperature is apparent in both Co doping and Mn substituted of FeSi. In conclusion, for small doping ($y < 0.01$) and low temperatures ($T < 1$ K) an unconventional negative MR contribution dominates, while either an increased temperature or an increased y produces a more standard behavior associated with $e - e$ interactions.

4.1.2 Hall Effect of $Fe_{1-y}Co_ySi$

The Hall Effect (HE) of Fe_{1-y} Co_ySi, $0 \leq y \leq 0.1$ is shown in Fig. 4.10. Large Hall effect signals are observed in the studied crystals. The anomalous HE contributions at $y \gtrsim 0.05$ are obvious as the Hall data resemble the magnetization as a function of field for these samples. Small y samples have a HE that is nearly linear in H

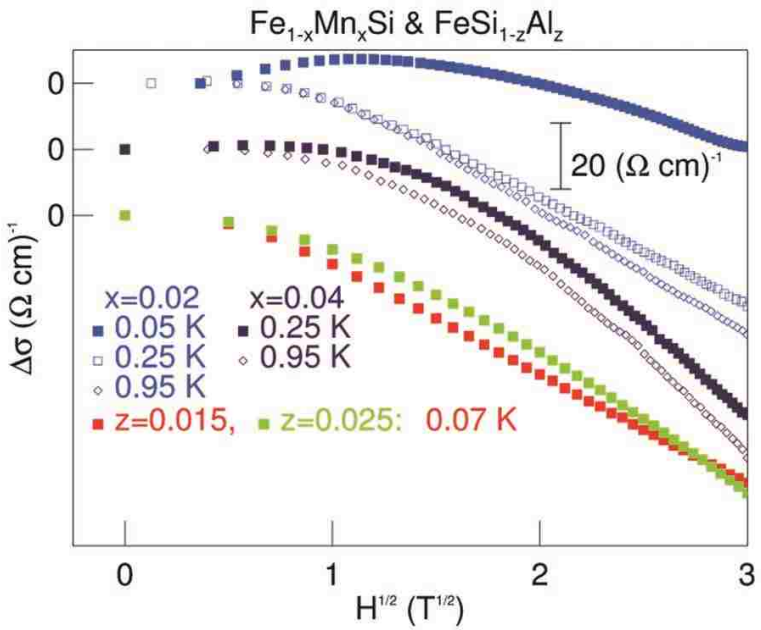

FIGURE 4.9: Magnetoconductivity of $Fe_{1-x}Mn_xSi$ and $FeAl_zSi_{1-z}$ plotted in $H^{1/2}$[7].

indicating the absence of anomalous HE contributions. Our data show a systematic decrease of normal HE with increasing y as would be expected for an increased charge carrier concentration. Due to the combined effects of the two HE contributions, a decrease of HE signal magnitude is first observed in the $y \leq 0.03$ samples and then the HE signal magnitude increases with the anomalous HE contribution dominating at larger y.

Manyala *et al*[8] reported a large anomalous HE on $Fe_{1-y}Co_ySi$ $y \approx 0.1$. They confirmed that the off-diagonal anomalous HE conductivity $\sigma_{xy} = \rho_{xy}/{\rho_{xx}}^2$ is more efficient in illustrating the anomalous contributions. The σ_{xy} contribution to the Hall conductivity is expected to be independent of charge scattering rates. This was demonstrated by a survey of σ_{xy} vs M including different group of materials from itinerant magnets, carrier hopping system and even heavy fermion systems (Fig. 4.11). Different regions in the plot display different dependence of the Hall

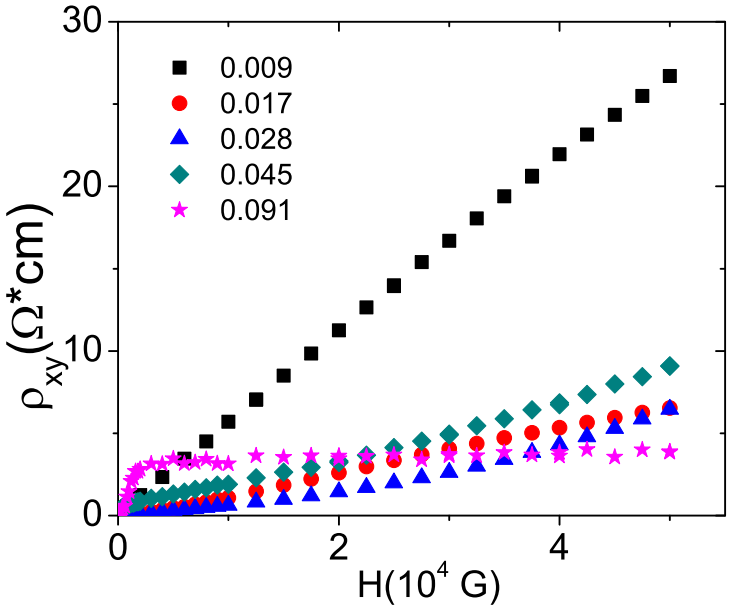

FIGURE 4.10: Hall Effect of $Fe_{1-y}Co_ySi$, $0 \leq y \leq 0.1$ at 4 K.

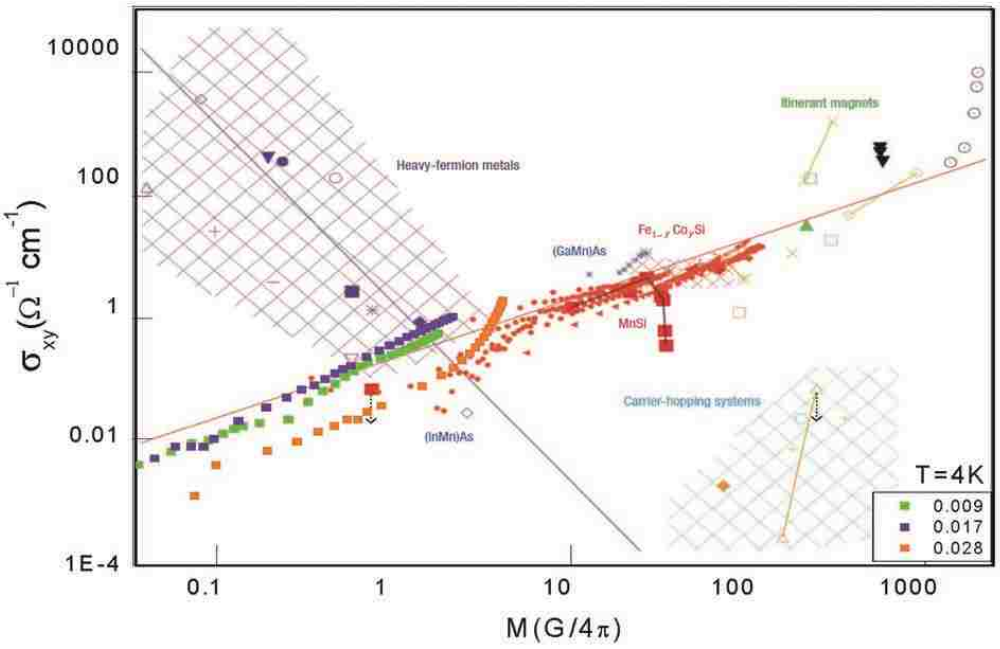

FIGURE 4.11: Hall conductivity σ_{xy} vs. magnetization M plot, showing the intrinsic nature of materials[8].
The different group of materials include itinerant magnets, carrier hopping system and the heavy fermion systems. Dilute doping or higher doping $Fe_{1-y}Co_ySi$ are all belonging to the category of itinerant magnets.

effect on the magnetization pointing out the dominance of different mechanisms in these classes of materials. It was found that $Fe_{1-y}Co_ySi$, $0.1 \leq y \leq 0.3$ shares the same behavior as the Mn-doped $III-V$ magnetic semiconductors such as (GaMn)As.

The more dilutely substituted $Fe_{1-y}Co_ySi$ samples investigated here display a similar trend in the σ_{xy} vs M figure where Dilute Co doped FeSi with $y > 0.01$ falls on top of the trend line of itinerant magnets with lower magnetization values. Therefore, despite the differences in the mechanisms of ferromagnetism, the intrinsic properties of (GaMn)As and $Fe_{1-y}Co_ySi$ are similar at low temperature.

4.2 $Fe_{1-y}Co_ySi$ Thermodynamic Properties

With the comparable transport behavior observed in Fe_{1-y} Co_ySi and in $Fe_{1-x}Mn_xSi$, the question that remains is if the non-FL in Fe_{1-y} Co_ySi shares the same origin as in Mn doped FeSi. With this question in mind I review some of the main findings from chapter 3. First, the impurity moments of both Mn and Co doping in $Fe_{1-x,y}Mn_xCo_ySi$ is consistent with an $S = 1$ magnetic moment at low x and y. Second, though majority of the Fe_{1-y} Co_ySi sample have $\Theta_W > 0$ with Θ_W systematically increasing, the low y samples close to the IMT have a negative Θ_W. This indicates the tendency for singlet formation either from the coupling of local magnetic moments associated with the Mn or Co dopants, or between the conducting charge carriers and these same moments. As a result when system is near IMT at low temperature, for either hole or electron doped FeSi, the local interaction is about the $S = 1$ local moments and $s = 1/2$ charge carriers moments in a screening effect dominated system.

Meanwhile, in section 4.1.1, we observed a non-FL behavior near IMT of Co doped FeSi similar as what has been discovered in $Fe_{1-x}Mn_xSi$ and confirmed that the non-FL only relates with spin moment interactions. All our findings in the magnetic and charge transport data suggest that the non-FL in Co doped FeSi has a same origin as in the Mn doping side - the "under-compensated Kondo effect", which leaves freely fluctuating magnetic moments at the lowest temperature. The existence of the unscreened moments at low T was verified in $Fe_{1-x}Mn_xSi$ while it was not observed in the similar hole doping nonmagnetic system - $FeAl_zSi_{1-z}$[7]. The last part of the investigation on non-FL is to demonstrate the likelihood of underscreened moments in $Fe_{1-y}Co_ySi$ at the low T. To explore the thermodynamic contribution of fluctuating magnetic moments at low temperatures in $Fe_{1-y}Co_ySi$, we have measured the specific heat in a variety of magnetic fields.

4.2.1 Specific Heat Measurement to Confirm Existence of Underscreened Spins

The top frame of Fig. 4.12 presents the specific heat data for our $Fe_{1-y}Co_ySi$ crystals with $0 \leq y \leq 0.03$ from 300 mK to 20 K. The magnitude of specific heat is increase with doping level. At zero field, all four samples display a sharp upturn in the $C(T)/T$ at the lowest temperatures measured. With an applied field, the upturns move to slightly higher temperatures and a full Schottky anomaly peak appears. The magnitude of the peak is reduced with increasing field as the entropy reduction is moved to higher temperature. There is an extended temperature range where the $C(T)/T$ is larger in fields than in the zero field. At our highest temperatures the specific heat loses its field dependence as expected for fields and temperatures of these magnitudes. The field dependence of the specific heat is observed in all samples, including the nominally pure sample since the impurity moment level extrapolated from the Curie constant is close to 0.5% in FeSi. The

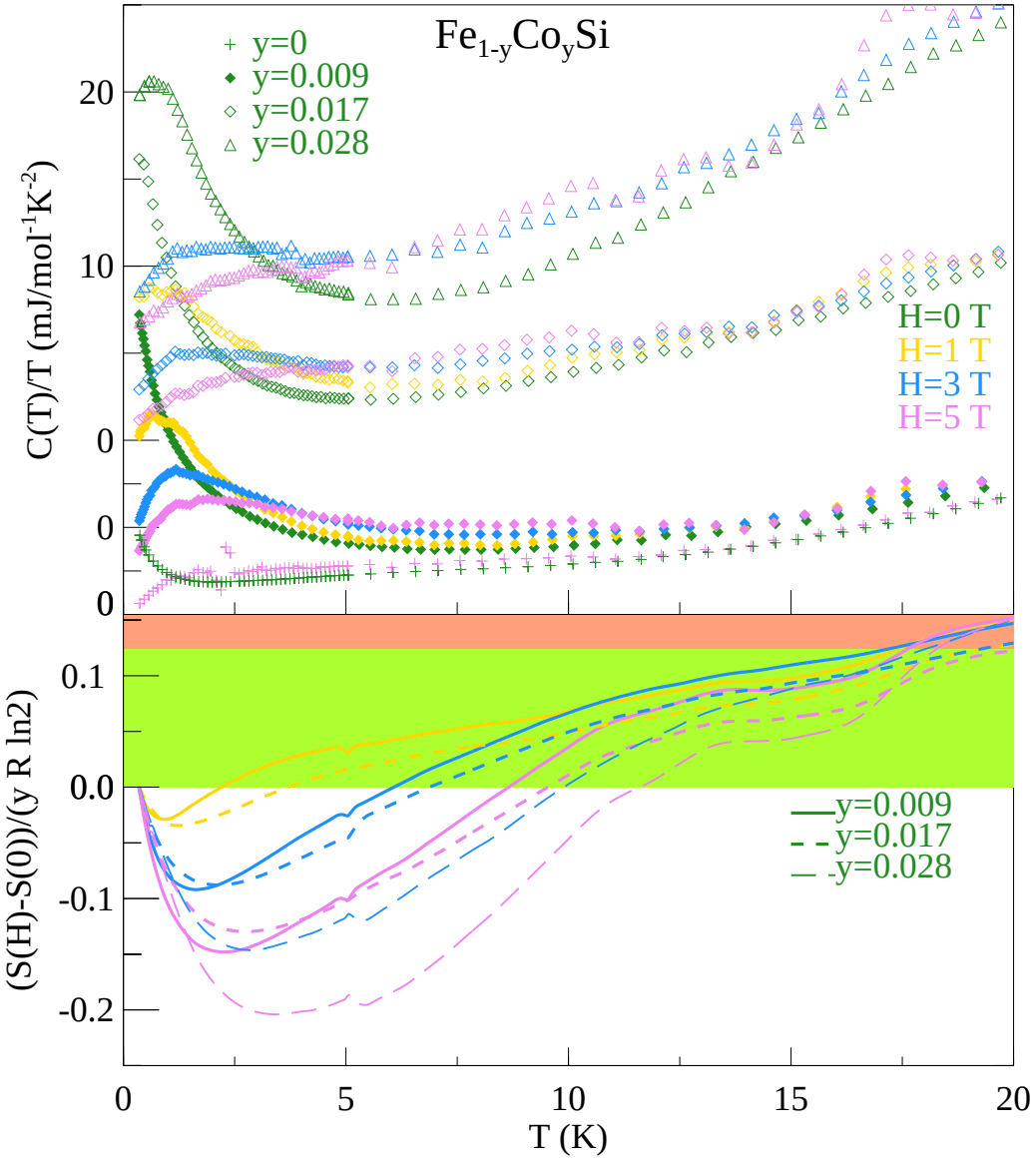

FIGURE 4.12: Specific heat divided by temperature $C(T)/T$ and change of entropy (Bottom) of $Fe_{1-y}Co_ySi$, $0 \leq y < 0.03$ for several applied magnetic fields. The change in entropy is expressed with the difference between the magnetic contribution of the in-field entropy and the zero field entropy $(S(H) - S(0))/yRln2$. R is the universal gas constant. Shade region indicates the contribution from magnetic moments that whose entropy is hidden below 300 mK at zero field.

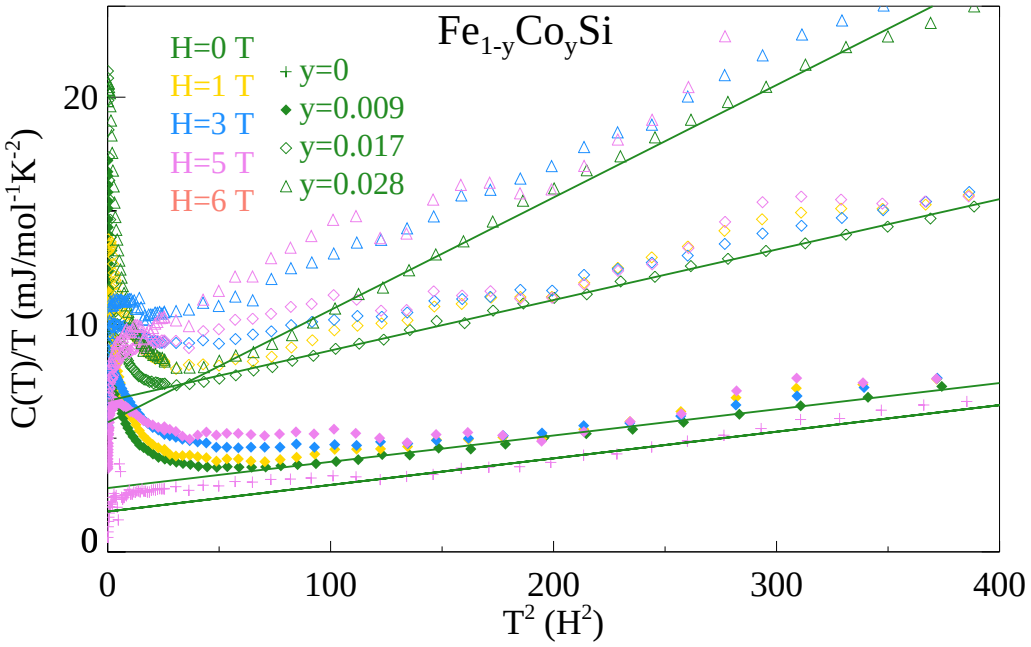

FIGURE 4.13: Specific heat $C(T)/T$ vs. T^2 for $Fe_{1-y}Co_ySi$ at various fields, H, with y and H reported in the figure. Green lines are fits of the standard form, $C(T)/T = \gamma + \beta T^2$ for a metal, to the data above 10 K.

specific heat data was fit with Eq. 2.18 (Fig. 4.13) to separate the contributions of phonons and Fermi liquid like electron gas components from the magnetic contributions. The graph shows the $C(T)/T$ in the scale of T^2 to illustrate the phonon and electron contributions. The fitting parameters are presented in table. 4.1. With increased y the electron contribution to specific heat is enlarged as expected due to the increased electron density of states. Meanwhile, there is a trend toward larger β with increased y which corresponds to a decreased Debye temperature. This is not observed in $Fe_{1-x}Mn_xSi$ where specific heat of different x samples are similar in value and shape at the higher temperature range. The consequence of the specific heat upturn in higher temperature is the significant decrease in Debye temperature which is not understood at this time.

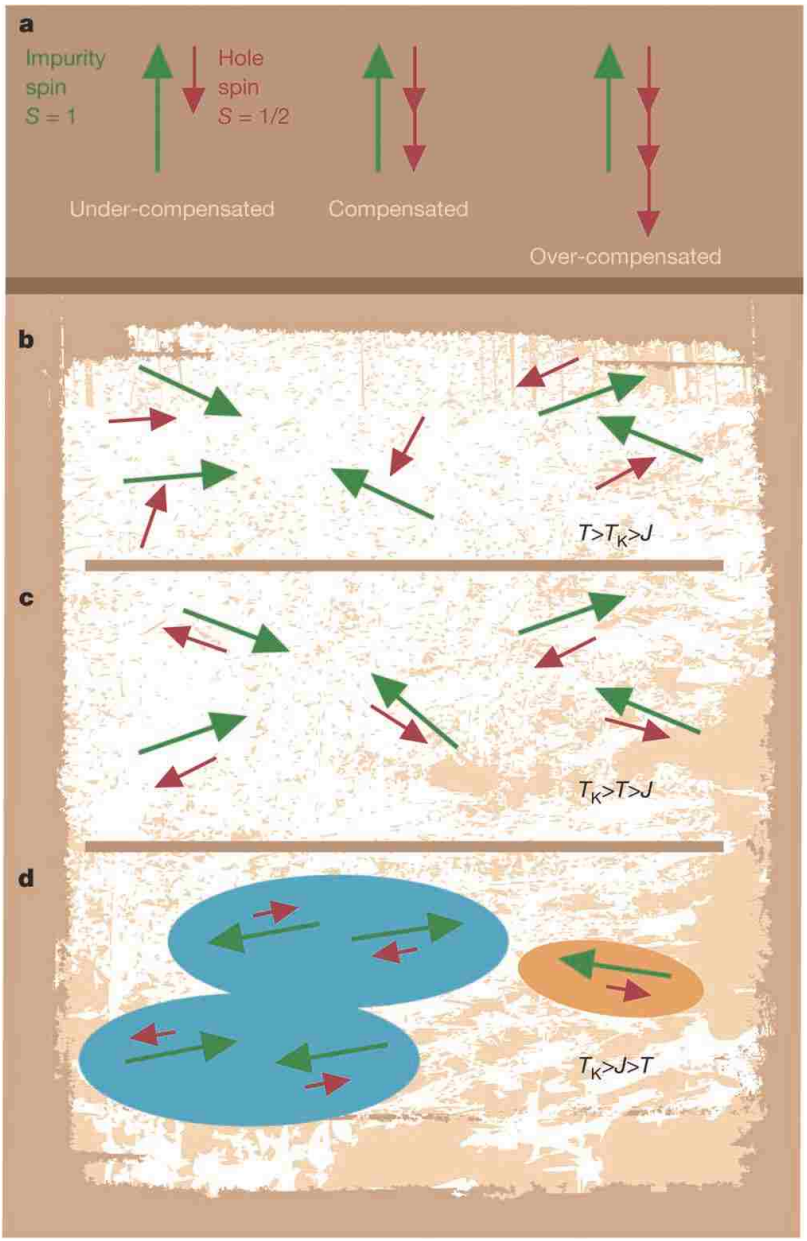

FIGURE 4.14: Undercompensated Kondo effect scheme graph.[7].
a, Comparison of underscreened, compensated and overcompensated Kondo problems. b, c, and d, Spin screening mechanisms in a magnetic semiconductor such as Mn or Co doped FeSi. Green arrows represent the impurity spin $S = 1$ and red arrows represent the charge carrier moment ($S = 1/2$). b, The random distribution of rapidly fluctuating impurity and carrier spins at high T. c, At $T \leq T_K$) the carrier gas incompletely screens the impurity spins. d, When $T \leq T_J$, the impurity moments tend to couple into screened singlets, denoted by blue shade. A few impurity moments are incompletely screened (yellow shade) and contribute to entropy.

TABLE 4.1: $Fe_{1-y}Co_ySi$ specific heat data fitting coefficients of eq. 2.18 with derived Debye temperature Θ_D for fitting.

y	γ $mJmol^{-1}K^{-2}$	β $mJmol^{-1}K^{-4}$	Θ_D K
0	1.77472	0.01170	552.06
0.09	2.80758	0.01155	554.44
0.17	6.64014	0.02219	445.99
0.28	5.69320	0.04947	341.40

To probe the existence of the uncoupled spins at the lowest temperature we calculated the entropy from our specific heat data of $Fe_{1-y}Co_ySi$. At zero field uncoupled magnetic moments occupy a manifold of degenerate magnetic states and thus the entropy associated with these states is not apparent at finite temperatures. Application of a magnetic field will split these degenerate states via the Zeeman effect allowing the entropy of these states to be apparent in specific heat measurements at temperatures where $T \sim H$. The entropy associated with these states can be found by comparing the integration of the specific heat over the temperature in finite and zero fields. With the definition of the entropy that

$$dS = \frac{\delta Q}{T} = \Big(\frac{C}{T}\Big)dT, \tag{4.4}$$

it can be obtained from the integral:

$$S(T) = \int_0^T \Big(\frac{C}{T}\Big)dT. \tag{4.5}$$

In practice the lower limit of integration is limited to the lowest measured temperature, in this case 300 mK. The differences in the result of numerical integration of the in-field entropy and the zero-field entropy of $Fe_{1-y}Co_ySi$, $0 \leq y < 0.03$ are presented in Fig. 4.12 bottom frame. It is obvious that the in-field entropy within the measured region is larger than the zero-field case. As indicated by the shaded areas above zero there is between 12 and 15 % difference for the three samples probed in our experiments. Given that entropy cannot be produced by applying

field, there must be considerable entropy at zero field which is not accessed over the range of integration (300 mK to temperature T). The presence of a magnetic field effectively splits the magnetic states by the Zeeman energy moving the low temperature entropy into the temperature window of our experiments. The missing entropy in the zero-field integration indicates that a large collection of early degenerate states persist at the lowest temperature. Those degenerate states correspond to fluctuating magnetic moments at very low temperature, well below likely Kondo screening temperature scales.

An estimate of the density of magnetic moments that are free to fluctuate below 300 mK can be obtained from the $((S(H)-S(0))/yRln2)$. This quantity represents the ratio of the unbound moments as compared to the magnetic moments induced via chemical substitution of Co for Fe. This estimate assumes a contribution of each moment being $\Delta S = Rln2$, where we have used the result from the Curie constant in chapter 3 that $S = 1$. In the case of the $y = 0.009$ sample with $T = 20$ K this estimate yields a density of 12 - 15% of the local magnetic moments associated with the Co dopants fluctuating, rather than being tied up in an ordered state or completely Kondo screened, below 300 mK. The population of the free fluctuating moments is larger than what was discovered at Mn doped FeSi. Such missing entropy in zero field is not seen in Al doped FeSi indicating that the extra low temperature entropy is more likely related to the presence of $S = 1$ magnetic moments, rather than the smaller $s = 1/2$ moments found for Al doping.

At this point, it is clear that the field dependent non-FL behavior in Co doped FeSi near IMT likely has the same origin as previous discovered on Mn doping side - the "under-compensated Kondo effect" (Fig. 4.14. a). In this scenario, the

$S = 1/2$ moments associated with the charge carries are not able to fully compensate the $S = 1$ local moments when forming Kondo singlets (Fig. 4.14. a).

Above the Kondo temperature, moments from mobile electrons are not paired with the local moments in the system (Fig. 4.14. b). When temperature drops below the Kondo temperature, the mobile moments bind with the local moments and form undercompenstated spin pairs since the $S = 1/2$ moments are insufficient to screen the equal density of larger $S = 1$ magnetic moments (Fig. 4.14. c). At lower temperatures, the remaining magnetic moments form singlets with surrounding magnetic moments (Fig. 4.14. d). This mechanism is thought to explain the low temperature behavior of common semiconducting systems near the IMT where a random AFM state is thought to develop[1]. However, in $Fe_{1-y}Co_ySi$ the extra entropy associated with the underscreened Kondo effect may be playing a role in producing a much larger fraction of fluctuating magnetic moments down to very low temperatures. The magnetic moments that do not form singlets at the lowest temperature are free to scatter charge carriers inelastically. Those scattering centers induce inelastic scattering that destabilizes the FL state, which is thought to produce NFL behavior. Meanwhile, these uncoupled moments lead to a large spin-degeneracy, which correspond to the residual entropy in zero-field that we have observed. Application of an external magnetic field Zeeman splits the degenerate states associated with the fluctuating magnetic moments reducing the effective cross section for inelastic scattering. The result is a return to Fermi liquid-like behavior in finite magnetic fields as previously observed in conductivity data.

4.2.2 Discussion of the Structure Discovered in the Specific Heat

An close examination of the temperature dependent specific heat data reveal anomalous peak structure as the temperature is scanned. The structure is observed

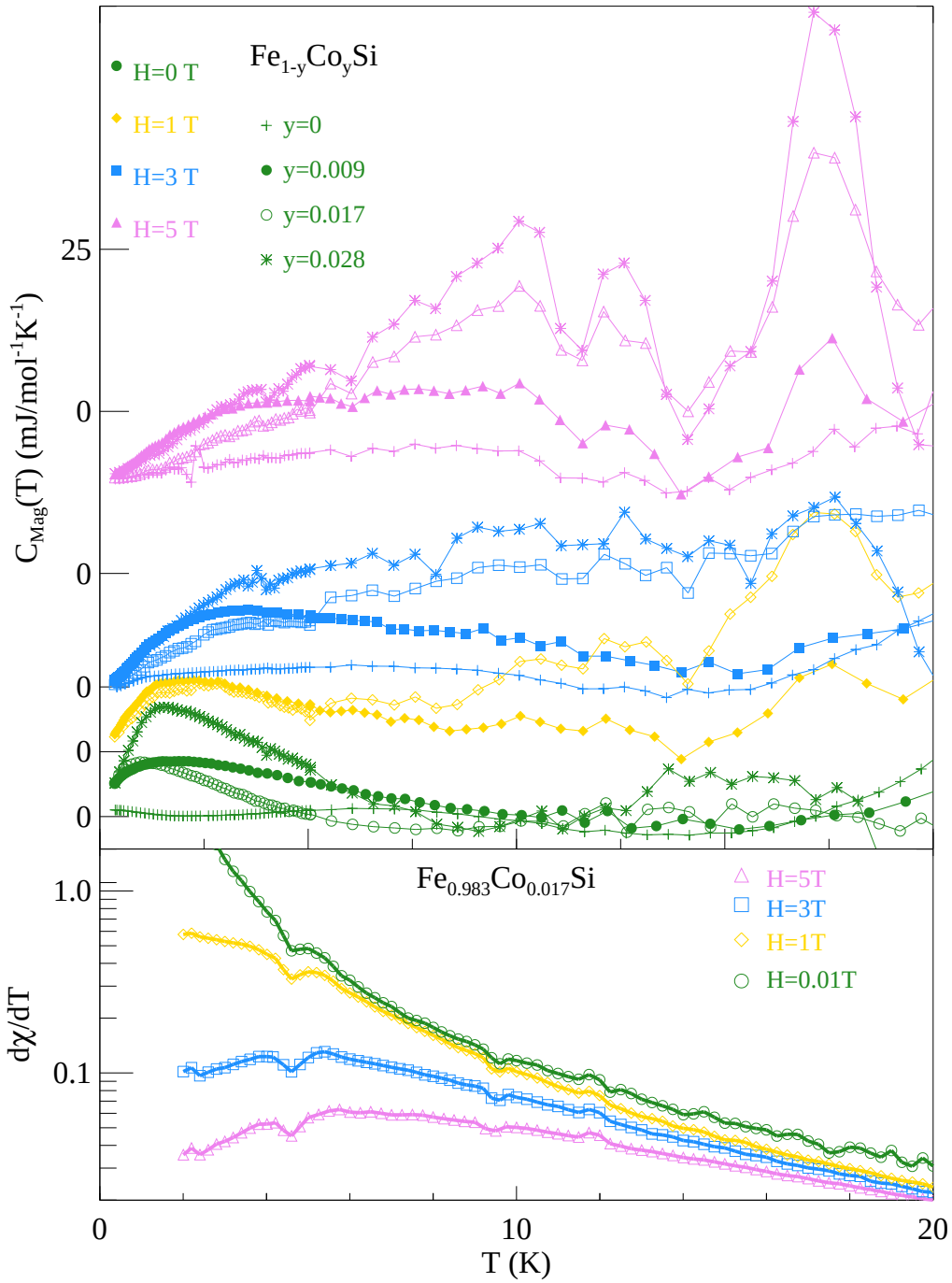

FIGURE 4.15: Temperature dependent specific heat and susceptibility structures. Top: Specific heat of $Fe_{1-y}Co_ySi$ subtracting off phonon and electron contributions. Bottom: the derivative of the susceptibility $d\chi/dT$ vs. temperature T of $Fe_{0.983}Co_{0.017}Si$ in magnetic fields identified in the figure.

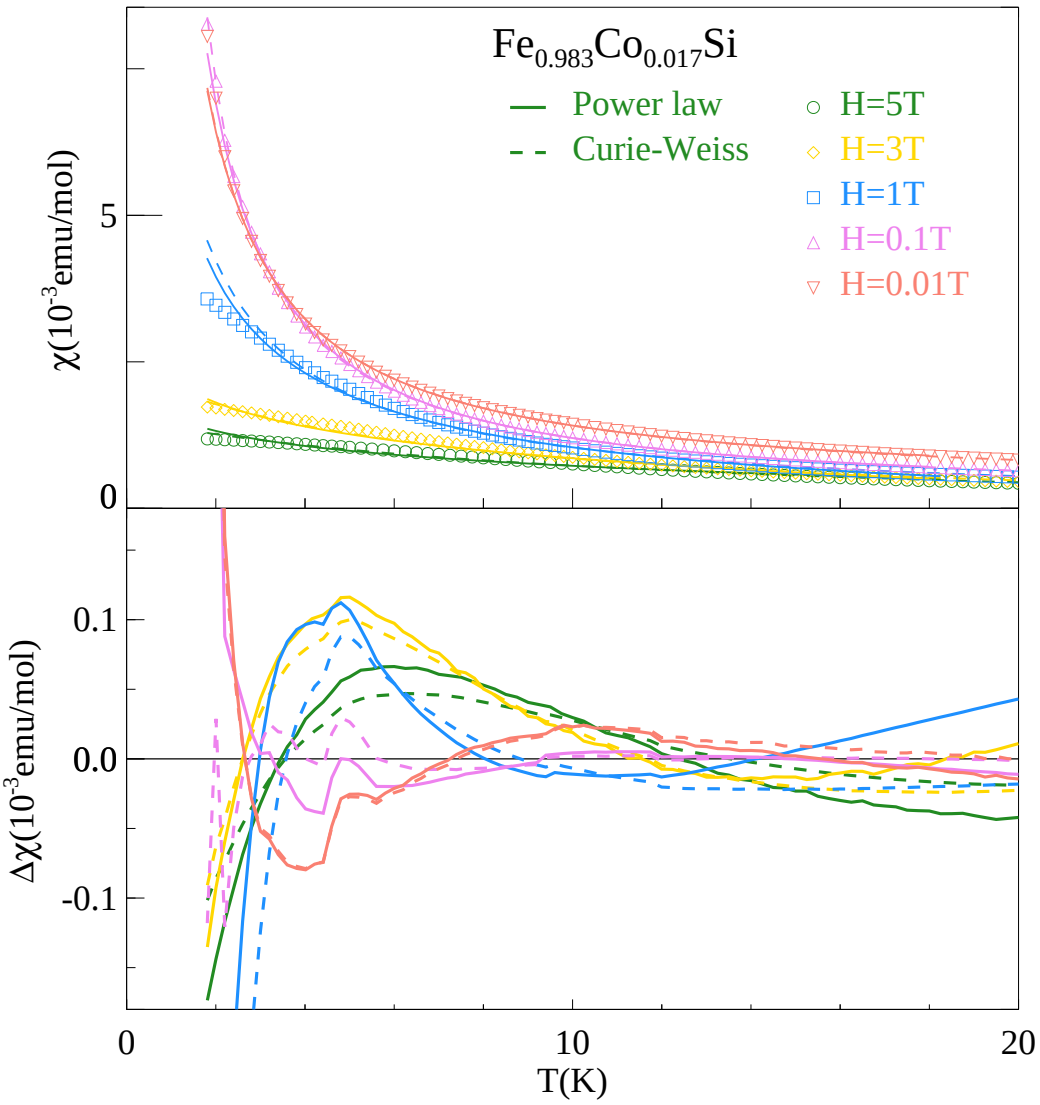

FIGURE 4.16: Analysis of the low temperature magnetic susceptibility of $Fe_{0.983}Co_{0.017}Si$.
Top: Magnetic susceptibility. Solid lines are fits of a Curie-Weiss model. Dashed lines are fits a $\chi \propto T^{\alpha}$ model. Bottom: Differences between data and the Curie-Weiss model fit (solid lines), differences between data and the power-law model fit (dashed lines).

on top of the smooth temperature dependent data expected for a non-interacting system of magnetic moments (Fig. 4.15). Such structures in the specific heat data are more apparent in finite magnetic fields and the magnitude of the anomalous peaks grow larger with increased doping levels and higher fields in the studied range.

A similarly non-monotonic temperature dependent specific heat was observed in the insulating dilute dipolar magnet $LiHo_{0.045}Y_{0.955}F_4$ that structure peak features dominated in the thermal response at low temperature[4]. In addition, there is an usual correlation between the specific heat and the susceptibility as the susceptibility is smooth. The susceptibility of $LiHo_{0.045}Y_{0.955}F_4$ follows an inverse power-law behavior rather than the Curie-Weiss law revealing an interacting picture of magnetic moments. The combination of a highly structured specific heat along with a smoothly varying susceptibility is explained with quantum entanglement - the mixing of classical ferromagnetic and antiferromagnetic contributions to the spin pair wavefunctions of free moments.

Looking back to our system, we see the possibility of similar effects existing in $Fe_{1-y}Co_ySi$. It has been confirmed through entropy study that $Fe_{1-y}Co_ySi$ has considerable density of freely fluctuating magnetic moments below our experimental temperature. Given the system dominated by Kondo screening and singlet coupling of residual moments, a biparticle interaction may exist between two nearby underscreened moments. As y is increased this system has a tendency to order ferromagnetically. At intermediate Co-concentrations, it is likely to have a partially degenerate ground state either characterized by spin glass ordering or more interestingly with a mixed FM and AFM interaction that intrigues a similar quantum

entanglement. In fig. 4.12, one can see that the hidden entropy in field is still in the process of releasing up to 20 K. This hints a relatively large temperature range for the system to recover from missing entropy of the freely fluctuating moments in zero field at the lowest temperature.

The susceptibility of $Fe_{1-y}Co_ySi$ appears to be smoothly diverging with inverse temperature. However, plotting the derivative of the susceptibility vs. temperature as in Fig. 4.15) highlights the variations away from such a smooth dependence. Here we observed that the anomalous peak structure also appears on the susceptibility data in a more subtle way. Two peaks can be easily identified on the $d\chi/dT$ vs T plot that correspond with the specific heat structure. One is below $T = 5$ K and another weaker one is near 10 K. There are hints of a third peak between 16 -18 K where there is large peak observed in the specific heat. The correlation between specific heat and susceptibility indicates a magnetic moment related underlying mechanism. In addition, a magnetic field may not simply move entropy to higher temperatures, but also play a role in bringing out the feature of the ground state as the structure of the specific heat is more profound in fields. In Fig 2.16 I display the temperature dependence of the susceptibility in $Fe_{1-y}Co_ySi$ by comparing the measured χ with a $T^{-\alpha}$ dependence and the Curie-Weiss law (Fig. 4.16). The low field χ increase faster with cooling than is predicted by the Curie-Weiss law dependence so that our power-law fits give $\alpha > 1$ ($H = 0.01T$, $\alpha = 1.3$) and a positive difference between data and fit in the lower frame. At higher fields chi increases more slowly so that a power-law fit yields $\alpha < 1$ at $H \geq 1$ T at fields that the wave structure in specific heat is observed.

In comparing $Fe_{1-y}Co_ySi$ with $LiHo_{0.045}Y_{0.955}F_4$ we must acknowledge several differences. First, instead of being a insulator, $Fe_{1-y}Co_ySi$ in our investigations ranges from insulator to metal. Second, $Fe_{1-y}Co_ySi$ is not likely well described as an Ising spin system and Kondo screening generally tends to suppress long range interactions and ordering[3]. This would make it difficult to apply a similar theoretical approach in $Fe_{1-y}Co_ySi$. In addition, the specific heat structure in $Fe_{1-y}Co_ySi$ continues to temperatures at least as high as 20 K with signatures of the same structures shown in the derivative of the susceptibility. In the current study, it is difficult to draw a conclusion of a directly comparison of $Fe_{1-y}Co_ySi$ and the $LiHo_{0.045}Y_{0.955}F_4$. However, our system provides an interesting case where spin clustering effects may exist when the system is exposed to a magnetic field suggesting that it is in a spin-liquid like state in zero field and low temperature.

4.3 Conclusion

We have discovered a similar field dependent non-FL behavior near the IMT for Co-substitution (an n-type dopant) as was discovered for Mn-substitution (p-type doping) in $Fe_{1-x,y}Mn_xCo_ySi$. The same origin - "undercompensated Kondo effect" is the mechanism we have identified for this behavior. Due to the equal densities of $S = 1/2$ charge carriers and $S = 1$ local moments that are associated with the Co substitution at low temperatures, the local moments tends to form an incomplete collective singlet state at low temperatures in a screening effect dominated system. However, neither the Kondo screening nor the low T singlet formation are sufficient to remove all the entropy from the magnetic degrees of freedom. As a result, large number of scattering centers are left at the lowest temperatures accessed in our measurements due to the presence of the underscreened moments. This results in abundance inelastic scattering of the charge carries which destabilizes of the

FL. Application of magnetic field aligns the remaining magnetic moments, thus removing the inelastic scattering and allows the system to return to a disorder FL behavior. The discoveries on both Mn and Co doping of FeSi indicate that this field depended non-FL behavior is not associated with the sign of charge carriers but instead related to the interaction between carriers and local moments.

Three scenarios have been proposed for non-FL behavior in heavy-fermion systems[13]. In the first scenario, the anomalous temperature dependence of material properties are associated with the disordered induced distribution of Kondo temperatures[10]. Non-FL behavior in a large group of the d and f electron systems are classified in this category[9;15]. The second mechanism associates the non-FL to a single-impurity. The quadrupolar Kondo effect falls under this heading, which was a mechanism proposed to describe the uranium based superconductors[2] and has been experimentally observed on GaAs/AlGaAs quantum dots[12]. The third scenario is related to a quantum phase transition (QPT), for example, $CeCu_{6-x}Au_x$ with $x_c \sim 0.1$. In $CeCu_{6-x}Au_x$, the QPT is induced by the competition between the Kondo screening effect and the RKKY magnetic ordering interaction.

Our system of $Fe_{1-x,y}Mn_xCo_ySi$ provides an interesting example of a field dependent non-FL under clear local moment and charge carrier interacting picture. This undercompensated Kondo mechanism is due to the unique $S = 1$ impurity moment of FeSi when doped with a magnetic substitution. A few rare earth materials also exhibit non-FL behavior induced by the undercompensated Kondo effect[11]. However, the non-FL behavior of the same mechanism hasn't been discovered yet in any other transition metal systems.

4.4 Bibliography

[1] R. N. Bhatt and P. A. Lee. Scaling studies of highly disordered spin antiferromagnetic systems. *Phys. Rev. Lett.*, 48:344–347.

[2] D. L. Cox. Quadrupolar Kondo effect in uranium heavy-electron materials? *Phys. Rev. Lett.*, 59:1240–1243, 1987.

[3] S. Ghosh, R. Parthasarathy, T. F. Rosenbaum, and G. Aeppli. Coherent spin oscillations in a disordered magnet. *Science*, 296(5576):2195–2198, 2002.

[4] S. Ghosh, T. F. Rosenbaum, G. Aeppli, and S. N. Coppersmith. Entangled quantum state of magnetic dipoles. *Nature*, 425(6953):48–51, 2003.

[5] Arisato Kawabata. Theory of negative magnetoresistance i. application to heavily doped semiconductors. *Journal of the Physical Society of Japan*, 49 (2):628–637, 1980.

[6] Charles Kittel. *Introduction to Solid State Physics*. John Wiley & Sons, Inc., New York, 6th edition, 1986.

[7] N. Manyala, J. F. DiTusa, G. Aeppli, and A. P. Ramirez. Doping a semiconductor to create an unconventional metal. *Nature*, 454(7207):976–980, 2008.

[8] Ncholu Manyala, Yvan Sidis, John F. DiTusa, Gabriel Aeppli, David P. Young, and Zachary Fisk. Large anomalous Hall effect in a silicon-based magnetic semiconductor. *Nat Mater*, 3(4):255–262, 2004.

[9] E Miranda and V Dobrosavljevi. Disorder-driven non-Fermi liquid behaviour of correlated electrons. *Reports on Progress in Physics*, 68(10):2337, 2005.

[10] E Miranda, V Dobrosavljevic, and G Kotliar. Kondo disorder: a possible route towards non-Fermi-liquid behaviour. *Journal of Physics: Condensed Matter*, 8(48):9871, 1996.

[11] V. N. Nikiforov, M. Baran, and V. Yu. Irkhin. Ferromagnetic Kondo lattice $CeRuSi_2$ with non-Fermi-liquid behavior. *Journal of Experimental and Theoretical Physics*, 116(5), 2013.

[12] R. M. Potok, I. G. Rau, Hadas Shtrikman, Yuval Oreg, and D. Goldhaber-Gordon. Observation of the two-channel Kondo effect. *Nature*, 446(7132): 167–171, 2007.

[13] A. Rosch, A. Schröder, O. Stockert, and H. v. Löhneysen. Mechanism for the non-Fermi-liquid behavior in $CeCu_{6-x}Au_x$. *Phys. Rev. Lett.*, 79:159–162, 1997.

[14] T. F. Rosenbaum, R. F. Milligan, M. A. Paalanen, G. A. Thomas, R. N. Bhatt, and W. Lin. Metal-insulator transition in a doped semiconductor. *Physical Review B*, 27(12):7509–7523, 1983.

[15] G. R. Stewart. Non-Fermi-liquid behavior in d- and f-electron metals. *Reviews of Modern Physics*, 73(4):797–855, 2001.

Chapter 5
Neutron Scattering Study on Fe_3Ga_4

5.1 Introduction

Incommensurate spin density waves (SDW) emerge in materials with either a Fermi surface instability known as nesting[29], as in the most extensively studied itinerant antiferromagnet chromium[8;15;19], or a long range indirect exchange interaction between local moments and conduction electrons - the RKKY interaction in the case of rare earth compounds[4;5;12;16;28]. The interplay between incommensurate order and properties like superconductivity[1–3;18;25] or ferroelectricity[14;27] are observed in a large category of materials. While Fermi surface nesting and local moments are not usually seen coexisting in one material, there are cases crossing that boundary. GdSi is a particular example[9;10], in which the RKKY interaction due the localized moments of the Gd orbitals cooperate with a Fermi surface nesting, leading to the incommensurate SDW order.

In this chapter, we discuss the metamagnetic transition metal compound, Fe_3Ga_4. In this material, there are complex interactions between local Fe moments and conducting charge carriers. We discovered that this material exhibits a incommensurate SDW structure over a intermediate temperature range likely due to the RKKY interaction.

Fe_3Ga_4 has a monoclinic crystal structure (Lattice parameters list in Table. 5.1), with 4 non-equivalent Fe sites in the unit cell as shown in Fig. 5.1. Previous studies have shown a series of magnetic transitions in this material over a wide temperature range[21;22]. Most of the previous experiments were conducted using polycrystalline

samples in establishing the framework of its magnetic phase diagram[6;13]. However, the details of its rich magnetic states and the mechanism behind the close competition of magnetic states still remain unclear.

In order to thoroughly explore the magnetism and the origin of the complex magnetic phase diagram, an investigation on the magnetic, transport, and thermodynamic properties of single crystalline Fe_3Ga_4 samples was performed in a previous study[17]. This investigation confirmed the important conclusions in polycrystalline samples and established a moderate anisotropy in the magnetic properties. The magnetic measurements indicate a ferromagnetic (FM) state below $T_1 = 68$ K as well as between $T_2 = 360$ K and $T_3 = 420$ K with an antiferromagnetic (AFM) state existing at intermediate temperatures. A sharp anomaly in the resistivity was found at T_2. A large anomalous Hall effect as well as a rather large topological Hall Effect was observed in the AFM state of Fe_3Ga_4. The anomalous field dependence of the Hall effect at different temperatures suggest changes to the electronic structure coinciding with the magnetic phase transitions while the topological Hall effect suggests that the magnetic moments in the AFM state may be non-coplanar. Electronic structure calculations suggested that the ground state can be tuned through anitsite disorder whereby Fe exists at a small density of Ga sites within the crystal structure. The calculation predicted a ground state of AFM order which shifted to a FM ground state with 1.2% antisite defects.

TABLE 5.1: Fe_3Ga_4 crystal lattice parameters at room temperature.

Formula:	$\mathbf{Fe_3Ga_4}$		Space Group:	$C2/m$
a	b	c	β	V
(Å)	(Å)	(Å)	(°)	(Å^3)
10.0979(15)	7.6670(15)	7.8733(10)	106.298(10)	585.06 (16)

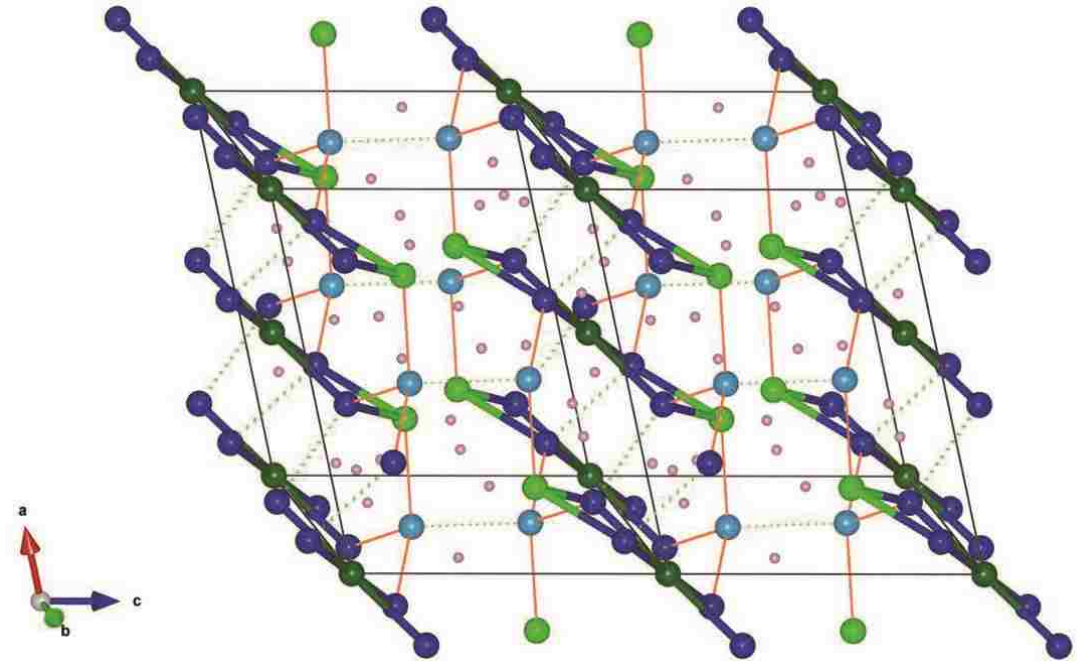

FIGURE 5.1: Crystal structure of Fe_3Ga_4 shown with 2 unit cells. Four in-equivalent Fe sites are Fe1 (Dark green), Fe2 (Green), Fe3 (Cyan) and Fe4(Dark blue). The Fe-Fe distances are indicated in three levels from 2.5 $\mathring{A}$ to 3 $\mathring{A}$ with tubes to dashed lines. There are also 4 inequivalent Ga sites plotted all in pink in this figure.

Despite the fruitful results in previous investigations, questions still remain regarding the nature of the magnetic states. Single crystal neutron scattering investigations are required to determine the character of the AFM state as well as its relation to the FM state of Fe_3Ga_4. In order to study the magnetic structure, neutron diffraction experiments have been performed using single crystals of Fe_3Ga_4 at ORNL employing the HB-3A four circle diffractometer at HFIR. Peak intensity measurements of the Bragg position confirmed FM ordering below 68 K and between 370 and 420 K. We also determined the magnetic structure in the low temperature FM state and the intermediate AFM phase between the two regions of FM ordering. A FM structure with moments lying along c direction is confirmed in the refinement result at 5 K. While the refinement result at 100 K indicates that the intermediate state consists of an incommensurate spin-density wave (SDW) struc-

TABLE 5.2: Fe_3Ga_4 crystal structure in atomic coordinate at room temperature.

No.	Site Notation	Wycoff	x	y	z	Occ.	U_{eq}(Å^2)
1	Fe1	2*c*	0	0	0	1.00	0.0049(2)
2	Fe2	4*i*	0.49442(7)	0	0.31088(10)	1.00	0.00557(16)
3	Fe3	4*i*	0.22488(7)	0	0.63791(9)	1.00	0.00511(16)
4	Fe4	8*j*	0.13563(5)	0.20024(7)	-0.15176(7)	1.00	0.00542(12)
5	Ga1	4*i*	0.26998(6)	0	0.08446(8)	1.00	0.00849(14)
6	Ga2	4*i*	0.04142(6)	0	0.34817(8)	1.00	0.00825(14)
7	Ga3	8*j*	0.60841(4)	0.20297(6)	0.15127(5)	1.00	0.00794(11)
8	Ga4	8*j*	0.35194(4)	0.18674(6)	0.44958(6)	1.00	0.00889(11)

ture with a wavevector of $q \approx 0.27c^*$. In this complex SDW structure there is a significant out of plane magnetic moment that is likely the cause of the topological Hall signal. Field depended studies indicate that the SDW wave state coexist with FM state above the high temperature transition for a magnetic field of $H = 0.5$ T.

5.2 Magnetic Structure Investigation of Fe_3Ga_4 with Neutron Diffraction

5.2.1 Crystal Preparation and Experimental Techniques

High purity (99.999%) Fe powder and (99.999%) gallium pieces were first melted in an RF induction furnace in an Argon atmosphere to synthesis polycrystalline Fe_3Ga_4. Single crystals of Fe_3Ga_4, of mass up to 700 mg, were synthesized from the polycrystalline charges employing either the floating zone technique or a modified Bridgman method in an RF furnace. To reduce non-equilibrium defects, the resulting single crystals were sealed in quartz tubes under vacuum and annealed at 550 °C for 48 hours. The crystal structure was confirmed with powder X-ray diffraction and further determined via single crystal X-ray diffraction using a Nonius Kappa CCD diffractometer (Mo $K\alpha$, $\lambda = 0.71073$ Å). We confirmed the *c*-centered monoclinic structure (space group $C2/m$)[21;22]. The refined atomic coordinates for Fe and Ga at room temperature are given in Table. 5.2.

Different temperature x-ray diffraction studies was performed within the temper-

ature range 5 - 295 K in a previous investigation of Fe_3Ga_4[6]. No structure change was found in all temperatures indicating there is no significant coupling between the lattice and the magnetism in Fe_3Ga_4 below ambient temperature. To continue the investigation above room temperature, we have performed powder X-ray diffraction (XRD) studies at several temperatures between 300 - 670 K to investigate the structure change through T_2, T_3 and the small change in high temperature susceptibility[17] observed at 650 K. We have also examined the temperature range 300 - 380 K in 10 K steps with single crystal XRD to search for a possible connection between crystal structure and the magnetic transition at T_2. Within the entire temperature range no structure change or abrupt lattice parameters changes were observed in both our single and powder XRD results (Fig. 5.2). Therefore, the mechanism behind the close competition of the magnetic states and re-emergence of ferromagnetism at high temperature is not related to any structural changes but instead may depend on more subtle mechanisms such the exchange between magnetic moments and itinerant electrons.

A single crystal of mass 24 mg was chosen for magnetic structure determination via neutron scattering. The magnetic properties of the sample were first measured with a MPMS to check the magnetic states and the magnetic transition temperatures. The sample was pre-aligned with the single crystal X-ray diffractometer to determine a, b and c axial directions. The single crystal neutron diffraction investigation was performed using the HB-3A four-circle diffractometer at the High Flux Isotope Reactor of Oak Ridge National Laboratory with neutron wavelength of 1.536 $\mathring{A}$. The crystal was placed in a close-cycle refrigerator allowing a temperature range of 5 - 450 K to be explored. Initial coordinates for UB-matrix calculation was taken from the X-ray scattering refinement. The UB-matrix is the Miller index

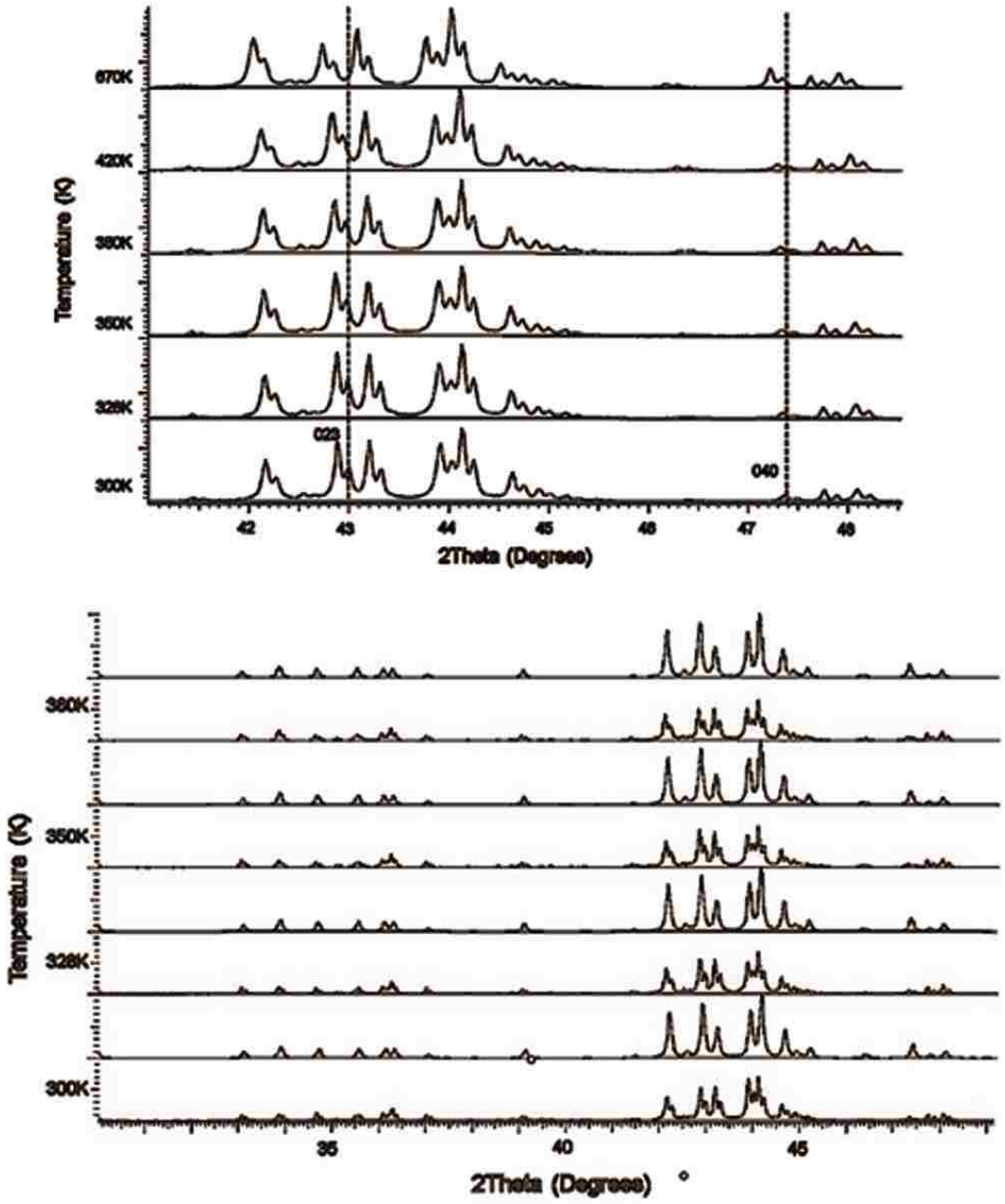

FIGURE 5.2: Selected powder X-ray diffraction patterns across high temperature magnetic transition (Courtesy of Katherine Benavides and Julia Chan, University of Texas, Dallas.)

connecting the reciprocal space position of (hkl) to the Cartesian coordinate (xyz) in lab reference system with the zero goniometer position of the instrument. The FM order parameter was obtained by scanning the temperature dependence of the (1 1 1) and (2 0 1) Bragg reflections over the 5 to 450 K range. Wave-vector scans along the (2 0 L) direction with $0.4 \geq L \leq 1.1$ were collected at large numbers of selected temperatures to determine the magnetic phase diagram. In addition, a large volume of the reciprocal space was scanned at 5 K and 100 K collecting all of the low q reflections at Bragg position as well as all of the low q magnetic peaks associated with the AFM ordering. Altogether 94 peaks were used for a full refinement of the FM state at 5 K and 154 q-scans taken at 100 K were employed in determining the AFM structure. Wave vector scans along (2 0 L) were also collected with the sample exposed to a 0.5 T magnetic field with a permanent magnet. Refinements of the magnetic structures were performed using the FULLPROF program suite [23].

5.2.2 Magnetic Structure Refinement and Magnetic Moment Calculation

Assuming that all the atoms (n^{th} unit cell, ν^{th} atom) in the crystal have a magnetic moment, a moment vector $\mu_{n\nu}$ for each atom can be defined giving amplitude and direction of this magnetic moment. This periodic moment distribution can be Fourier expanded as

$$\vec{\mu}_{n\nu} = \sum_{n\nu} m_{\nu k} e^{2i\pi \cdot \vec{R}_{n\nu}}, \tag{5.1}$$

where $\vec{k}$ is the propagation vector and $\vec{R}_{n\nu}$ is the atomic coordinate of the specific atom in unit cells. $m_{\nu k}$ is a complex Fourier transform parameter that associates with the propagation vector $\vec{k}$: $m_{\nu k} = Re_{\nu k} + iIm_{\nu k}$.

Given that the magnetic atom position is based on the underlying nuclear structure, the wave vector $\vec{k}$ in the summation has a periodicity in the reciprocal space. One can chose wave vectors in the unit cell of the crystal groups, i.e. within the first Brillouin zone of unit cell.

The differential magnetic cross section is:

$$\frac{d\sigma_N}{d\Omega}(\vec{Q}) = \frac{(2\pi)^3)}{V} N \sum_{\vec{H}} \sum_{\vec{k}} m|\vec{F}_N(\vec{Q})|^2 \delta(\vec{Q} - \vec{H} - \vec{k}), \tag{5.2}$$

where N is the number of unit cells contained in the crystal, $\vec{Q}$ is the scattering vector and $\vec{H}$ is the lattice vector. $\vec{F}_N(\vec{Q})$ is the unit cell magnetic structure factor in non-polarized neutron beam:

$$\vec{F}_N(\vec{Q}) = p \sum_{\nu} f_\nu(\vec{Q}) \mu_{n\nu} e^{i\vec{Q}\cdot\vec{r}_\nu}. \tag{5.3}$$

$\sum_\nu$ sums over the scattering from atoms in the unit cell. When $\vec{Q} = \vec{H}$, as limited by the δ function, function, the Bragg condition is satisfied for the particular reciprocal lattice[23].

With a determined propagation vector, integrated magnetic peak intensities, and knowledge of nuclear structure, one can deduce the $\vec{F}_{N\perp}(\vec{Q})$ for all the magnetic peaks. From here, it is possible to refine the coupling, direction and magnitude of the Fourier components $\mu_{\nu k}$ with constrains of the crystal structure and symmetry groups.

With the relation of $-\vec{k} = \vec{k}^*$, the moment vector can be expressed as

$$\vec{\mu}_{n\nu} = \sum_k Re_{\nu k} \cos(\theta_{n\nu} + \psi_{k\nu}) + Im_{\nu k} \sin(\theta_\nu + \psi_{k\nu}), \tag{5.4}$$

where $\theta_{n\nu} = 2\pi\vec{k} \cdot \vec{R}_{n\nu}$ is the scattering angle and ψ_{kv} is the magnetic phase factor. $\vec{R}_{n\nu}$ is the positional vector of atom:

$$\vec{R}_{n\nu} = (x_v \cdot \vec{a} + y_v \cdot \vec{b} + z_v \cdot \vec{c}) + (n_a \cdot \vec{a} + n_b \cdot \vec{b} + n_c \cdot \vec{c}). \tag{5.5}$$

Here (x_v, y_v, z_v) is the atomic coordinates of the atom site in unit cell and n=(n_a, n_b, n_c) defines "the n'th the unit cell" from the origin where the atom is located. The summation of Eq. 5.4 is arranged for the propagation vectors over pairs of $(\vec{k}', -\vec{k})$. The coefficients of the real and imaginary parts correspond to the Fourier decomposition. Thus, with known crystal structure and a group of well refined basis vector coefficients, one can obtain the magnitude and direction of magnetic moments of any atoms in the crystal cell with Eq. 5.4 and Eq. 5.5.

To obtain the coefficients of the moments or moment vectors after Fourier transformation Eq. 5.1 is used to determine the magnetic structure. To perform the refinement one needs the initial crystal structure data information as well as a large number of neutron scattering magnetic peaks with the peak reciprocal lattice index, peak position in d-space (or 2θ), and the peak intensity determined. In a relatively simple structure case such as the low temperature FM state of Fe_3Ga_4, one can obtain the magnetic moment on each site directly from the refinement with Fullprof since the magnetic structure is commensurate.

Determining an incommensurate structure such as the AFM structure of Fe_3Ga_4 is a more complex task. The crystal symmetry is reduced when materials undergo AFM transitions so that the original four inequivalent Fe sites break into seven inequivalent Fe sites. In the AFM state, a propagating SDW structure is found for its complicated moment distribution. The magnetic moment vector rather than the moment magnitude is produced in the refinement result. The magnetic peaks were taken at 100 K, where the AFM peak intensity is nearly the strongest. The 100 K data refinement was first carried out with no symmetry restrictions between the symmetry split Fe-sites. This yields a SDW structure with Fe-sites that are

structurally equivalent having the same average and maximum magnetic moments. Based on the refined basis vector coefficients, the AFM moments could be calculated using Eq. 5.4. At 5 K the magnetic structure refinement yielded a structure of FM ordering with moments lie along c direction.

The AFM magnetic structure is produced with the following procedure to render the magnetic moment on each atomic site. For a particular site (x_ν, y_ν, z_ν), the position of all $\vec{R}_{n\nu}$ is created by adding the translation to the nearby cells (n_a, n_b, n_c). θ_{nv} is derived in fractional coordinates. The base vector coefficients and the basis vectors in the refinement output are employed to create the specific coefficients $Re_{n\nu k}$ and $Im_{\nu k}$ of the 7 Fe sites. With the $\theta_{n\nu}$, $Re_{n\nu k}$ and $Im_{\nu k}$ determined, one can now directly derive the magnetic moment magnitude of each axial direction following Eq. 5.5. The calculation procedures outlined above and the following magnetic structure imaging were performed with a package of originally composed IDL codes.

5.2.3 Results and Analysis

Fig. 5.3 displays the results of q-scans along the (2 0 L) $0.4 \geq L \leq 1.1$ plane which reveal an incommensurate an incommensurate magnetic ordering peak in the intermediate temperature AFM state. The temperature dependence of Bragg scattering and the scattering from the incommensurate magnetic ordering is dramatic. With temperature approaching 48 K, a weak magnetic ordering peak first emerges at (2 0 0.74) with a relatively narrow width. As temperature is increased toward T_1 the incommensurate peak increases in intensity and evolves to slightly lover L values while the (2 0 1) Bragg peak suddenly decreases in intensity at $T1$. At 100K the incommensurate AFM peak is centered at (2 0 0.73) with a strong intensity. When the temperature rises toward T_2, the AFM peak grows wider and gradually

diminishes. In summary, the magnetic scattering evolves with temperature with L varying from 0.7 to 0.8 clearly demonstrating the incommensurability of the AFM state.

The temperature dependence of the scattering intensity at the (2 0 1) Bragg po-

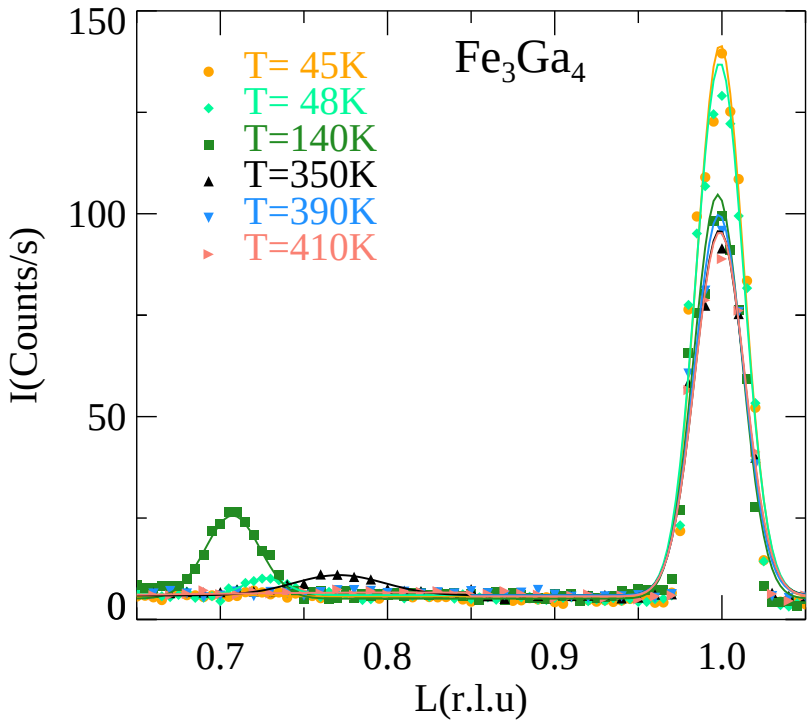

FIGURE 5.3: Neutron diffraction along the (2 0 L) direction at various temperatures in $H = 0$ T.

sition, which is closely related to the FM order parameter, can be better viewed in Fig. 5.4. b. Similar behavior was also observed on the (1 1 1) Bragg peak intensity scans. Fig. 5.4 presents a comparison between the intensity of the (2 0 1) Bragg peak and *dc* susceptibility, χ, of the same crystal taken at a field of 0.01 T. Two temperature regions with extra scattering at the (2 0 1) Bragg position are consistent with the temperature where χ is large, illustrating their ferromagnetic behavior.

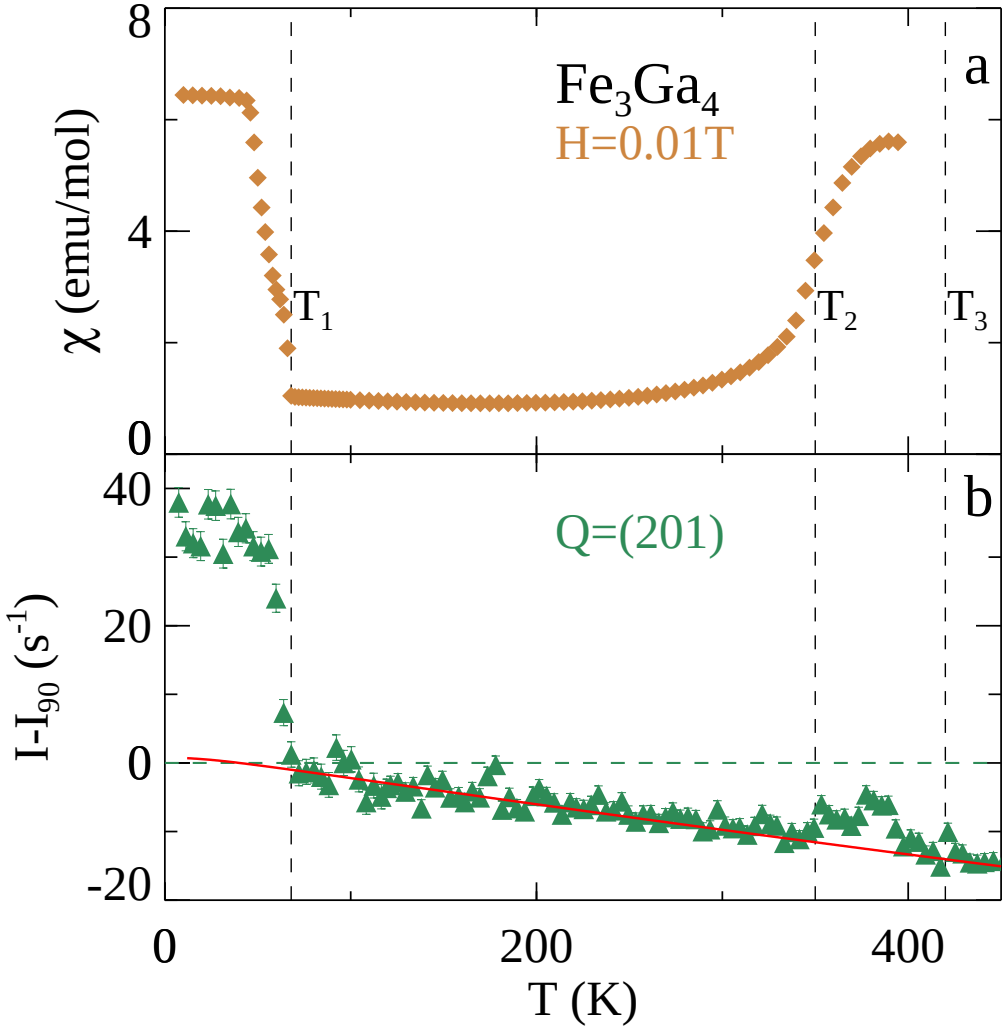

FIGURE 5.4: Temperature dependence of the magnetic scattering intensity and *dc* susceptibility of Fe_3Ga_4.
The magnetic scattering intensity of the (2 0 1) Bragg reflection, $I - I_{90}$, is taken as the intensity, I, measured at temperature T after subtraction of the scattering intensity at $T = 90$ K, I_{90}. $T = 90$ K is chosen as a background since Fe_3Ga_4 is ordered antiferromagnetically at this temperature. Dashed lines at $T_1 = 68$ K, $T_2 = 360$ K and $T_3 = 420$ K indicate the three transitions of Fe_3Ga_4 in the studied temperature range.

In order to verify that there is no other contributions beside the thermal effects in the Bragg scattering intensity of intermediate state a fit of the expected Debye-Waller (DW) dependence using the Debye temperature determined from specific heat measurements[17;20;24] is displayed in Fig. 5.4 b (red line). The DW factor is the correction factor for the lattice thermal vibration induced decrease of scattering intensity on the Bragg position:

$$I = I_0 \exp(-2M). \tag{5.6}$$

With M approximated as:

$$M = B(sin\theta/\lambda)^2, \tag{5.7}$$

Here B is the Debye parameter:

$$B = \Big(\frac{12h^2}{mk_b\Theta_M}\Big)\Big[\frac{\Phi(y)}{y} + \frac{1}{4}\Big]. \tag{5.8}$$

Θ_M is the mean Debye temperature and $\Phi(y)$ is the Debye integral:

$$\Phi(y) = (1/y)\int_0^y [\exp(x) - 1]^{-1} x dx. \tag{5.9}$$

Here $x = (h\nu/k_BT)$ and $y = (h\nu_m)/k_BT = \Theta_M/T$. A commonly used half-numerical expression for DW parameter B[20] is in the form of

$$B = (11492/A)\frac{T}{\Theta_D^2}\Big[\Phi(\frac{\Theta_D}{T}) + \frac{1}{4}(\frac{\Theta_D}{T})\Big](A^{-2}). \tag{5.10}$$

Θ_D is the Debye temperature, which was obtained from ref.[17] as Θ_D=125 K. A is the atomic weight in the unit of ^{12}C. The Debye integral was also obtained numerically. The $sin\theta/\lambda$ can be derived from the Bragg scattering law, with $n = \sqrt{h^2 + k^2 + l^2}$, (h, k, l) = (2, 0, 1) and d=3.355 $\mathring{A}$. Thus, the DW factor can be calculated and fitted to the scattering intensity. This part of analysis were carried out with a Matlab code.

As can be seen from the quality of the fit to the data, the decreased Bragg intensity as the temperature increases is consistent with the thermally increasing DW factor excluding the extra scattering due to FM order. There appears to be a large difference between the magnetic scattering intensity at $q = (2\ 0\ 1)$ for $T_2 < T < T_3$ and that at $T < T_1$. The reason for the weak scattering at high T FM state is likely to be the usual decrease of the magnetization as the Curie temperature is approached. A detailed investigation of the magnetic scattering in this temperature regime is needed to ruled out a more complex magnetic order for $T_2 < T < T_3$. However, it is clear that the magnetic ordering has a FM component and we do not detect any additional scattering outside of that meeting the Bragg condition.

As mentioned in section 5.2.1, we have carried out an extensive survey of the scattering in reciprocal space at 5 - 100 K in order to fully characterize both the low T FM state as well as the intermediate incommensurate AFM state. These surveys have allowed us to refine the magnetic structures of both states. The results of the refinement for the low T FM state are presented in Table 5.3. In Table 5.3, we report both the atomic positions of the four crystallographically distinct Fe positions in the monoclinic crystal structure as well as the magnetic moment on each corresponding site calculated with the magnetic moment constrained to the crystallographic c-axis. The magnetic structure is plotted in Fig. 5.5. A. The size of the magnetic moments corresponds well to the results of *Mössebauer* experiments[13] and are in general agreement with the average magnetic moment determined from magnetization measurements[6;17]. The magnetic moment is constrained to lie along the c-axis since the refinement result along the a and b directions yields only small contributions that are no larger than the error bars in the refinement ($\sim$0.3 μ_B).

TABLE 5.3: Magnetic structure data for the low temperature ferromagnetic state at 5 K. m^* is taken from *Mössebauer* experiments[13].

Atom Site	**Atomic Coord. a**	**b**	**c**	**Moment(μ_B)** m_c	m^*
Fe1	0	0	0	1.54(28)	1.75
Fe2	0.4935(6)	0	0.3096(7)	1.20(22)	1.33
Fe3	0.2240(7)	0	0.6376(8)	1.24(21)	1.15
Fe4	0.1352(5)	0.2019(5)	-0.1519(6)	1.49(12)	1.48
m_{mean}				1.37(22)	1.36

Therefore, we neglect any non-collinear magnetic moments as their existence is beyond our ability to discern in the low temperature FM state of Fe_3Ga_4.

Table 5.4 lists the magnetic moments determined from the refinement of the magnetic peaks at 100 K for the AFM order. In the AFM state of Fe_3Ga_4 the 4 nonequivalent Fe crystallographic sites in the unit cell split into 7 nonequivalent positions based on the symmetry group reduction since they have differing locations along the c-axis which is the propagation direction of the SDW. The crystallographic equivalent Fe-sites at different c positions are no longer equivalent in the new magnetic unit cell with the wavevector propagating along c-axis. The refined structure is consistent with a SDW structure with a propagation vector of $q = [0, 0, \delta], \delta = 0.27$ at $T = 100$ K. The resulting moments on the 7 nonequivalent sites have large variations. Due to the incommensurate nature of the ordering, the moments from cell-to-cell along the propagation will change accordingly. The averaging over 1600 ($4 \times 4 \times 100$) unit cells shows that the magnetic moments has a maximum amplitude of 2.38(8) μ_B. The total average magnetic moment is 1.30(4) μ_B which is within error of the average moment in the low T FM state. In addition, the averaged magnetic moment magnitudes of Fe sites in each crystallography symmetry are also comparable to the FM magnetic moment magnitudes. In the AFM state at 100 K the magnetic moments are mostly along the a-axis

with a maximum of 2.30(6) μ_B and mean of 1.24(3) μ_B. However, there are considerable contributions that lie along the crystallographic b- (m_{max}=0.57(7) μ_B and m_{mean}=0.37(4) μ_B) and c axis (m_{max}=0.58(2) μ_B and m_{max}=0.31(1) μ_B) directions as non-linear and non-coplanar components. The magnetic moment along the b-direction is found only for Fe sites 6 and 7 which are equivalent in the unit cell (Fe4). Though b components only exist on 4/9 of the atoms, they are not negligible and are in similar amplitude of the more ubiquitous magnetic moments in the c-direction.

A graphic rendering of our refined magnetic structure at 100 K is shown in Fig. 5.5. C where the variation in the magnetic moments is presented over five Fe_3Ga_4 unit cells to include more than one full period. Compared with the SDW materials such as Cr[8;15], the SDW state of Fe_3Ga_4 is more complex. Fig. 5.5. B is a plot of the 100K magnetic structure projected to the $b-c$ plane. It is clear how the moments with b-axis contributions lie on the Fe sites 6 and 7 which originate from the splitting of the crystallographic Fe4 sites. This confirmed the previous suggestion of the existence of a non-coplanar magnetic moment based on the large topological Hall effect in the intermediated temperature AFM state[17]. Meanwhile, the large variation of magnetic moments indicates the richness of the magnetic interaction in this system.

Now a comparison of the effectively competing magnetic states in Fe_3Ga_4 can be easily made by looking at Fig. 5.5. A and C. The direction of the magnetic moments are along the c-axis at the FM state, while they lie mainly along the a-axis in the AFM structure. There is clearly a spin reorientation at the T_1 transition. As stated in previous study[17], the mechanism that drives this transition and leads to

spin orientation is temperature and field dependent. The magnitude of the moment depends on its corresponding crystallographic Fe sites and is modulated in cells with the incommensurate SDW propagation. The magnetic moments within $a-c$ layers are close to parallel, contract to Cr, which has an incommensurate SDW phase that exhibits AFM interaction between nearest neighbors[8;15].

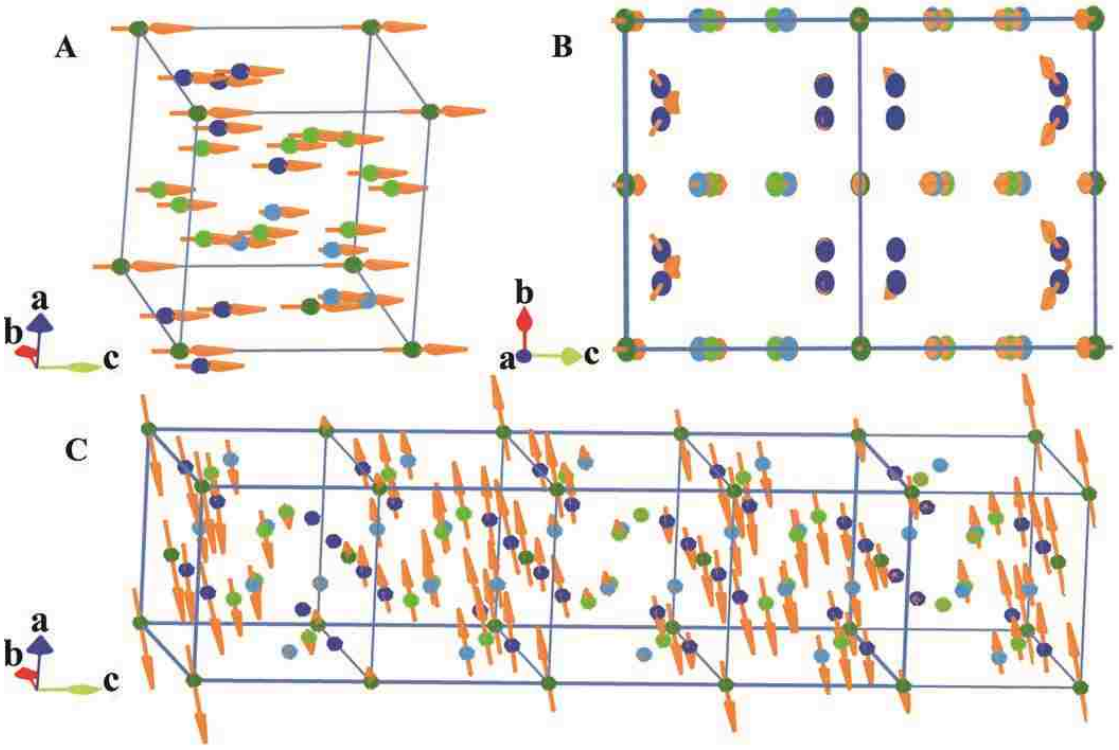

FIGURE 5.5: Refined magnetic structures of T=5 K Ferromagnetic (FM) state and T=100K incommensurate spin density wave (SDW) state.
A: Magnetic structure of T=5 K FM state in one unit cell. B: Magnetic structure of the incommensurate state at T=100 K projected to the $b-c$ plane. C: Magnetic structure of the incommensurate SDW state at T=100 K shown in five unit cells along propagation direction. The Fe atoms are categorized into different colors based on the crystallographic nonequivalent Fe sites: Fe1 (Dark green), Fe2 (Green), Fe3 (Cyan) and Fe4 (Dark blue).

TABLE 5.4: Magnetic moments for the seven different Fe sites of one particular unit cell in the intermediate temperature AFM state ($T = 100$ K) with statistics of moments over 1600 ($4 \times 4 \times 100$) unit cells. Here the mean value of b direction is calculated just on the Fe sites 6 and 7.

Fe	**Atomic Coord.**			**Moment**(μ_B)			$m_{mean}(\mu_B)$				$m_{max}(\mu_B)$			
	a	**b**	**c**	**a**	**b**	**c**	**a**	**b**	**c**	$\|m\|$	**a**	**b**	**c**	$\|m\|$
1	0	0	0	-2.31(6)	0	0.58(2)	1.47(4)	0	0.37(1)	1.51(4)	2.31(6)	0	0.58(1)	2.38(6)
2	0.4944	0	0.3108	-1.55(4)	0	0.38(1)	1.02(2)	0	0.25(1)	1.05(4)	1.61(4)	0	0.40(1)	1.65(4)
3	0.5055	0	0.6891	-0.96(3)	0	0.24(1)	1.02(2)	0	0.25(1)	1.05(4)	1.61(4)	0	0.40(1)	1.65(4)
4	0.2248	0	0.6379	-0.95(3)	0	0.24(2)	1.16(3)	0	0.29(1)	1.20(5)	1.83(4)	0	0.46(1)	1.88(5)
5	0.7751	0	0.3620	-1.79(5)	0	0.45(2)	1.16(3)	0	0.29(1)	1.20(5)	1.83(4)	0	0.46(1)	1.88(5)
6	0.1356	0.2002	0.1517	-0.22(1)	0.06(1)	-0.05(1)	1.32(2)	0.37(4)	0.33(1)	1.41(8)	2.08(3)	0.58(6)	0.52(1)	2.22(8)
7	0.8643	0.2002	0.8482	-2.00(3)	-0.56(7)	0.50(1)	1.32(2)	0.37(4)	0.33(1)	1.41(8)	2.08(3)	0.58(6)	0.52(1)	2.22(8)
m_{mean}				0	0	0	1.24(3)	0.32(2)	0.31(1)	1.30(4)	-	-	-	-
m_{max}				-	-	-	-	-	-	-	2.31(6)	0.58(7)	0.58(2)	2.38(8)

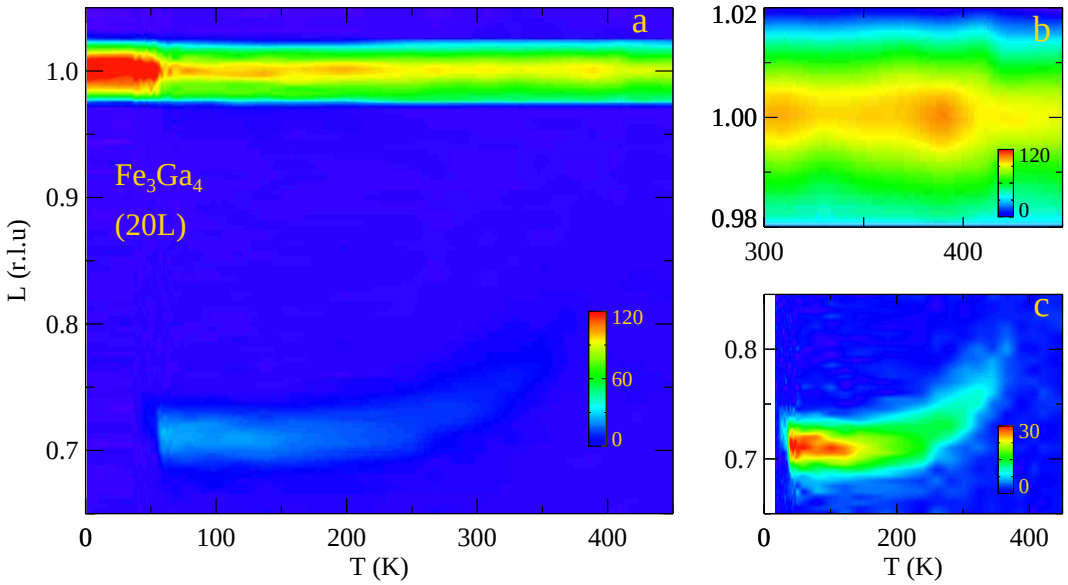

FIGURE 5.6: Temperature, T, dependence of the neutron scattering intensity in the (2 0 L) direction.
a: the intensity map of the scattering in the (2 0 L) reciprocal lattice direction. Scans were performed with L varying between 0.65 and 1.05 reciprocal lattice units (rlu) in increments of 0.005 rlu over T range of 5 - 450 K. b: the $300 \leq T \leq 450$ K region showing the additional scattering at the (2 0 1) Bragg peak position above 330 K. c: the scattering at the incommensurate wavevector (2 0 1-δ) for $5 \leq T \leq 450$ K with δ evolving into smaller values as the system approaches the T_3. Color-bars indicate the scattering intensity in counts/s.

A summary of our neutron scattering data at zero field is presented in Fig. 5.6. There are three features of this plot that represent the main experimental findings in the zero field neutron scattering study of Fe_3Ga_4. First is the large increase in the scattering cross section at the (2 0 1) Bragg position below 68 K demonstrating a robust FM ordering that is consistent with previous measurements of the magnetization and the *Mössebauer* spectrum of Fe_3Ga_4[13;17]. When temperature rises above T_1 the reduced scattering at the Bragg position is accompanied with an increase of scattering at (2 0 1-δ) representing the presence of an incommensurate SDW phase with propagating vector (0,0,δ) with $0.2 < \delta < 0.3$. The details of the

T and q dependence of this scattering contribution can be better viewed in Fig. 5.6. **c** where an abrupt loss of scattering is evident near T_1 while a more continuous change is evident above 300 K. At these higher temperatures, the peak center position moves to somewhat higher q before the intensity of the peak is reduced below the level of the background scattering at T_2. In the $T_2 < T < T_3$ temperature range the scattering at the (2 0 1) Bragg position increases in intensity as can be observed in Fig. 5.6. **a** and **b** before abruptly decreasing at T_3. This behavior is also consistent with the previous magnetization measurements, which indicate a paramagnetic state above the high T FM state. To conclude, in Fe_3Ga_4 there is a strongly FM ordered state below T_1 which transitions to an incommensurate SDW state for $T_1 < T < T_2$. There is a re-emergence of ferromagnetism at T_2, however we have not ruled out a more complex ordering in this temperature range.

SDW transitions are often accompanied by sharp changes to the Fermi surface which can modify the charge carrier conduction properties. The conductivity, σ, as shown in Fig. 5.7 and Fig. 5.8 is measured with current flowing along c-axis and b-axis respectively. It were also measured in a transverse magnetic field of 0.5 T in the same current directions. As magnified in the insets, there are small anomalies that appear at T_1 and T_2 position indicating changes in the electronic structure and a partial Fermi surface gapping (and gap closing) associated with the SDW phase. It is clear that the charger carrier density is modified and a sudden change of conductivity appears. When the system transitions from a high T FM to the incommensurate SDW state an energy gap at the Fermi surface opens. As the temperature decreases this gap grows with the internal magnetic fields increasing. The Fermi surface structure appear to recover as the gap closes when entering the FM state at both T_1 and T_2 from the incommensurate SDW state. Accompanying

this change is a charge carrier density increase and a discontinuity appears on the conductivity data.

In Fig. 5.7 the conductivity anomaly at T_2 is smaller than the anomaly at T_1, with $\Delta\sigma_2 = 0.082(m\Omega \times cm)^{-1}$ comparing to $\Delta\sigma_1 = 0.457(m\Omega \times cm)^{-1}$. At low temperatures thermal scattering is reduced resulting a larger value of the conductivity when no other interactions are present. As a result, the change in relative conductivity at the transitions can be taken as a true reflection of the extent of Fermi surface that is gapped by the presence of the SDW state. We obtained the ratio of the conductivity change as $\Delta\sigma_2/\sigma_2 = 1.75\%$ and $\Delta\sigma_1/\sigma_1 = 3.41\%$ indicating that the gap decreases with temperature in the SDW state. Due to the relative large value and rapid change trend of the conductivity at low T it's not surprising that even a wider gap induced discontinuity might not be always easily measurable. As the discontinuity at T_1 is less apparent on the conductivity curve when current was added along the b axis. The T_2 behavior is, in contrast, always noticeable on top of a relatively slowly varying resistivity. With a moderate sized magnetic field the transition becomes slower as indicated by the greatly smoothed T_2 discontinuity.

The anomalies in the conductivity at the magnetic phase transition temperatures can be directly compared to rare earth elements and compounds where the mechanism behind the SDW instability is RKKY coupling. As in the rare earth Dy, the incommensurate magnetically ordered state originates from indirect exchange (RKKY coupling)[5;7]. As Dy evolves from a paramagnetic state into a SDW state a gap open up at the Fermi surface as a result of the ordering. These gaps become larger as the magnetization builds up below T_N. It is believed that as the gap

grows the RKKY coupling is reduced so that the metamagnetic field is suppressed. At about 85 K the metamagnetic field is reduced to zero so that the FM state becomes the zero field ground state.

The character of the magnetism in transition metal compounds is typically more itinerant than in f-electron materials In Fe_3Ga_4 complex interactions render rich magnetic moment contributions in non-equivalent Fe sites including the emergence of non-coplanar moments. The large (1.3 μ_B) and diverse moments suggest the existence of more localized magnetic moments. No sign of nesting in the complex Fermi surface was found in the theoretical simulations[17], which makes the RKKY mechanism a reasonable explanation for the mechanism causing the development of an SDW state in Fe_3Ga_4. It is not typical for a Fermi surface-nesting caused SDW state to be unstable towards ferromagnetism as these materials have a SDW ground state[2;8;26]. While materials with RKKY interaction induced SDW are often observed to go through transitions from a high T PM to SDW and end up with a FM ground state[5;7;28] as the RKKY can be greatly reduced by the development of energy gaps at the Fermi surface. A direct Fermi surface study, such as an ARPES experiment, could be employed to confirm this conjecture.

The effect of a magnetic field on the SDW phase and the transition temperatures between the FM and SDW phases are demonstrated in Fig. 5.9. This figure displays the integrated intensities of the (2 0 1) Bragg peak representing the FM order parameters in $H = 0$ and $H = 0.5$ T. A comparison of the two curves shows that the temperatures where low T FM phase is stable has been dramatically increased by the application of $H = 0.5$ T field. Fig. 5.9. b shows the integrated intensity of the peak at $(2\ 0\ 1 - \delta)$ indicative of the spin density wave state at the same two fields. It is obvious that the temperature range of the SDW wave has been greatly

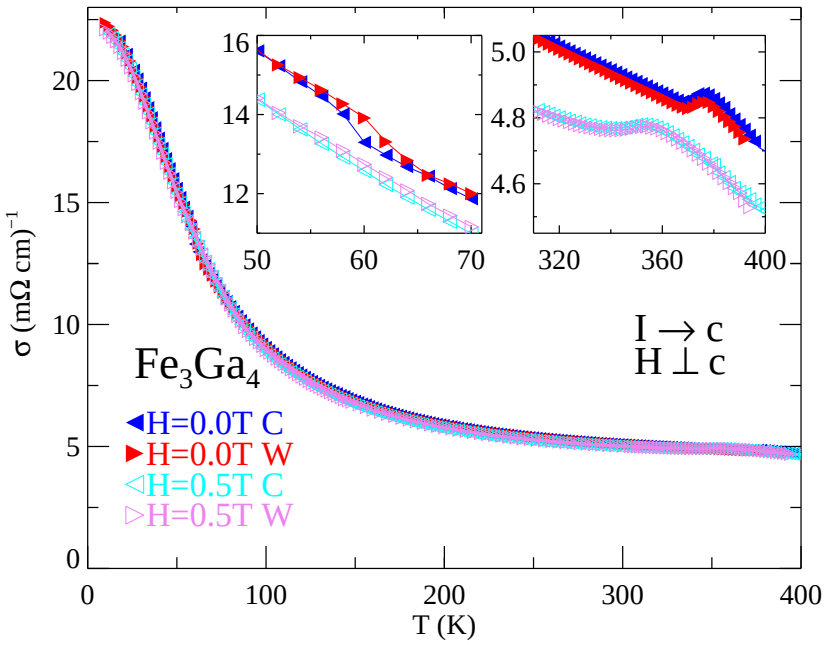

FIGURE 5.7: Temperature, T, dependence of the conductivity with current along c direction.Data in field are displaced by -1 $(m\Omega \times cm)^{-1}$ (low T) or -0.15 $(m\Omega \times cm)^{-1}$ (high T) for ease of view.

reduced due to the increasing of T_1. As evidenced by the dramatic increase in T_1 with the application of field, one can conclude that although the field doesn't have an apparent effect on the size of the magnetic moments, the stability of the low T FM state over the SDW state is increased substantially. The high sensitivity to moderately sized magnetic fields is one of the defining features of Fe_3Ga_4 and a sharp metamagnetic transition is first identified in the previous magnetization measurement[17]. Here, the neutron scattering data confirms that moderate field substantially favors low T FM state.

Fig. 5.9. c displays the SDW wavevector, δ, dependence on T at both fields. The SDW shows signs of being influenced by the lattice, which would favor a commensurate state, and the RKKY interaction, which ought to be rather temperature independent. As we have stated in section 5.2.1, through a wide temperature range

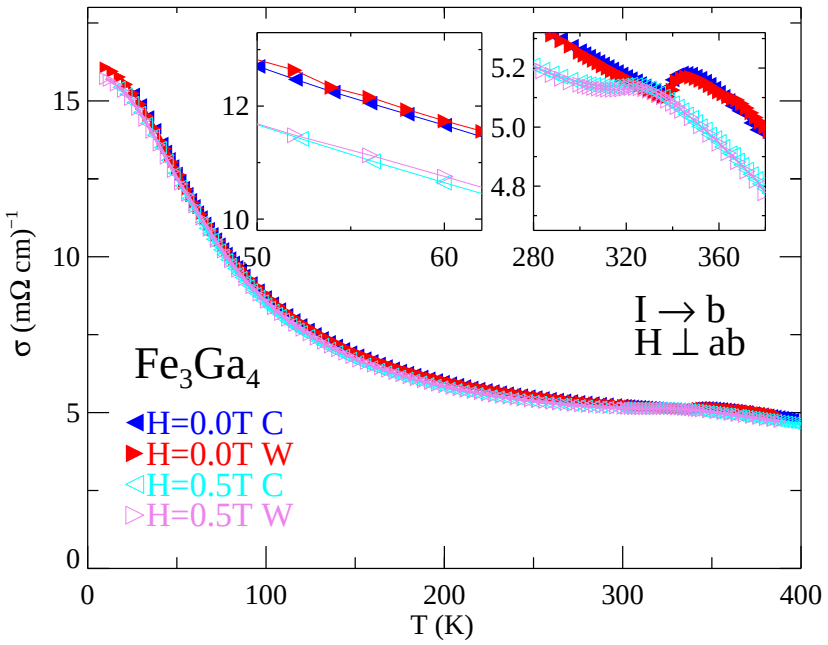

FIGURE 5.8: Temperature, T, dependence of the conductivity with current along b direction. Data in field are displaced by -1 $(m\Omega \times cm)^{-1}$ (low T) or -0.15 $(m\Omega \times cm)^{-1}$ (high T) for ease of view.

XRD study there are only very subtle changes to the lattice constants at the magnetic transition temperatures indicating small coupling between the lattice and the magnetic states. Thus, the system never enters a commensurate SDW phase. The competition between the coupling to the lattice and the natural RKKY ordering vector is less apparent when a field is applied. At $T > 300$ K the significant decrease in δ with T that has been observed at $H = 0$ is replaced by a nearly constant δ at $H = 0.5$ T.

Fig. 5.9 d displays the correlation length determined from fits of the resolution function convoluted to a Lorentzian to the q-dependence of the AFM scattering peaks. At zero field, the incommensurate SDW peaks begins to broaden around 200 K leading to small correlation length of 80 $\mathring{A}$ near T_2. The correlation length in a field of 0.5 T has a similar T-dependence but appears to have an even smaller

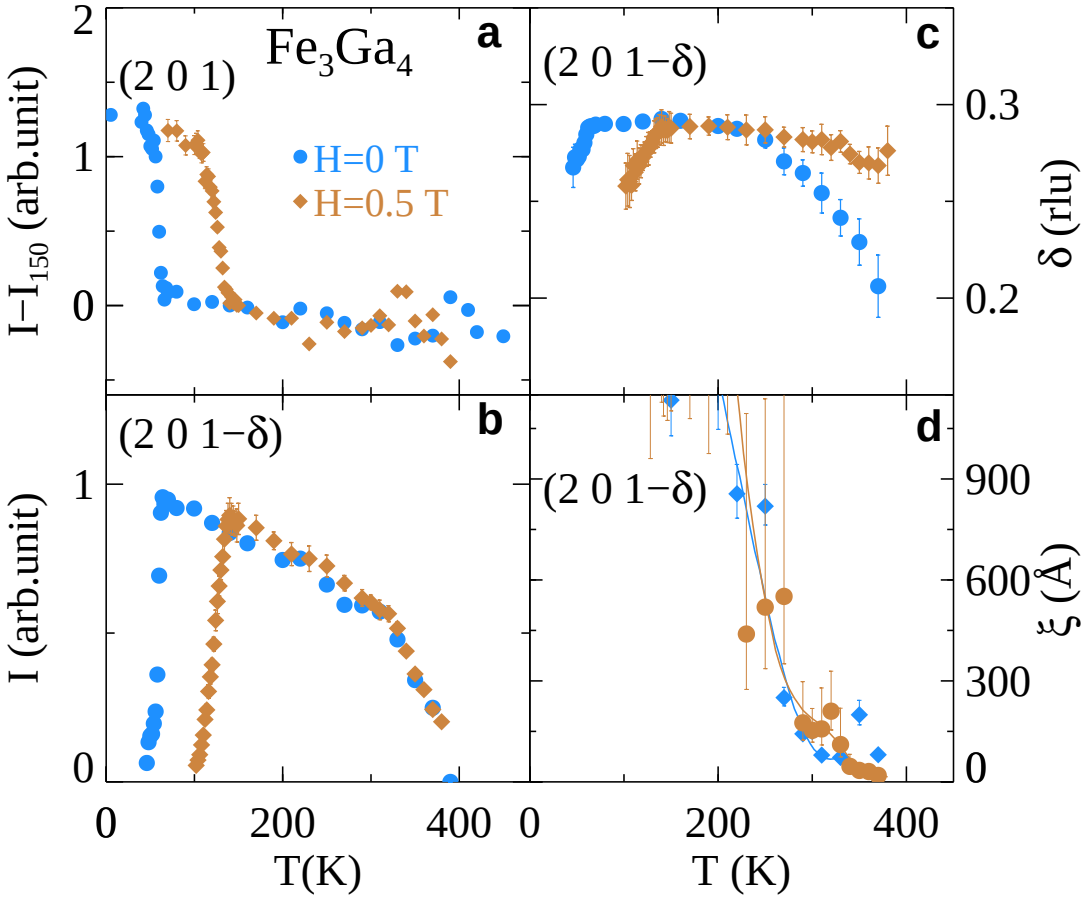

FIGURE 5.9: Temperature dependence of magnetic states of Fe_3Ga_4 studied in H=0 T and H=0.5 T.
a: Temperature, T, dependence of the integrated intensity, I of the (2 0 1) Bragg peak after subtraction of the integrated intensity at 150 K, I_{150} at magnetic fields, H, of zero and 0.5 T. The T range where the ferromagnetic phase is stable is dramatically increased by the application of moderate H. b: Integrated intensity, I, of the peak discovered at (2 0 1-δ) indicative of the spin density wave state displayed at $H = 0$ and $H = 0.5$ T. c: The temperature dependence of δ at the same fields. d: Correlation length of the AFM peaks are extracted by fitting the (2 0 1-δ) AFM peaks with a profile of the resolution function convoluted Lorentzian function. Solid lines are guides to the eye.

value as it approaches - and seemingly exceeds - T_2. This suggests an interesting scenario that the SDW phase coexist with the high T FM state in Fe_3Ga_4. Together with the nominal change of the SDW wave vector and the stabilization of the FM state in field, this experiment presents evidence that a real case that metastable SDW state can coexist with ferromagnetism when under the influence of an external magnetic field[11].

5.3 Conclusions

In this chapter, we discussed the results of the neutron scattering investigation of Fe_3Ga_4, in which we discovered the magnetic structure of the low temperature FM state and the intermediate temperature AFM state. The low temperature ground state is a robust FM state with magnetic moments lying along c-axis. Ferromagnetism is also confirmed for temperatures between 360 and 420 K. A wide ranging search in q-space for magnetic scattering in the intermediate temperature range revealed an incommensurate AFM state in the structure of a SDW. We confirmed the existence of non-coplanar moments in the SDW state that has been predicted through transport measurements based on the large topological Hall Effects. Transport measurements with current in different orientations and fields revealed Fermi surface gapping associated with the SDW state which grows larger with reduced temperature in the intermediate state.

With the consistent picture of SDW state to low T FM state transition and a Fermi surface which is gapped and which widens with cooling, we propose a RKKY coupling mechanism for the long range ordering force that causes the SDW instability. period here then start a new sentence. The behavior of Fe_3Ga_4 appears to be comparable to Rare-Earth marerials where RKKY interactions are thought to

dominate the magnetic interactions. The study of the neutron scattering in moderate magnetic field indicate that the SDW coexist with the high T FM state.

In conclusion, we have successfully determined the magnetic structures of this interesting compound and our neutron scattering results have confirmed a number of the important findings in previous magnetic or transport measurements. Those findings include the tendency to stabilize the low T FM state to higher temperatures in moderate magnetic fields and the non-coplanar moments in the incommensurate SDW phase which corresponding to the topological transport properties. The results in high temperature that the SDW survive with a small value of correlation length before disappearing and the field enhanced SDW to coexist with the high T FM state scenario indicate interesting mechanism behind the T_2 transition. We have discovered an rare case of the indirect exchange coupling between charge carries and local moments introduces incommensurate SDW instability in a transition metal system where there is no noticeable Fermi surface nesting. A low temperature transition occurs when the Fermi surface gapping associated with the SDW phase becomes wide enough to decrease the RKKY interaction such that the FM state becomes the lower energy state. With the mechanism behind the intermediate SDW state and its transition to low T FM unraveled, mysteries on the reentered FM above T_2 still remain. Future work work on the high temperature FM region is required to fully understand the complex magnetism of Fe_3Ga_4.

5.4 Bibliography

[1] Alireza Akbari, Ilya Eremin, and Peter Thalmeier. RKKY interaction in the spin-density-wave phase of iron-based superconductors. *Phys. Rev. B*, 84: 134513, 2011.

[2] M. Braden, O. Friedt, Y. Sidis, P. Bourges, M. Minakata, and Y. Maeno. Incommensurate magnetic ordering in $Sr_2Ru_{1-x}Ti_xO_4$. *Phys. Rev. Lett.*, 88: 197002, 2002.

[3] G. F. Chen, Z. Li, D. Wu, G. Li, W. Z. Hu, J. Dong, P. Zheng, J. L. Luo, and N. L. Wang. Superconductivity at 41 K and its competition with spin-density-wave instability in layered $CeO_{1-x}F_xFeAs$. *Phys. Rev. Lett.*, 100:247002, 2008.

[4] Bernard R. Cooper. Magnetoelastic effects and the magnetic properties of rare-earth metals. *Physical Review Letters*, 19(16):900–903, 1967.

[5] A. del Moral and E. W. Lee. Exchange force explanation for the antiferromagnet-ferromagnet transition in dysprosium. *Journal of Physics C: Solid State Physics*, 8(22):3881, 1975.

[6] H. G. M. Duijn. *Magnetotransport and magnetocaloric effects in intermetallic compounds*. Ph.d thesis, Universiteit van Amsterdam, 2000.

[7] R. J. Elliott and F. A. Wedgwood. Theory of the resistance of the rare earth metals. *Proceedings of the Physical Society*, 81(5):846, 1963.

[8] Eric Fawcett. Spin-density-wave antiferromagnetism in chromium. *Reviews of Modern Physics*, 60(1):209–283, 1988.

[9] Yejun Feng, Jiyang Wang, D. M. Silevitch, B. Mihaila, J. W. Kim, J.-Q. Yan, R. K. Schulze, Nayoon Woo, A. Palmer, Y. Ren, Jasper van Wezel, P. B. Littlewood, and T. F. Rosenbaum. Incommensurate antiferromagnetism in a pure spin system via cooperative organization of local and itinerant moments. *Proceedings of the National Academy of Sciences*, 110(9):3287–3292, 2013.

[10] Yejun Feng, Jiyang Wang, A. Palmer, J. A. Aguiar, B. Mihaila, J. Q. Yan, P. B. Littlewood, and T. F. Rosenbaum. Hidden one-dimensional spin modulation in a three-dimensional metal. *Nat Commun*, 5, 2014.

[11] M. Gulcsi, M. Crian, and Zs Gulcsi. Theory of coexistence between change-density-waves, spin-density-waves and ferromagnetism. *Journal of Magnetism and Magnetic Materials*, 39(3):290–294, 1983.

[12] F. Honda, N. Metoki, T. D. Matsuda, Y. Haga, and Y. nuki. Long-period, longitudinal spin density modulation in an itinerant 5f magnetic compound UCu_2Si_2. *Journal of Physics: Condensed Matter*, 18(2):479, 2006.

[13] Nobuo Kawamiya and Kengo Adachi. Magnetic and Mssbauer studies of metamagnetic Fe_3Ga_4. *Journal of the Physical Society of Japan*, 55(2):634–640, 1986.

[14] H. Kimura, Y. Sakamoto, M. Fukunaga, H. Hiraka, and Y. Noda. Control of magnetic interaction and ferroelectricity by nonmagnetic Ga substitution in multiferroic YMn_2O_5. *Phys. Rev. B*, 87:104414, 2013.

[15] N. I. Kulikov and V. V. Tugushev. Spin-density waves and itinerant antiferromagnetism in metals. *Soviet Physics Uspekhi*, 27(12):954, 1984.

[16] E. W. Lee. The magnetoelastic behaviour of antiferromagnets having helical spin configurations. *Proceedings of the Physical Society*, 84(5):693, 1964.

[17] J. H. Mendez, C. E. Ekuma, Y. Wu, B. W. Fulfer, J. C. Prestigiacomo, W. A. Shelton, M. Jarrell, J. Moreno, D. P. Young, P. W. Adams, A. Karki, R. Jin, Julia Y. Chan, and J. F. DiTusa. Competing magnetic states, disorder, and the magnetic character of Fe_3Ga_4. *Physical Review B*, 91(14):144409, 2015.

[18] S. Ohira-Kawamura, H. Shishido, A. Yoshida, R. Okazaki, H. Kawano-Furukawa, T. Shibauchi, H. Harima, and Y. Matsuda. Competition between unconventional superconductivity and incommensurate antiferromagnetic order in $CeRh_{1-x}Co_xIn_5$. *Phys. Rev. B*, 76:132507, 2007.

[19] A. W. Overhauser. Spin density waves in an electron gas. *Physical Review*, 128(3):1437–1452, 1962.

[20] L.-M. Peng, G. Ren, S. L. Dudarev, and M. J. Whelan. Debye–Waller Factors and Absorptive Scattering Factors of Elemental Crystals. *Acta Crystallographica Section A*, 52(3):456–470, 1996.

[21] M. J. Philippe, B. Malaman, and B. Roques. Preparation and study of intermetalliciron-gallium compounds in single-crystal state. *Comptes Rendus Hebdomadaires Des Seances De L Academie Des Sciences Serie C*, 278 (17):1093–1095, 1974.

[22] M. J. Philippe, B. Malaman, B. Roques, A. Courtois, and J. Protas. Crystal structure of phases Fe_3Ga_4 and Cr_3Ga_4. *Acta Crystallographica Section B-Structural Science*, 31, 1975.

[23] J. Rodriguez-Carvajal. Recent advances in magnetic structure determination by neutron powder diffraction. *Physica B*, 192:55, 1993.

[24] D. B. Sirdeshmukh, L. Sirdeshmukh, and Subhadra K. G. *DebyeWaller Factors of Crystals*, volume 80 of *Materials science*, chapter 3, pages 77–133. Springer Berlin Heidelberg, 2006.

[25] Oleg P. Sushkov and Valeri N. Kotov. Theory of incommensurate magnetic correlations across the insulator-superconductor transition of underdoped $La_{2-x}Sr_xCuO_4$. *Phys. Rev. Lett.*, 94:097005, 2005.

[26] E. Svanidze, Jiakui K. Wang, T. Besara, L. Liu, Q. Huang, T. Siegrist, B. Frandsen, J. W. Lynn, Andriy H. Nevidomskyy, Monika B. Gamza, M. C. Aronson, Y. J. Uemura, and E. Morosan. An itinerant antiferromagnetic metal without magnetic constituents. *Nat Commun*, 6, 2015.

[27] Yoshikazu Tanaka, Noriki Terada, Taro Nakajima, Munetaka Taguchi, Taro Kojima, Yasutaka Takata, Setsuo Mitsuda, Masaki Oura, Yasunori Senba, Haruhiko Ohashi, and Shik Shin. Incommensurate orbital modulation behind ferroelectricity in $CuFeO_2$. *Phys. Rev. Lett.*, 109:127205, 2012.

[28] R. Troc, M. Samsel-Czekaa, J. Stpien-Damm, and B. Coqblin. Interplay between ferromagnetism, SDW order, and underscreened Kondo lattice in

UCu_2Si_2. *Physical Review B*, 85(22):224434, 2012.

[29] V.G. Veselago and L.I. Vinokurova. *The magnetic and electron structures of transition metals and alloys*. Commack, NY (USA); Nova Science Publishers, Inc., Jan 1988.

Chapter 6
Summary

Two iron-based magnetic systems have been investigated in this thesis. We illustrated that the physical properties of each material corresponds to one type of local magnetic moments and itinerant charge carriers interactions.

In dilute Co doped FeSi the Kondo effect was found to incompletely screen the local magnetic moments associated with the dopants. This leaves partially compensated magnetic moments which tend to form spin-singlets well below the Kondo temperature. As a result, there are a large density of free fluctuating moments which remain freely fluctuating down to our lowest measured temperatures (300 mK). Those underscreened magnetic moments induce inelastic scattering leading to the non-FL behavior near the IMT region of $Fe_{1-x,y}Mn_xCo_ySi$. Application of magnetic field removes these inelastic scattering centers allowing the system to return to a disordered FL. When the dopant level is increased the Kondo effect between charge carriers and local moments is overshadowed by the collective behavior of the impurity moments. Therefore, an ordering effect between local moments overturns the undercompensated Kondo mechanism.

In Fe_3Ga_4 the local spins couple indirectly through conducting itinerant electrons - the RKKY interaction. The long range periodic RKKY interaction induces a SDW order and stabilizes the incommensurablility in the SDW phase. The partial Fermi surface gap related with the SDW phase grows with decreasing temperature which leads to a decreased metamagnetic field with cooling. Meanwhile, the car-

rier density continues to decrease as the gap grows with cooling until the RKKY interaction weakens so that the ferromagnetic exchange dominates the system below 70 K. At these temperatures the SDW state surrenders to the ferromagnetic ground state, the related gap in Fermi surface closes, and a carrier density increase is reflected in the conductivity data.

In the two Fe-based compounds that we investigated, either the Kondo effect or RKKY interaction works independently in affecting the material properties. However, the interplay between the two mechanisms have been discovered in rare earth materials such as Ce compounds like (Ce, La)PdSn[5] and uranium compounds like UTe or $UCu_{0.9}Sb_2$[2;3;7]. The competition scenario of Kondo lattice and RKKY interaction was first proposed by Doniach[1] and extended[2;4] for underscreened Kondo effects to describe the ferromagnetic Kondo properties of uranium compounds. It has been discovered that non-FL behavior may coexist with FM order in rare earth materials, i.e. $URu_{2-x}Re_xSi_2$ and $CeRuSi_2$[6;8]. The competition the Kondo effect and RKKY interaction is important in such f-electron systems where non-FL behavior is associated with quantum criticality. Here, the non-FL behavior occurs in doped semiconducting systems when in an underscreened regime and the interesting behavior continues as the magnetic state is nucleated via higher densities of dopants in $Fe_{1-y}Co_ySi$. In addition, the investigation on Fe_3Ga_4 presents that the incommensurate magnetically ordered states in transition metal compounds could have the origin of the RKKY interactions.

6.1 Bibliography

[1] The Kondo lattice and weak antiferromagnetism. *Physica B+C*, 91:231 – 234, 1977.

[2] Doniach diagram for ordered, disordered and underscreened Kondo lattices. *Journal of Magnetism and Magnetic Materials*, 320(14):1989 – 1994, 2008.

[3] Piers Coleman. *Heavy Fermions: Electrons at the Edge of Magnetism*. John Wiley and Sons, Ltd, 2007.

[4] J. Gan, P. Coleman, and N. Andrei. Coexistence of Fermi liquid and magnetism in the underscreened Kondo problem. *Phys. Rev. Lett.*, 68:3476–3479, 1992.

[5] Dexuan Huo, Katsunori Mori, Tomohiko Kuwai, Hiroki Kondo, Yosikazu Isikawa, and Junji Sakurai. RKKY interaction and Kondo effect in $(Ce, La)PdSn$. *Journal of the Physical Society of Japan*, 68(10):3377–3382, 1999.

[6] V. N. Nikiforov, M. Baran, and V. Yu. Irkhin. Ferromagnetic Kondo lattice $CeRuSi_2$ with non-Fermi-liquid behavior. *Journal of Experimental and Theoretical Physics*, 116(5), 2013.

[7] N. B. Perkins, M. D. Núñez Regueiro, B. Coqblin, and J. R. Iglesias. Underscreened Kondo lattice model applied to heavy fermion uranium compounds. *Phys. Rev. B*, 76:125101, 2007.

[8] M. Sasaki, A. Ohnishi, T. Kikuchi, M. Kitaura, Ki-Seok Kim, and Heon-Jung Kim. Interplay between the Kondo effect and randomness: Griffiths phase in KM_xTiSe_2 (M = Co, Ni, and Fe) single crystals. *Phys. Rev. B*, 82:224416, 2010.

Appendix: Noncentrosymmetric Magnetic Materials

The lack of an inversion center allows a type of spin-orbital interaction in magnetic materials, named after Dzyaloshinsky and Moriya, which can have important effects on the magnetic and charge carrier properties. In magnetic B20 materials, it was established that there are three hierarchy of interactions with well separated energy scales[1;3]. The strongest is the ferromagnetic exchange interaction that leads to a polarized spin alignment. This is followed in importance by the Dzyaloshinsky-Moriya (DM) interaction that produces long range order modulations and is usually about one order of magnitude weaker. Dzyaloshinsky proposed that long period helices could form as a result of spin-orbital interaction in noncentrosymmetric materials[2], such as MnSi.

The role of DM interaction in HM materials, such as MnSi and $Fe_{1-y}Co_ySi$, has been studied for several decades. Much progress have been achieved, yet there are still new and interesting results being reported such as the recently discovered skyrmion lattice. The weakest interaction in the list is the crystal-field interaction. It is the higher order spin-orbital terms that effects the directionality of the helimagnetic wavevector with respect to the crystalline lattice.

The DM interaction can be described by an additional term in the Ginzburg-Landau free energy:

$$D \cdot \vec{H} = \vec{D} \cdot \vec{M} \cdot \Delta \times \vec{M}. \tag{6.1}$$

Here M is the magnetization and $\vec{D}$ is the DM exchange constant (Typically $|D| \ll |J|$). This interaction tends to align the magnetic moments perpendicu-

lar to each other and to $\vec{D}$ which lies along the symmetry axis. Since $|D| \ll |J|$ and $\vec{J}$ is usually antiferromagnetic, the DM interaction tends to produce canted antiferromagnetic structures.

Based on a Ginzburg-Landau expansion of the free energy of itinerant ferromagnets, the magnetic field B that stabilizes the magnetization $\vec{M}$ is given by the usual magnetic equation of state:

$$B(\vec{M}) = \frac{1}{V}\frac{\partial F}{\partial \vec{M}} = A\vec{M} + b\vec{M}^3. \tag{6.2}$$

The temperature-dependent inverse susceptibility

$$A = a + b[3\langle m_{\parallel}^2\rangle + 2\langle m_{\perp}^2\rangle] \tag{6.3}$$

includes the effects of thermal spin fluctuations. Here $\perp$ and $\parallel$ denote fluctuations transverse and longitudinal to the local magnetization. The parameters a and b represent the zero temperature inverse initial susceptibility. The initial mode-mode coupling parameter is $m_{s,0} = -a/b$ which can be derived from the magnetic field dependence of $\vec{M}$.

Here we introduce the Ginzburg-Landau treatment for helimagnets. Even in the isotropic helimagnets, the DM interaction, the transition at conical upper critical field (H_c) and crystal anisotropies all need to be considered to describe the reorientation transition at lower conical critical field. Note that the upper critical field is not dependent on orientation, while the lower one depends on the orientation of the field with respect to the crystal lattice. The form of the Ginzburg-Landau potential of the magnetization for an isotropic helimagnet is:

$$\mathcal{V}(\vec{M}) = \frac{a}{2}\vec{M}^2 + \frac{b}{4}(\vec{M}^2)^2 + \frac{D}{2}\vec{M}(\Delta \times \vec{M}) - \frac{c}{2}\vec{M}\Delta^2\vec{M} - \vec{B}\vec{M} \tag{6.4}$$

where c is a parameter related to high order terms in susceptibility. In a general regime of the phase diagram outside of the **A**-phase, the potential can be described by minimization of $\vec{M}$ with the conical-helix Ansatz as

$$\vec{M}(\vec{r}) = M\hat{B} + M_Q cos(\vec{Q}\vec{r})\hat{e}_1 + M_Q sin(\vec{Q}\vec{r})\hat{e}_2. \tag{6.5}$$

$\vec{Q}$ is the helix wavevector as $\vec{Q} = Q\hat{B}$. $\hat{e}_1$ and $\hat{e}_2$ are unit vectors that has

$$\hat{e}_1 \times \hat{e}_2 = \hat{B}. \tag{6.6}$$

Now the Eq. 6.4 can be simplified as

$$\mathcal{V}(M, M_Q, Q) = \frac{a}{2}(M^2 + {M_Q}^2) + \frac{b}{4}(M^2 + {M_Q}^2)^2 - \frac{D}{2}{M_Q}^2 Q + \frac{c}{2}{M_Q}^2 Q^2 - MB. \tag{6.7}$$

It leads to three equations:

$$\frac{\partial \mathcal{V}}{\partial M} = aM + b(M^2 + {M_Q}^2)M - B = 0, \tag{6.8}$$

$$\frac{\partial \mathcal{V}}{\partial M_Q} = aM_Q + b(M^2 + {M_Q}^2)M_Q - DQM_Q + cQ^2 M_Q = 0 \tag{6.9}$$

and

$$\frac{\partial \mathcal{V}}{\partial Q} = -\frac{D}{2}{M_Q}^2 + cQ{M_Q}^2 = 0. \tag{6.10}$$

Eq. 6.10 can be solved at a finite $M_Q > 0$ with the helix wavevector

$$Q = \frac{D}{2c}. \tag{6.11}$$

Then the Eq. 6.9 can be simplified as

$$a + b(M^2 + {M_Q}^2) - \frac{D^2}{4c} = 0 \tag{6.12}$$

When comparing with Eq. 6.8, there can be a simple form

$$\frac{B}{M} = -\frac{D^2}{4c} = cQ^2 \tag{6.13}$$

This indicates that magnetization is a linear function of the magnetic field and their relation is determined by $\frac{1}{cQ^2}$ in the conical phase. And the final result for magnetization at conical field is

$$M_Q = \frac{1}{\sqrt{b}}\sqrt{cQ^2 - a - b(\frac{B}{cQ^2})^2} \tag{6.14}$$

with

$$B_{c2} = cQ^2\sqrt{\frac{cQ^2 - a}{-b}} \tag{6.15}$$

The conical phase and the ferromagnetic phase are delimited by the upper critical field B_{c2}. When the magnetic field is small, $B < B_{c2}$, one can have the stable conical helix. When the field is larger than B_{c2}, the system orders ferromagnetically with $M_Q = 0$. The magnetization goes back to Eq. 6.2.

The characteristics of the spin fluctuations depend on the energy range. In the range that energy is larger than the spin-orbit coupling and momenta larger than the DM interaction D, the spin fluctuation is ferromagnetic. Spin-orbital coupling is important in the limit of small energies where system is far from an itinerant ferromagnet. The approximate form for magnetization where $B \geq B_{c2}$ and close to B_{c2} is:

$$\frac{B(M)}{M} \approx A + bM^2 \tag{6.16}$$

and $B_{c2} = cQ^2M_{c2}$. As a result, the Arrott form in the noncentrosymmetric itinerant ferromagnetic system can be obtained from Eq. 6.16, with $\frac{B}{M}$ vs. M^2 being approximately linear.

Bibliography

[1] A. Bauer, A. Neubauer, C. Franz, M. Garst, and C. Pfleiderer. Quantum phase transitions in single-crystal $Mn_{1-x}Fe_xSi$ and $Mn_{1-x}Co_xSi$: Crystal growth, magnetization, ac susceptibility, and specific heat. *Physical Review B*, 82(6):064404, 2010.

[2] I. E. Dzyaloshinskii. Theory of helicoidal structures in antiferromagnets. *SOVIET PHYSICS JETP*, 19(1):960–971, 1964.

[3] U. K. Roszler, A. N. Bogdanov, and C. Pfleiderer. Spontaneous skyrmion ground states in magnetic metals. *Nature*, 442(17):797, 2006.

Vita

Yan Wu was born in July 1985 at Xian City, China. She finished her undergraduate studies at Northwest University at China in May 2006. She went to Chinese Academy of Science, Fujian institute of research on structure of materials at September 2006 and earned her Master degree of science in December 2008. In January 2009, she came to Louisiana State University to pursue graduate studies of doctoral degree in physics. She is currently a candidate for the degree of Doctor of Philosophy in physics, which is anticipated to be awarded in May 2016.